Scaling of Gas Diffusion into Limited Partial Cavity
and
Interaction of Vertical Jet with Cross-flow beneath Horizontal Surface

by

In-ho R. Lee

A dissertation submitted in partial fulfillment
of the requirements for the degree of
Doctor of Philosophy
(Naval Architecture and Marine Engineering)
in The University of Michigan
2015

Doctoral Committee:

Professor Steven L. Ceccio (Chair)
Professor Luis Bernal
Assistant Research Scientist Simo A. Mäkiharju
Professor Marc Perlin

Dedicated to my family

ACKNOWLEDGMENTS

I would like to thank to my advisor, Prof. Steve Ceccio for not only his guidance throughout my graduate studies but also motivation on life and social skills. Whenever I met difficulties in my academic work, he supported me in direct and indirect ways. Also, I would like to thank my committee members, Prof. Marc Perlin for both being in my committee and for supporting me with physical guidance in experiment, Prof. Luis Bernal for agreeing to be in my committee, and Dr. Simo Makiharju for both being in my committee and for supporting me with all detail consulting.

My colleagues, Dr. Harish Ganesh, Joel Hartenberger, Jimmy Gose, and Seongjin Yoon deserve special mention for all the collaborations, sharing resources and discussions. In addition, I would like to thank Kent Pruss, Bill Kirkpatrick, and Marv Casey for their time and effort at machine shop at Autolab. Also, Nick Wild, David Parsons and Brent Cragin deserve special mention for all the expertise they provided during my time at MHL. I would also like to thank Amanda Dallaire and Sallie Kne for their time and effort.

My graduate school life in Ann Arbor would not have been complete without friends. In that regard I thank to Dr. Daehyun Kim, Dr. Sungmin Lee, Dr. Hongrae Park, Dr. EunSoo Kim, Dr. Eunjung Chae, Dr. Ayoung Kim, and Dr. Hongyoon Kim, for sharing not only their academic talks but also entertaining life. I would also like to thank all my friends, tennis fellows, Korean Basketball team, and board members from KSAG (Korean Student Association- Graduate), for all the great times.

Finally, I would love to thank my family for their supports throughout all my life. Now I more respect my father with his research work and his role in the family. My

mother deserves a special mention for being very supportive of all my decisions. And at last but not least, I would like to thank my lovely wife and my unborn baby boy. They have been my motivation and happiness throughout all my daily life.

TABLE OF CONTENTS

LIST OF FIGURES

LIST OF TABLES

NOMENCLATURE

Scaling of Gas Diffusion into Limited Partial Cavities

c_O	Freestream dissolved gas concentration
c_S	Saturated dissolved gas concentration at the cavity surface
$c_{S,US}$	Saturated dissolved gas content at the cavity surface in the low pressure region near the cavity separation
D	Molecular diffusion coefficient
D_t	Turbulent diffusion coefficient
k_B	Constant used at each model. Value varies by assumptions
L_C	Partial cavity length
L_D	Length scale derived from each modeling assumptions
L_{DB}	Length scale used on model of Brennen
L_{DPK}	Length scale used on model of Parkin and Kermeen (Parkin and Kermeen (1963))
L_{DPR}	Length scale used on model of Parkin and Ravindra (Parkin and Ravindra (1991))
L_{DSF}	Length scale used on Slug flow model (Parkin and Ravindra (1991))
$L_{D\delta}$	Length scale related to the diffusion boundary layer at the bubble surface within the cavity
M_B	Total amount(mass) of ingassing per unit volume of the cavity
m_B	Mass of the non-condensable gas in the bubble
$\dot{m}_B$	Net mass flux in general
$\dot{m}_{B,Sat}$	Net mass flux in the wake of the cavity for super-saturated conditions

$\dot{m}_{B,USat}$	Net mass flux in the wake of the cavity for under-saturated conditions
$\dot{m}_{INJ}$	Mass flux of air injected into wedge apex
$\dot{m}_{SB}$	Mass rate of ingassing into a single bubble
N_B	Number of bubble
P	Static Pressure in the measurement location upstream of the wedge
P_{G_O}	Pressure of the non-condensable gas in a bubble
P_T	Throat pressure
P_V	Liquid vapor pressure
P_W	Static pressure in the measurement location downstream of the wedge
q_C	Net volume flux of flow in and out of the cavity
R	Ideal gas constant
R_{BC}	Average bubble radius within the cavitating region
R_B	Bubble radius measured in the cavity wake
$\langle R_B \rangle$	Average bubble radius measured in the cavity wake
S_C	Schmit number ($S_C = \nu/D$)
S_{C_t}	Turbulent Schmit number ($S_{C_t} = \nu/D_t$)
S	Surface tension of water against air
T	Temperature in Kelvin
t_B	Residence time of the bubbles in super-saturated region pressure
U	Freestream average flow speed
U_C	Flow speed at the cavity interface (the throat speed)
V_C	Volume of the partial cavity
$V_{C,US}$	Volume of the partial cavity for under-saturated flow
α_C	Average void fraction of partial cavity
α_W	Average void fraction in the wake
δ	Boundary layer thickness of the flow at the cavity interface

θ	Momentum thickness of the flow at the cavity interface
υ	Liquid kinematic viscosity
σ	Cavitation number $\left(\sigma = (P - P_V)/\left(\frac{1}{2}\rho U^2\right)\right)$
ρ	Liquid density

Interaction of Vertical Jet with Cross-flow beneath Horizontal Surface

a	Constant coefficient used at $\left(P_C = P_\infty\left(1 + aQ^{*b}\right)\right)$
b	Constant coefficient used at $\left(P_C = P_\infty\left(1 + aQ^{*b}\right)\right)$
C	Average length of chord of leg
C_D	Drag coefficient $\left(C_D = D/\left(\frac{1}{2}\rho {U_\infty}^2 e\right)\right)$
C_{DC}	Discharge coefficient (Fluid Flow, Rolf H. Sabersky, 4th edition)
$\hat{C}$	Calculated chord length of the cavity(leg) from $\left(Q_i = \gamma \frac{\pi}{2} \hat{C} e U_\infty sin\varphi\right)$
D	Drag force
D_i	Diameter of injection tube
e	Thickness of the cavity(leg)
$\hat{e}$	Calculated thickness of the cavity(leg) from $\left(Q_i = \frac{\pi}{2} C \hat{e} U_\infty sin\varphi\right)$
$\check{e}$	Calculated thickness of the cavity(leg) from $\left(\check{e} = aQ^{*b} \frac{P_\infty}{\rho g \varepsilon}\right)$
Fr_δ	Froude number $\left(Fr_\delta = U_\infty/\sqrt{g\delta}\right)$
${Fr_\delta}^*$	Froude number with $cos\varphi$ $\left({Fr_\delta}^* = U_\infty cos\varphi/\sqrt{g\delta}\right)$
g	Gravity acceleration
Ma	Mach number ($Ma = U_i$/c, c: speed of sound in water, $c = 1484$ m/s)
P_i	Average dynamic pressure at the exit of injection tube
P_C	Average pressure in the cavity(leg)
P_∞	Hydrostatic pressure with fixed draft on the bottom surface of barge model

Q_i	Net volume flux of injected jet
Q^*	Non-dimensionalized volume rate $\left(Q^* = Q_i/(U_\infty \delta^2)\right)$
Re_{D_i}	Reynolds number $\left(Re_{D_i} = U_i D_i/\nu_i\right)$
r	Velocity ratio (r = U_i/U_∞)
S	Surface tension between water and air (S =0.072 N/m)
U^*	Volume rate ratio of jet and cross-flow in the boundary layer ($U^* = Q_i/U_\infty \delta^2$)
U_i	Average speed of jet at the exit of injection tube $\left(U_i = Q_i/\left(\frac{\pi}{4}{D_i}^2\right)\right)$
U_∞	Average speed of cross-flow
We	Weber number ($We = \rho {U_\infty}^2 \delta/S$)
Π	Momentum ratio of the jet and the cross-flow $\left(\Pi = \left(\rho_i {U_i}^2\right)/\left(\rho_\infty {U_\infty}^2\right)\right)$
β	Angle of injection tube. Angle between jet injection direction and barge surface on upstream direction
γ	Constant coefficient used at $\left(Q_i = \gamma \frac{\pi}{2} \hat{C} e U_\infty sin\varphi\right)$
δ	Boundary layer thickness of the cross-flow on the barge hull. δ_1 and δ_2 refer boundary layer thickness of Barge model I and Barge model II
ε	Constant coefficient used at ($P_C = P_\infty + \varepsilon \rho g e$)
ν_i	Kinematic viscosity of fluid of the jet
ν_∞	Kinematic viscosity of fluid of the cross-flow
ρ_i	Density of fluid of the jet
ρ_∞	Density of fluid of the cross-flow
σ	Cavitation number $\left(\sigma = (P_\infty - P_C)/\left(\frac{1}{2}\rho {U_\infty}^2\right)\right)$
$\hat{\sigma}$	Cavitation number with reference pressure at boundary layer thickness $\left(\hat{\sigma} = (P_\infty - P_C)/\left(\frac{1}{2}\rho {U_\infty}^2\right)\right)$
σ^*	Cavitation number including $cos\varphi$ $\left(\sigma^* = (P_\infty - P_C)/\left(\frac{1}{2}\rho (U_\infty cos\varphi)^2\right)\right)$

$\hat{\sigma}^*$	Cavitation number with reference pressure at boundary layer thickness including $cos\varphi$ $\left(\hat{\sigma}^* = (P_\infty + \rho g\delta - P_C)/\left(\frac{1}{2}\rho(U_\infty cos\varphi)^2\right)\right)$
φ	Sweep angle of leg. Average angle between transverse plane and edge of split leg
$\hat{\varphi}$	Calculated sweep angle of leg from section 9.3

ABSTRACT

Scaling of Gas Diffusion into Limited Partial Cavity: Bubble populations in the wake of a partial cavity resulting from gas diffusion were measured to determine the non-condensable gas flux into the cavity. The diffusion rate is related to the dissolved gas content, the local cavity pressure, and the flow within and around the cavity. The measurements are used to revisit various scaling relationships for the gas diffusion, and it is found that traditional scaling that assume the presence of a gas pocket over-predict the gas diffusion. A new scaling based on diffusion into low void-fraction bubbly mixture within the partial cavity is proposed, and it is shown to adequately scale the observed production of gas bubbles.

Interaction of Vertical Jet with Cross-flow beneath Horizontal Surface: Vertical gas jet injection into liquid cross-flow beneath horizontal surface was observed and the physics of it was studied. Previous studies on jet and cross-flow interactions showed that cross-flow speed, jet speed, and their momentum ratio are related to the resulting flow behavior. In the present study, it is found that overall topology of the resulting flow is completely different with previous studies by changing the direction of jet injection regarding gravity direction. Dimensions to describe new topology and scaling based on gravity acceleration and boundary layer thickness in addition to traditional parameters are proposed.

CHAPTER 1

Introduction

This thesis presents two different studies on multiphase flow. The first is a study of gas diffusion into limited partial cavities and the next is a study of interaction of vertical jet into cross-flow beneath horizontal surface. Chapter 2-4 will present the study of gas diffusion into limited partial cavities and Chapter 5-9 will present the study of interaction of vertical jet into cross-flow beneath horizontal surface.

1.1 Scaling of Gas Diffusion into Limited Partial Cavities

Cavitation can occur when liquid is exposed to a reduction in static pressure to that near or below the fluid vapor pressure. When the fluid experiences pressure below vapor pressure (*i.e.* tension), vapor bubbles can form and grow. And, if the flow pressure recovers, the vapor can re-condense. However, if non-condensable gas is dissolved in the liquid, the presence of vapor pockets or bubbles provides an interface for mass transfer of the dissolved gasses. Therefore, even when vapor cavitation bubbles collapse, it is possible to observe thick clouds of remnant micro-bubbles of largely non-condensable gas. It would be desirable to predict the rate at which the dissolved gas comes out of solution into cavitating flows. Many previous studies were done to observe and analyze the net mass flux of the non-condensable gas bubbles from partial cavity. However, most of the solutions from the studies significantly over-predict or under-predict the net mass flux, which indicates critical parameter is missing.

In the present study, cavitation occurring on the wedge is studied with bubble population measurements based on high speed cinematography. Cavitation on the wedge with different inflow conditions is carefully studied. Non-condensable gas mass flux observed experimentally is compared with scalings from previous studies, and new scaling is suggested.

1.1.1 Contributions of the study

Using a high magnification imager coupled to a high-speed digital video camera has improved measurement of the non-condensable gas net mass flux in the wake of the partial cavity. The present study also identifies presence of non-condensable gas in under-saturated flow based on the level of the saturation in the free stream and the pressure at the apex of the wedge. Most important contribution of the present study is considering void fraction of the wedge cavitation as a parameter solving the net mass flux of non-condensable gas. Void fraction measurements of the wedge cavitation using 2-D X-ray densitometry with the same experiment set up are referred.

1.1.2 Roadmap

Chapter 2 introduces the problem with overview of the physics and previous studies in the topic. Chapter 3 describes the experimental set up, water channel, instruments used for measurements, inflow conditions, and imaging system. Chapter 4 presents the result of mass flux of the non-condensable gas diffused into the cavity and a discussion of the gas diffusion into limited partial cavities.

1.2 Interaction of Vertical Jet with Cross-flow beneath Horizontal Surface

In the purpose of reducing ship energy consumption for better energy efficiency, numerous methods to reduce drag of ship were investigated for years. One of the efficient ways of skin friction drag reduction is to inject air beneath the hull to create air layer that covers part of the hull. Figure 1.1 presents the image of Mitsubishi Air Lubrication System. Air is injected through spanwise slot on the bottom hull to create the air layer. Simpler way of introducing air is to inject through circular orifice. However, the dynamics of air injection into liquid cross-flow under horizontal surfaces is not well understood.

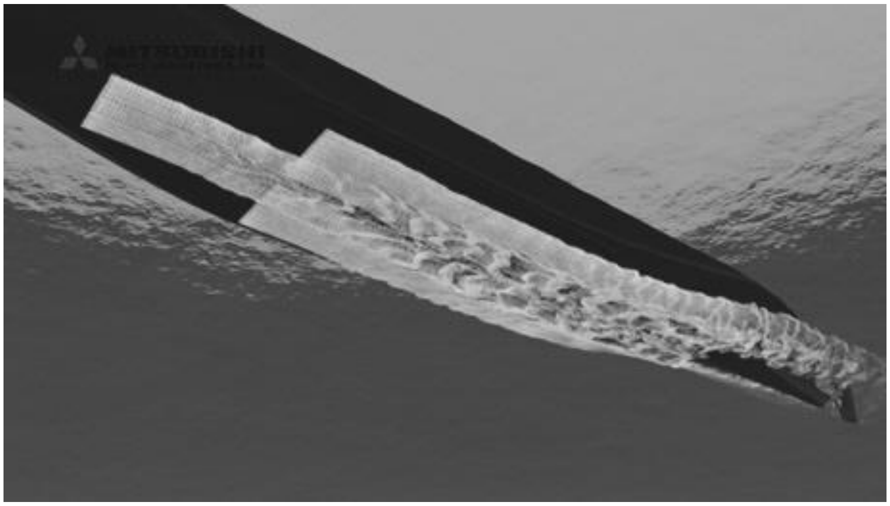

Figure 1.1 Mitsubishi Air Lubrication System

In the present study, air injection through circular orifice into liquid cross-flow beneath horizontal surface is studied with high speed and low speed cinematography. Air development with different flow conditions such as cross-flow speed, air injection rate, and boundary layer profile of cross-flow are observed and analyzed. The topology of resulting flow is compared with jet injection into cross-flow in different directions.

1.2.1 Contributions of the study

Many studies on interaction of jet and cross-flow have been investigated for long time. However, most of the studies were done in different conditions the problem we have. Either, density difference of the jet and the cross-flow and/or direction of jet regarding gravity direction was different with the current problem. Few investigations of vertical gas jet along gravity direction into liquid cross-flow beneath horizontal surface have been reported. However, the range of air injection rate was relatively low and the flow conditions were limited. In the present study, range of flow conditions is relatively wide to observe different type of topology of resulting flow. In addition to important parameters on jet and cross-flow interaction from previous studies, gravity is introduced to explain the physics. Also, the data from the present study can be used for CFD code validations on interaction of vertical gas jet along gravity direction and liquid cross-flow beneath horizontal surfaces.

1.2.2 Roadmap

Chapter 5 introduces the problem with overview of the physics and previous studies in the topic. Chapter 6 describes the experimental set up, basin, barge models, instruments, and imaging system. Chapter 7 presents the result on interaction of vertical jet with cross-flow beneath horizontal surface. Chapter 8 discusses the dimensional and non-dimensional scaling of interaction of vertical jet with cross-flow beneath horizontal surface. Chapter 9 deals with the physics of this part of the study, concludes the chapter, and presents future work.

CHAPTER 2

Scaling of Gas Diffusion into Limited Partial Cavities

2.1 Background

Small non-condensable gas bubbles are typically present in the wake of partial cavitation. Partial cavitation is often associated with a low-pressure region of flow separation that is either partially or fully filled with the fluid's vapor phase. If the freestream liquid contains dissolved gas, some of this gas may diffuse into the cavity at the low-pressure liquid-vapor interfaces. Entrainment and pressure recovery in the cavity wake leads to condensation of the vapor, but the non-condensable gas may not rapidly return to solution. Instead, clouds of small gas bubbles will be convected away from the cavity.

This process was discussed by a number of previous researchers, including Parkin and Kermeen (1963), Gadd and Grant (1965), Brennen (1969), Billet and Weir (1975), and Maeda *et al.* (1991). A review presented by Yu and Ceccio (1997) used measurements of the bubble populations downstream of a partial cavity to compare the observed gas diffusion rates to those predicted from four different scaling models.

Figure 2.1 shows a schematic diagram of an ideal partial cavity, adapted from Yu and Ceccio (1997). Here, it is assumed that the gas pocket is at vapor pressure. The freestream speed, cavitation number, and dissolved non-condensable gas content are U, σ, and c_O, respectively. The flow velocity at the cavity free surface is $U_C = U\sqrt{1+\sigma}$, and the length is L_C. At the cavity surface, the saturated dissolved gas content is c_S. The turbulent boundary layer over the cavity interface is characterized with a boundary layer thickness, δ, and momentum thickness, θ. Gas diffusion rates from the cavity can then written as,

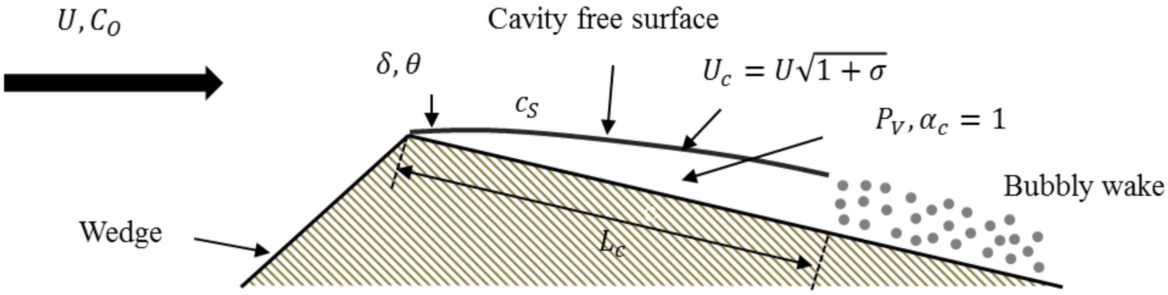

Figure 2.1 Schematic drawings of the partial cavity flows: Classical depiction of the cavity as a vapor pocket with a free surface

$$\dot{m}_B = k_B(c_O - c_S)U_C L_D \tag{2.1}$$

where k_B is a constant, and L_D is a length scale derived from modeling assumptions. Based on the different models of Parkin and Kermeen (1963), Brennen (1969), and Parking and Ravindra (1991), L_D , takes different forms as shown below.

If molecular diffusion is the dominant mechanism (Parkin and Kermeen (1963)), then

$$L_{DPK} = \sqrt{DL_C/U_C} \tag{2.2}$$

where D is the molecular mass diffusion coefficient, and k_B = 2.25. This model corresponds to a Schmidt number, $S_C = \upsilon/D$, at the cavity interface of zero, where υ is the liquid kinematic viscosity. For turbulent diffusion at the cavity interface with a turbulent $S_{C_t} = \upsilon/D_t = 1$, where D_t is the turbulent diffusivity, Brennen predicted that

$$L_{DB} = \sqrt{L_C\theta} \tag{2.3}$$

with k_B = 0.45. Similarly, Parkin and Ravindra (1991) modified their laminar diffusion model by employing a turbulent diffusivity:

$$L_{DPR} = \sqrt{L_C \delta} \tag{2.4}$$

with k_B = 0.18. Note that since $\theta \approx \delta/10$ for a developed turbulent boundary layer, the modified Parkin model and the Brennen model are nearly equivalent. Finally, if we assume that the turbulent Schmidt number is very large, $S_{C_t} = \upsilon/D_t$ >>1, we can derive the Slug Flow model:

$$L_{DSF} = \delta \tag{2.5}$$

with k_B = 1. We assume here that all the gas in the boundary layer above the cavity rapidly enters the cavity.

Yu and Ceccio (1997) measured diffusion produced bubble populations downstream of a stable partial cavity, computed the gas flux, and compared the observed and predicted gas flux. They found that the molecular diffusion model significantly underestimated the gas flux, as expected. But, the models that assumed turbulent mass diffusion at the cavity boundary overestimated the rate of gas diffusion by at least two orders of magnitude. Subsequent to these measurements, researchers have shown that the void fraction in partial cavities can vary widely, ranging from a few percent gas-fraction to near unity (Stutz and Legoupil, 2003; Coutier-Delgosha *et al.*, 2007).

2.2 Present study

In the present work, gas diffusion scaling is revisit with a new set of measurements that include the volume fraction of the cavitating region, α_C. Figure 2.2 illustrates the flow around a partial cavity that is comprised of a bubbly mixture with $0 < \alpha_C < 1$. The void fraction and static pressure within the separated cavity may vary, and there is liquid flow into and out of the cavity. Hence, new scaling that considers the gas diffusion that can take place within the bubbly mixture is proposed. For this scaling, the cavity size is based on a size of a 5% void fraction contour, and for simplicity the bubble size and pressure are taken to be constant within this contour. Then, the measured and predicted gas diffusion rates using previous and newly developed scaling are compared.

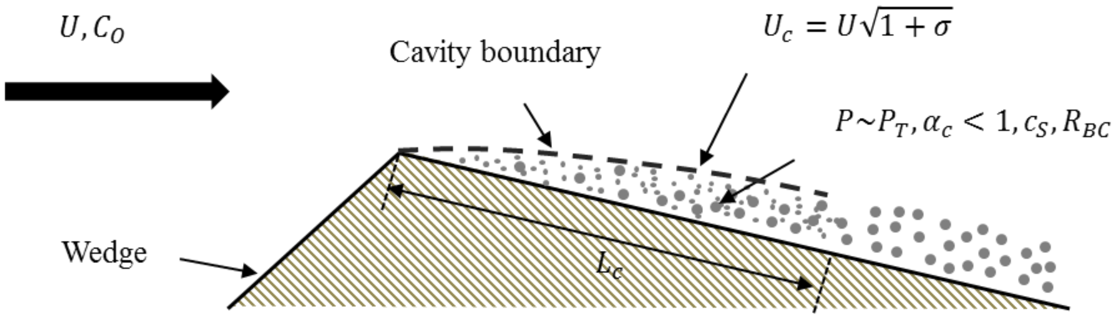

Figure 2.2 Schematic drawings of the partial cavity flows: Representation of the cavity as a bubbly mixture

2.3 Roadmap

First part of the thesis will be mapped in the following order. Experimental setup is introduced in Chapter 3. Properties and description of water channel, instruments for measurements, inflow conditions, and imaging system are presented in Chapter 3. Chapter 4 contains results from the experiment; Gas mass flux in the wake due to injected air into the cavity, mass flux of the non-condensable gas diffused into the cavity and scaling of the gas dissolution rate. Moreover, discussion on scaling of gas diffusion into limited partial cavities is presented in Chapter 4.

CHAPTER 3

Experimental Setup

3.1 9-inch Water Channel

The experiments were performed in the University of Michigan's 9-Inch Water Tunnel. The tunnel has square test section that is $21\ \mathrm{cm}$ by $21\ \mathrm{cm}$ with chamfered corners. In this study, the test section was reduced in $7.62\ \mathrm{cm}$ by $7.62\ \mathrm{cm}$ in order to facilitate X-ray measurements. The flow speed and pressure in the test section can be independently controlled. The flow speed can vary from 0 to $18\ \mathrm{m/s}$ and the static pressure near vacuum to $100\ \mathrm{kPa}$ gauge pressure. Also, de-aeration system enables to control the dissolved gas content of liquid flow.

Limited partial cavities in water were created at the apex of a wedge. Dimensions and location in the test section of the wedge are specified in Figure 3.1.

3.2 Instruments

3.2.1 Measurement of inflow conditions

The static pressure at the entrance to the test section, marked in Figure 3.1, is measured using absolute pressure transducer (Omega PX203-030A5V). And flow speed was measured using differential pressure transducer (Omega PX409-030DWU10V), which is also marked in Figure 3.1. The incoming average flow speed, U, was set at $8 \pm 0.2\ \mathrm{m/s}$. The flow speed near the cavity interface, just downstream of the wedge apex where the cavity formed (the throat speed), estimated from the inlet flow speed is $U_C = 12\ \mathrm{m/s}$. The freestream static pressure, P, was varied to change the freestream cavitation number:

$$\sigma = \frac{P - P_V}{\frac{1}{2}\rho U^2} \tag{3.1}$$

where P_V is the liquid vapor pressure, and ρ is the liquid density. The uncertainty in the cavitation number is ± 0.2. The freestream temperature was in the range of 24 ±1℃.

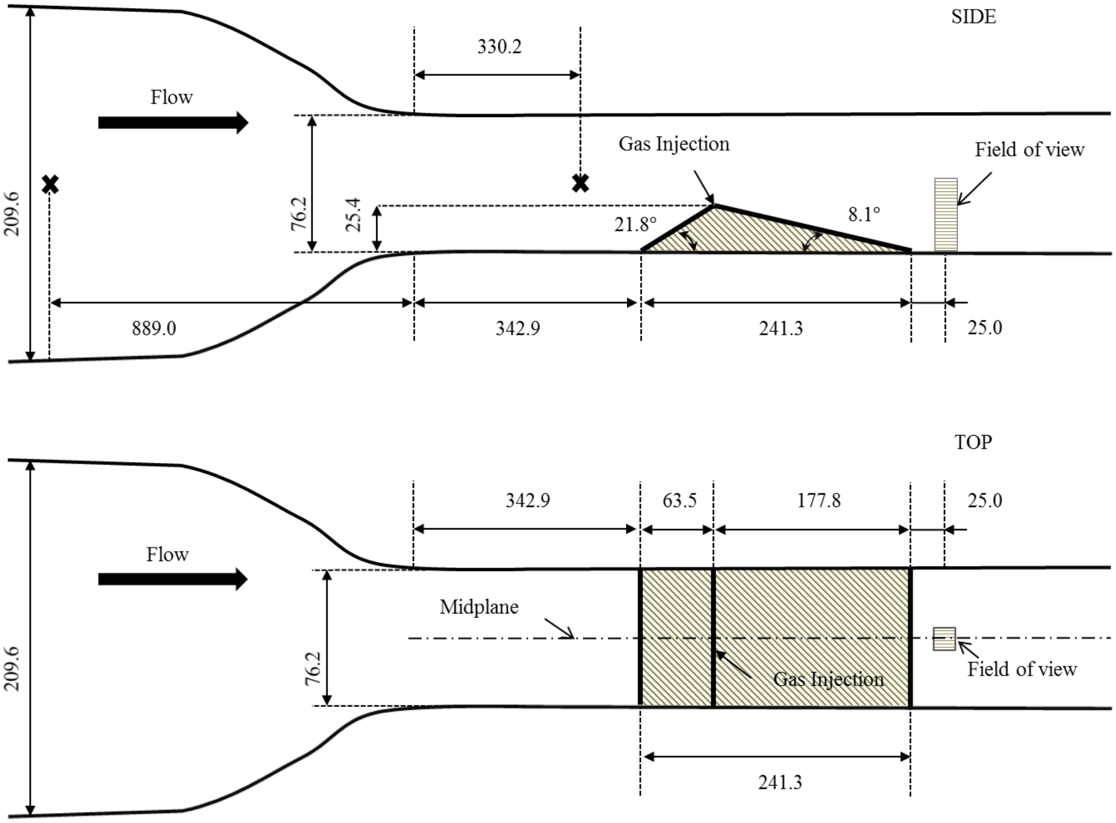

Figure 3.1 Top and side schematic views of the wedge in the test section of the water channel. All dimensions are in millimeters. "X" mark indicates locations of the pressure taps used to measure the free stream pressure, *P*, and average flow velocity, *U*.

A de-aeration system was used to change the dissolved gas content of liquid flow. The dissolved oxygen content was measured using a Dissolved Oxygen meter (Thermo Scientific Orion Star). As discussed in Yu and Ceccio (1997), the dissolved oxygen content is related, but not equivalent, to the dissolved air content of the flow. However, we will assume that the percentage of dissolved oxygen saturation is similar to the percentage of dissolved total air concentration, and that the ppm of Nitrogen is 1.8 that of Oxygen, which is an approximation discussed in Yu and Ceccio (1997). From this, we can determine the level of saturation at various pressures with Henry's law constant for air such that for a given pressure (at 24 ℃) is $c_S = 0.23P - 0.50$, where the P is in kPa and c_S is in kg/m^3.

3.2.2 Air injection system

Air was injected at the apex of the wedge to validate the measurement of the gas flux, as discussed below, section 3.4.3. The air was metered using a mass flow meter (Omega FMA 6707), and the mass flux of air was known to an uncertainty of $\pm 2.0 \times 10^{-4}\ \mathrm{g/s}$ at 24℃.

3.2.3 X-ray densitometry

The void fraction of the partial cavity was measured using a two-dimensional time resolved x-ray densitometry system. Completed description of the system is provided by Mäkiharju *et al.* (2013). A brief description of it is followed. A fan beam of x-rays from a $150\ \mathrm{kV}\ 433\ \mathrm{mA}$ source passed through the measurement domain, wherein it is attenuated according to the Beer-Lambert law. After the measurement domain, the beam encounters a two-dimensional imager consisting of an x-ray image intensifier coupled to a high-speed camera (Vision Research Phantom V9.0). The light intensity distribution measured by the camera can then be related back to a spanwise averaged projection of the void fraction in the measurement domain.

3.3 Inflow conditions

As discussed earlier, inflow conditions were controlled and measured. Incoming average flow speed, U, was fixed at $8 \pm 0.2\ \mathrm{m/s}$. Total 15 cases were measured with different dissolved oxygen contents and cavitation number (by changing static pressure of freestream). 3 cases with $L_C = 0cm$ at each dissolved oxygen contents were to measure mass flux at no cavitation. Table 3.1 summarized test matrix.

Parameter	**Range**	**Note**
$\boldsymbol{U}\ (\mathbf{m/s})$	$\mathbf{8 \pm 0.2}$	
$\boldsymbol{P}$ (**kPa**)	**78 ~ 125** $\pm$ **0.3**	
DO (%)	**30, 50, and 70**	
$\boldsymbol{\sigma}$	**2.3 ~ 3.3** $\pm$ **0.2**	$\boldsymbol{\sigma = \frac{P - P_V}{\frac{1}{2}\rho U^2}, P_V = 3}$ **kPa**

Table 3.1 Test matrix of Mass flux of the non-condensable gas diffused into the cavity

3.4 Imaging system

3.4.1 Camera setup and processing parameters

Bubble populations were measured downstream of the cavity using a high magnification imager coupled to a high-speed digital video camera. A Phantom V710 camera was used with a Questar QM 100 Photo-Visual Long Distance microscope as a high magnification imager. This coupled system was fixed on a stage that could be translated in three directions with 1 mm increment (flow direction, vertical direction, and spanwise direction). Target was backlit with ARRI light (ARRILUX 400) lighting system. Videos were taken at six different vertical (cross stream) locations from the bottom flow boundary with 8 mm intervals, focusing at the center plane in depth direction at fixed distance 2.5 cm from the wedge. Videos were taken with 800×600

of resolution, 13,000 fps of sampling rate, 1 to 5 µs of exposure time, and 2 seconds of acquisition time. The depth of field of the imaging volume was determined by traversing a target across the focal plane. The depth of field was found to be 320 µm, as defined by the thickness across the place where a sharp boundary was in focus to within 112 pixels resolution on the image. Figure 3.2 shows a schematic of the camera setup and the processing parameters.

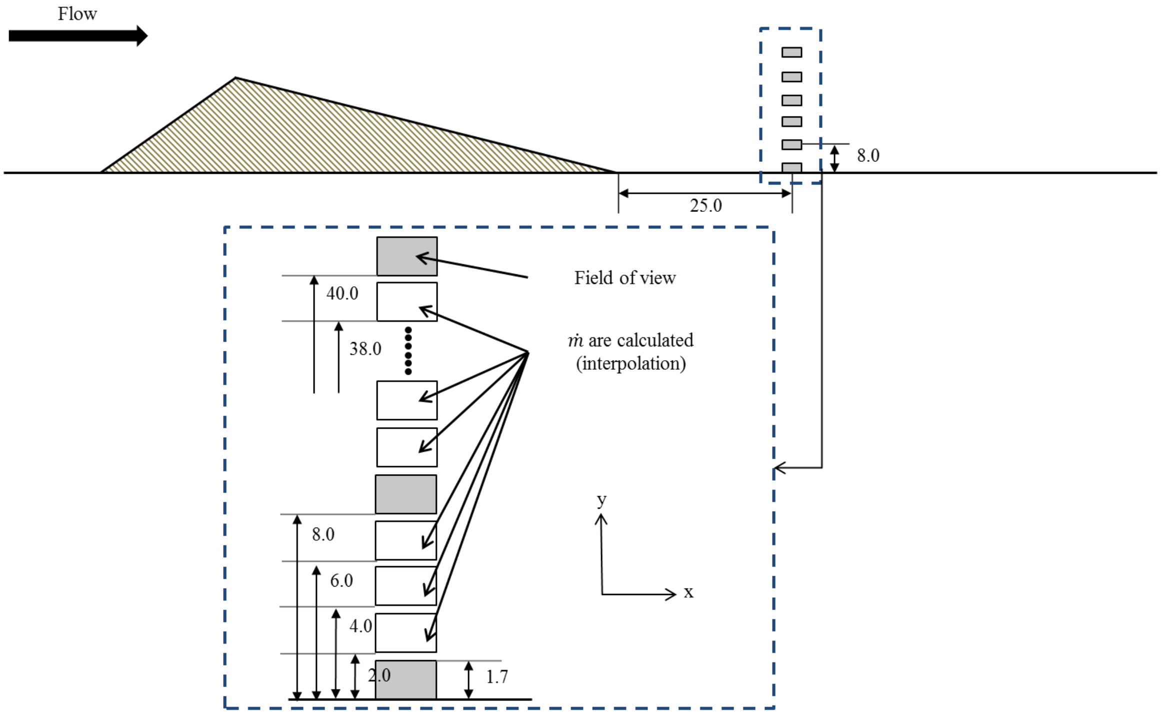

Figure 3.2 Detailed view of the fields of view used to determine the void fraction profiles in the wake of the wedge. All dimensions are in millimeters.

3.4.2 Measurement of bubble population

As discussed earlier, video were taken at six different vertical locations for single condition. From the video, consecutive images were chosen such that the images did not contain the same bubbles (*e.g.* they were not correlated). Chosen images were converted to grey scale and median filtered. Mean image through whole video was subtracted from filtered images in order to remove the background. Using edge detecting, the edge of the bubbles was determined. Detected bubbles were sorted by their mean intensity, size, eccentricity, and distance of their centroid from the edge of the image. Those values were used to filter non-bubble particle (mean intensity and eccentricity) and bubbles clipped at the edge (distance of their centroid from the edge of the image).

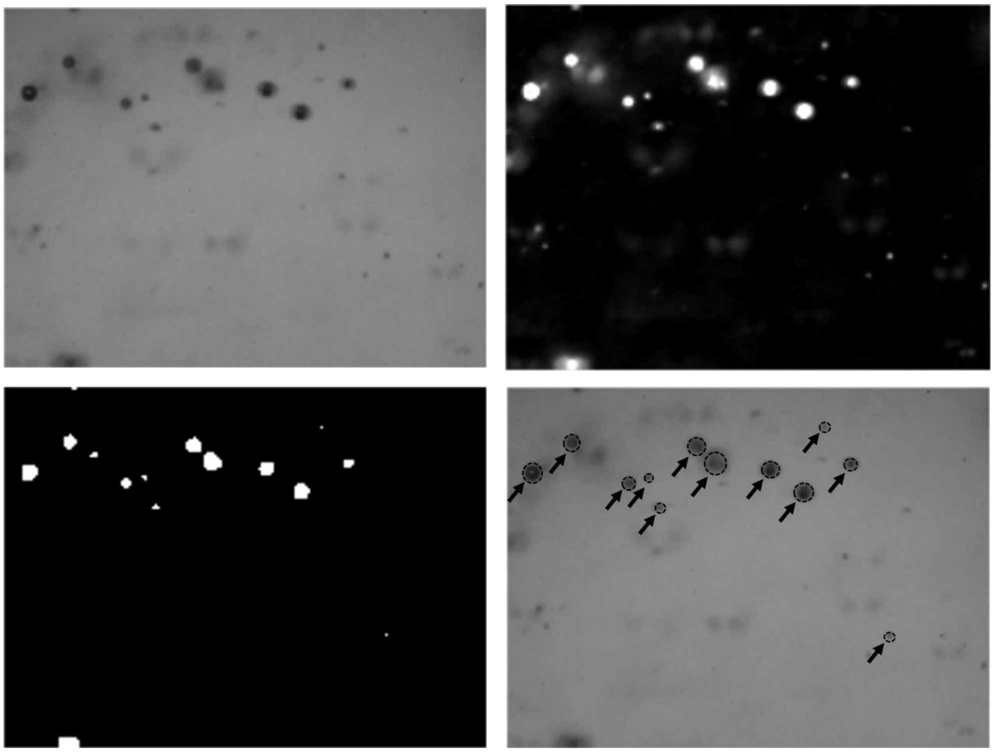

Figure 3.3 Step of image processing using MATLAB. (Left/Top) Original image, (Right/Top) Image after background subtraction and median filtering, (Left/Bottom) Image converted into Black and White, and (Right/Bottom) Original image with detected bubble marked.

The diameter of the filtered bubble is the average of distances between edge of the bubble in x, y, and two diagonal directions. Image processing was performed using a routine in MATLAB. Example of image process is shown in Figure 3.3. Starting from original image located on the left-top, image after background subtraction and median filtering is on the right-top. Image on the left-bottom has been converted into

Black/White after edge detection. At last, right-bottom image is the original image with detected/filtered bubble marked.

To estimate the size of the bubble, images of resolution target were taken with the system to calibrate the size of a pixel ($2.86\ \mu\text{m/pixel}$). Bubbles were counted only when they were equivalent or bigger than 2×2 pixels. Hence the minimum resolvable bubble size (diameter) was $5.7\ \mu\text{m}$. The bubble velocity was assumed to be equal to flow velocity. Bubbles were chosen randomly in the video, and their velocities were calculated by computing the bubble displacement for a fixed time period (*e.g.* the frame rate). At least 10 bubbles were selected in the video, and average of their velocities was used.

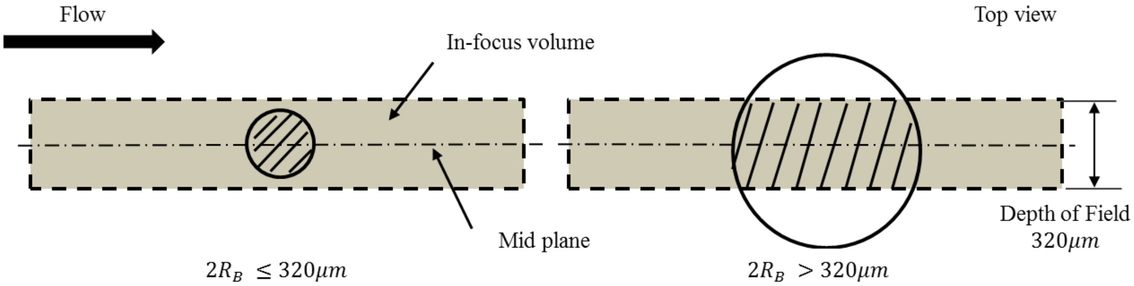

Figure 3.4 Description of bubble location in the in-focus volume. Bubble with diameter smaller than depth of field (left) considers whole portion when calculating bubble volume. Bubble with diameter bigger than depth of field (right) considers only the portion, hatched part, inside the in-focus volume. Dotted border box refers in-focus volume.

The gas volume fraction at the imaging location was estimated after estimating in-focus volume of the image to be $1.25\ \text{mm}^3$, considering the known depth of field of the image of $320\ \mu\text{m}$. The gas volume was estimated after measuring the diameter of bubble. We assume that (1) the detected bubbles are spheres, (2) only the portion of the volume inside the focused volume contributes to the volume fraction, and (3) for the centroid of the bubble with diameter bigger than depth of field, $320\ \mu\text{m}$, is on the midplane. Figure 3.4 describes assumptions. Total gas volume in the wake was sum of measured gas volume at six locations and calculated gas volume at locations in between the six locations. Gas volume at three virtual locations in between actual measurement location was calculated by linear interpolation. Focused volume at virtual locations is assumed to be equivalent with locations actually measured. In the dotted border box on Figure 3.2, two different locations are described. The average void fraction in the wake, α_W, is then given by the total gas volume (six actual measurement and fifteen calculation) divided by the in-focus measurement volume ($21 \times 1.25mm^3 = 26.25mm^3$).

3.4.3 Calibration of measurement: Gas mass flux in the wake due to injected air into the cavity

In order to validate the optical measurement of the gas flux behind the cavity, a known mass flux of air, $\dot{m}_{INJ}$, was injected into the wedge apex under non-cavitating conditions. The mass flux on the gas downstream of the cavity, $\dot{m}_B$, was determined using the optical measurements by: (1) measuring the bubble populations and mean bubble speeds at 6 measurements locations above the bottom wall of the test section, (2) determining the local void fraction at each location, (3) determining the non-condensable mass flux after correcting for the local static pressure, Laplace pressure and the percentage of water vapor in the bubble. The pressure of the non-condensable gas within each bubble of radius R_B is given by

$$P_{G_O} = P_W - P_V + \frac{2S}{R_B} \tag{3.2}$$

where P_W is the static pressure in the measurement location downstream of the wedge, and S is the surface tension. The mass of the non-condensable gas in each bubble is then

$$m_B = \frac{4}{3}\pi R_B^3 \frac{P_{Go}}{\mathbf{R}T} \tag{3.3}$$

where **R** is the ideal gas constant (assumed to be that for air), and T is the temperature. Note that the pressure in the measurement location downstream of the wedge has recovered to well above vapor pressure, and the bubbles are largely composed of non-condensable gas.

Figure 3.5 presents the time averaged void fraction in the wake, non-condensable mass fraction, and gas-phase velocity profiles downstream of the wedge for two cases of gas injection without cavitation. Both data sets were curve fit to provide analytical expressions that could be integrated to determine the gas volume flux. The void fraction profile was fit with a log-normal distribution, and the velocity fitted with a power-law profile. Figure 3.6 shows the bubble size distributions. Table 3.2 shows the results from two gas injection experiments, where $\langle R_B \rangle$, is the average bubble radius, and α_W is the average void fraction in the wake.

$\boldsymbol{\sigma}$	$\dot{\boldsymbol{m}}_{\boldsymbol{INJ}}$ **(g/s) x 10^3**	$\langle \boldsymbol{R_B} \rangle$ **(µm)**	$\boldsymbol{\alpha_W}$ **x 10^4**	$\dot{\boldsymbol{m}}_{\boldsymbol{B}}$ **(g/s) x 10^3**	$\dot{\boldsymbol{m}}_{\boldsymbol{B}}/\dot{\boldsymbol{m}}_{\boldsymbol{INJ}}$
2.4 ± 0.2	**2.5 ± 0.2**	**62 ± 3**	**6.2 ± 0.3%**	**7.2 ± 0.3%**	**2.9**
2.4 ± 0.2	**6.4 ± 0.2**	**79 ± 3**	**16.0 ± 0.3%**	**18.5 ± 0.3%**	**2.9**

Table 3.2 Comparison of the injected and measured non-condensable gas flux

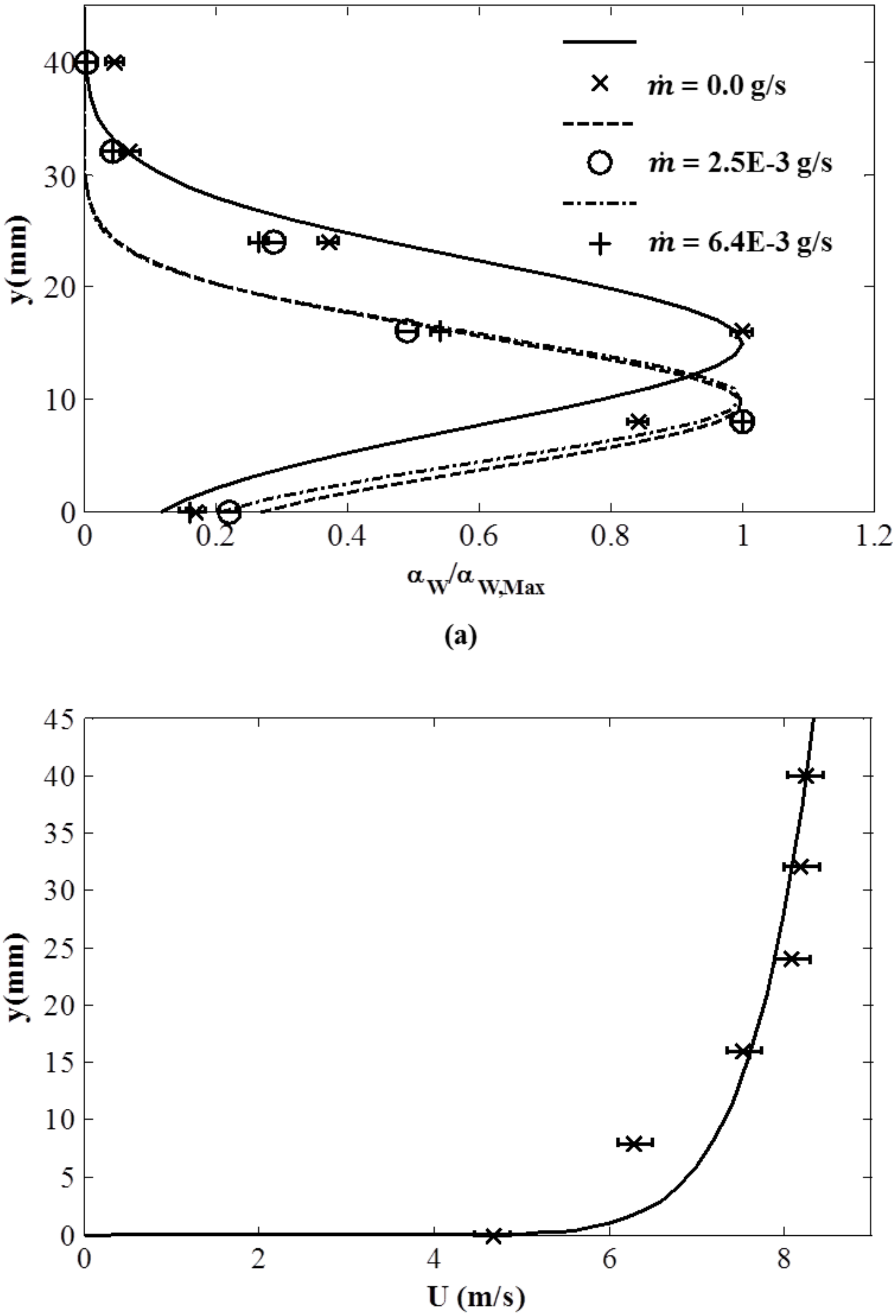

(a)

(b)

Figure 3.5 Profile of void fraction and gas-phase velocity are plotted with error bars and fitted curve.

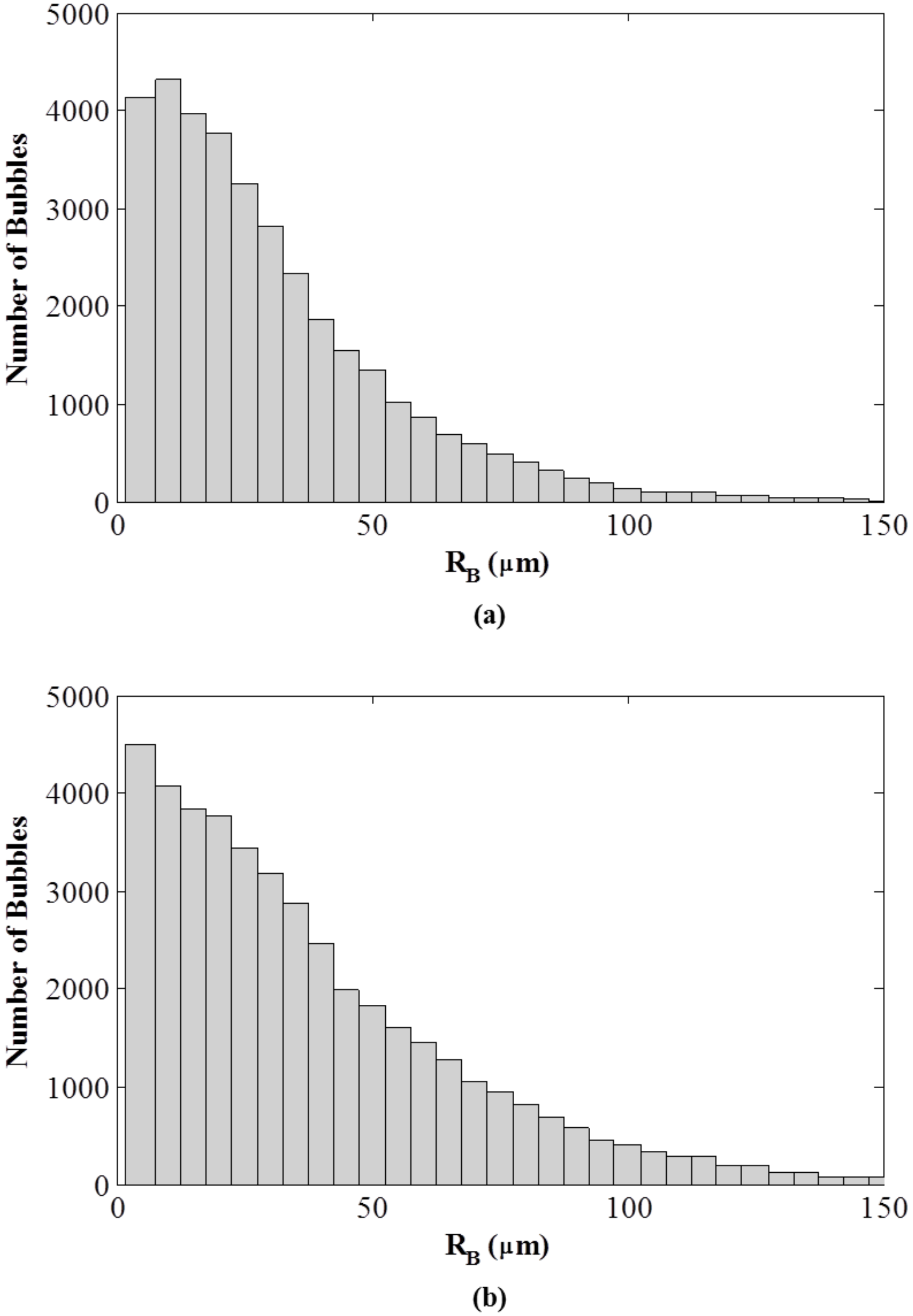

Figure 3.6 The measured bubble size distributions for the case of injected air at the wedge apex for injected gas flux of (a) $2.5 \times 10^{-3} g/s$, and (b)$6.4 \times 10^{-3} g/s$. Data were collected form 6,500 independent frames for each case, at σ=2.4.

3.4.4 Uncertainty of bubble population measurement

In Table 3.2, the optical measurement of the void fraction and resulting gas flux is over-estimated by approximately a factor of 3 in both cases. This is likely due to method of determining the effective thickness of the measurement volume and assumptions of the bubble location inside the in-focus volume. Assumption (1), the detected bubbles are spheres, and assumption (3), the centroid of the bubble with diameter bigger than depth of field, $320\,\mu\mathrm{m}$, is on the midplane, both maximize the bubble volume. In the following results, we will reduce the optically measured gas flux produced by the purely cavitating flow by 1/3.

CHAPTER 4

Results and Discussion

4.1 Mass flux of the non-condensable gas diffused into the cavity

The gas flux in the wake of the partial cavity was measured without the injection of any air into the cavity. Care was taken to ensure that no non-condensable gas was present in the gas injection system; hence, the bubble populations present downstream of the cavity were comprised of bubbles that may have been present upstream of the cavity and/or bubbles created by dissolution of dissolved gas into the low-pressure zone of partial cavitation near the wedge apex.

Once again, the freestream velocity was fixed at $U = 8\ \mathrm{m/s}$, but the freestream cavitation number was varied to create partial cavities of different lengths. In Figure 4.1, first two images show photographic image of the cavitating wedge for the case of $L_C = 2.0$ cm corresponding to $\sigma = 2.5$, and bottom image shows the void fraction field from the x-ray visualization. Note that the average void fraction of the cavity is a few percent.

The cavity length and volume fraction were measured using x-ray densitometry. Note that we are using the x-ray defined cavity length, defined by the extent of the cavity that is greater than 5% void fraction, and the volume is the region that is greater than 5% void fraction. The average void fractions range from $0\% < \alpha_C < 15\%$ for the range of

$0 < L_C < 4$ cm. Figure 4.2 shows the average cavity length, volume, and void fraction versus cavitation number.

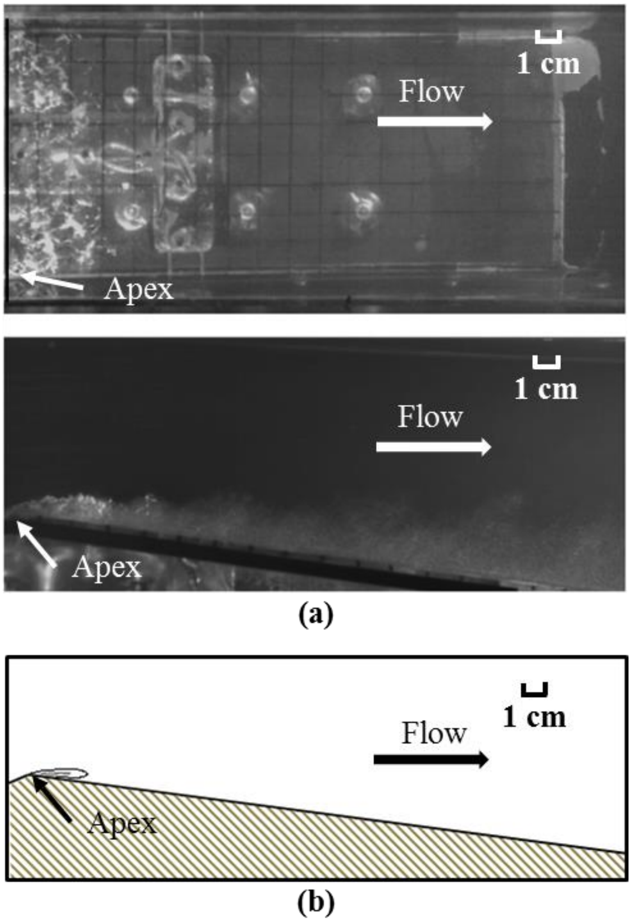

Figure 4.1 Both images are cavitating wedge with L_C=2cm, and σ=2.5. (a) Top and side photographic images and (b) Void fraction field for the cavitating flow. Inner contour is void fraction 15% and outer contour is void fraction 5%.

The bubble populations downstream of the cavities were examined for three different freestream dissolved gas concentrations, c_O, corresponding to oxygen saturation levels of 30%, 50%, and 70% at atmospheric pressure. At the highest pressure (σ = 3.8), there is no cavitation, and any bubbles measured are part of the background nuclei population. With a reduction in pressure, the cavity forms, and small bubbles can then be observed to persist in the cavity wake, even in the region of pressure recovery downstream of the wedge. Further reduction in pressure corresponds to both an increase in the cavity length and the number of bubbles observed in the cavity wake. Over the range of cavitation numbers tested ($\sigma > 2.0$), the cavity was relatively stable in length (*i.e.* a closed partial cavity), as compared to a cavity that is shedding large clouds (Laberteaux and Ceccio, 2001).

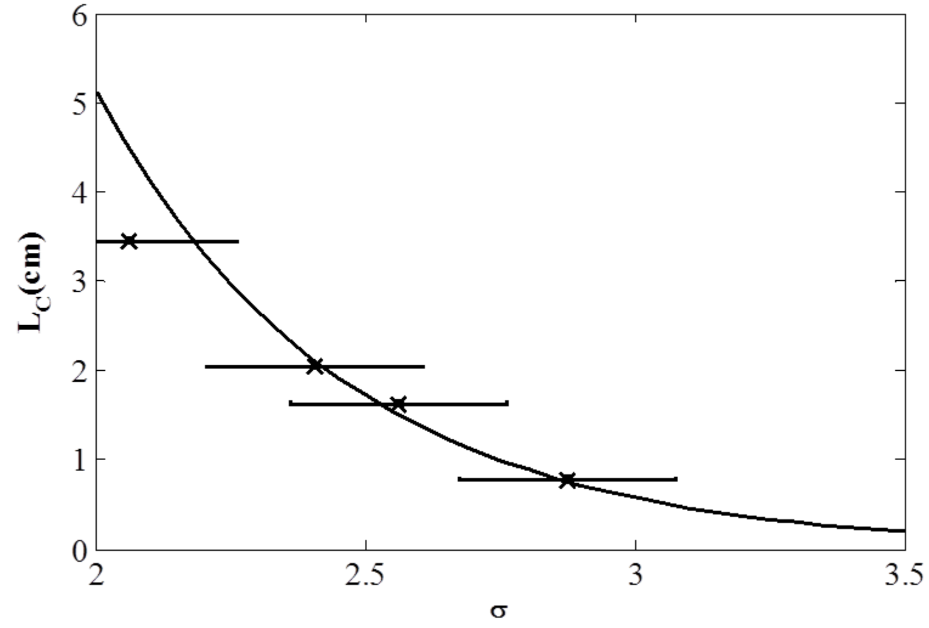

(a)

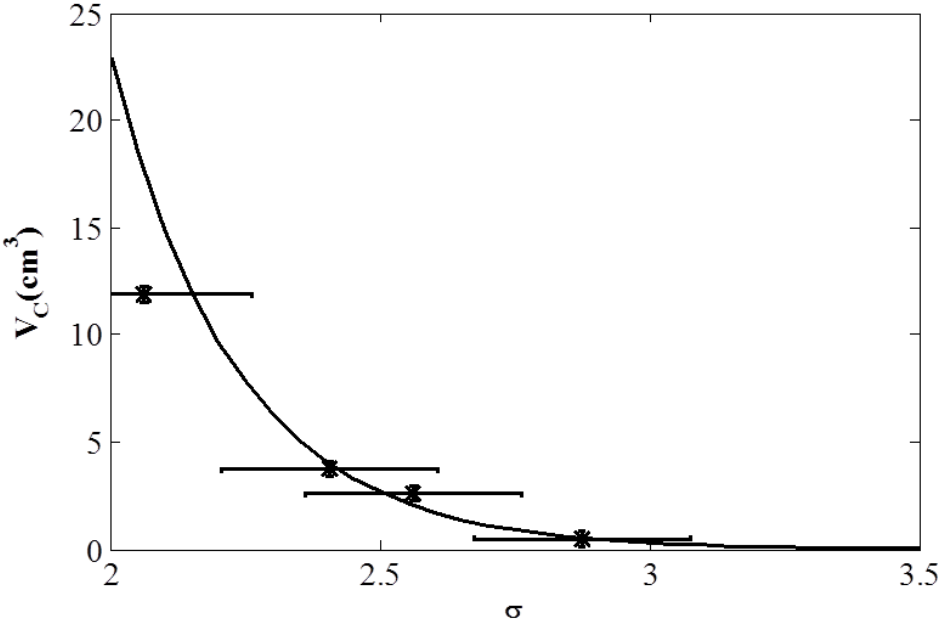

(b)

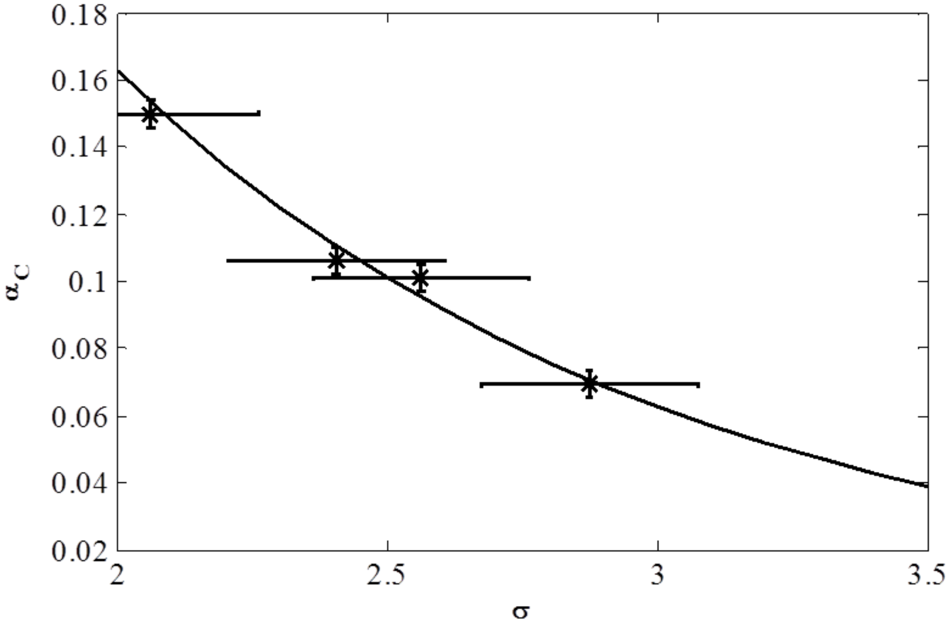

(c)

Figure 4.2 (a) The average cavity length, L_C (b) volume, and (c) void fraction α_C as a function of cavitation number, σ. The curve fits are shown that were used to compute values for scalings. (a) Uncertainty of average cavity length is ±0.03cm.

Figures 4.3 presents the bubble size distributions for varying gas saturation and pressure, along with the average bubble size. As expected, both the average bubble size and the number of bubbles increase with increasing oxygen saturation level. As before, the velocity and void fraction profiles were curve fitted to allow for integration to determine the void fraction. Table 4.1 presents the measured results.

DO%	σ	L_C (cm)	α_C x 10^2	$c_O - c_S$ (ppm)	#Bubbles (2 s)	$\langle R_B \rangle$ (µm)	α_W x 10^6	$\dot{m}_B$ (g/s) x 10^7
30	**3.0**	**0.6**	**6.5**	**-5.8**	**459**	**18**	**0.05**	**2**
30	**2.7**	**1.1**	**8.5**	**-3.7**	**564**	**16**	**0.10**	**5**
30	**2.4**	**2.1**	**11.1**	**-1.7**	**2,534**	**19**	**0.61**	**27**
30	**2.3**	**2.6**	**12.1**	**-1.0**	**2,661**	**19**	**0.70**	**31**
50	**3.0**	**0.6**	**6.3**	**-1.4**	**429**	**16**	**0.04**	**2**
50	**2.7**	**1.1**	**8.5**	**1.0**	**2,923**	**18**	**0.61**	**27**
50	**2.3**	**2.4**	**11.7**	**3.5**	**11,534**	**27**	**9.67**	**423**
50	**2.3**	**3.0**	**12.8**	**4.2**	**16,705**	**32**	**24.8**	**1064**
70	**3.3**	**0.3**	**4.8**	**1.3**	**252**	**16**	**0.07**	**3**
70	**3.0**	**0.7**	**6.7**	**3.8**	**2,749**	**19**	**0.61**	**26**
70	**2.7**	**1.2**	**8.7**	**5.9**	**9,575**	**25**	**6.12**	**249**
70	**2.3**	**2.4**	**11.7**	**8.2**	**23,537**	**39**	**67.4**	**2805**

Table 4.1 The measured bubbly non-condensable gas flux in the cavity wake from natural cavities for varying cavitation number and dissolved oxygen content. The gas flux measured for the under-saturated cases are shown in bold.

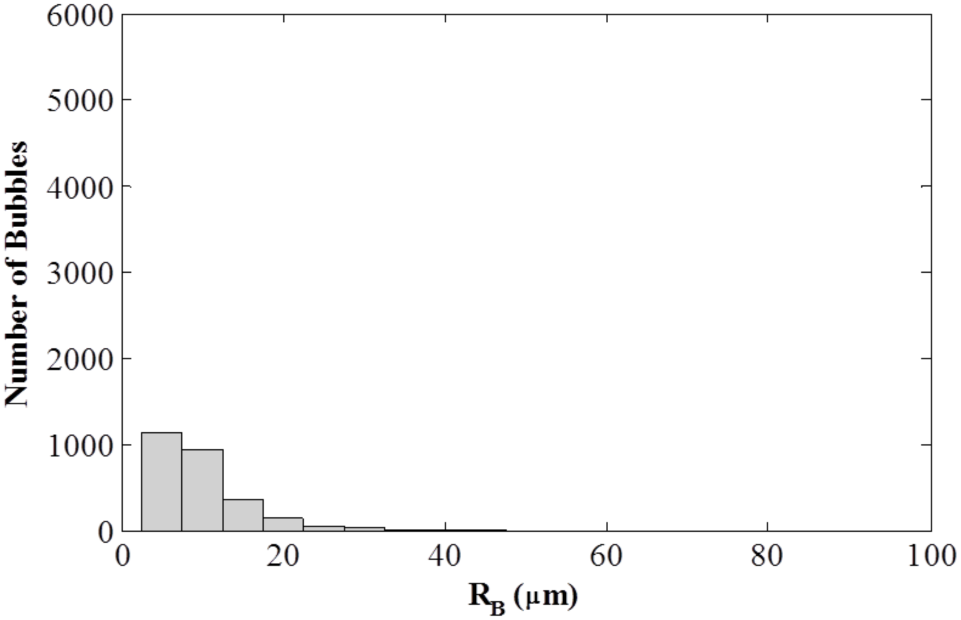
6000
5000
4000
3000
2000
1000
0
Number of Bubbles
0
20
40
60
80
100
R_B (μm)

(a)

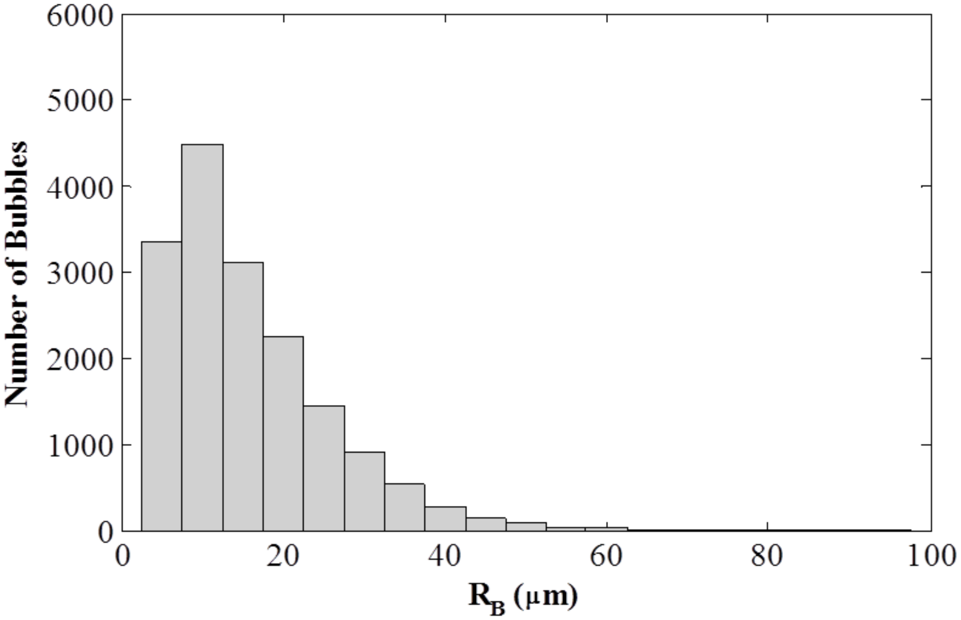
6000
5000
4000
3000
2000
1000
0
Number of Bubbles
0
20
40
60
80
100
R_B (μm)

(b)

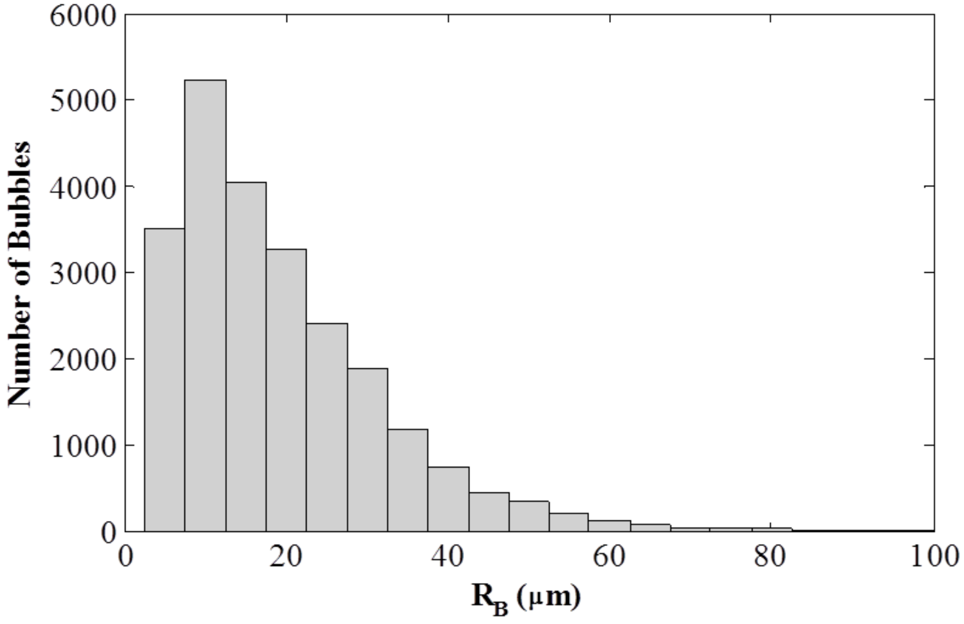

(c)

Figure 4.3 The measured bubble populations in the cavity wake for dissolved oxygen contents of (a) 30% σ=2.3, (b) 50% σ=2.3, and (c) 70% σ=2.3. Data were collected from 6,500 images.

The measured gas flux as a function of cavitation number is plotted in Figure 4.4. Data are presented for the non-cavitating cases ($L_C = 0$) to illustrate that the baseline gas flux due to the freestream nuclei population passing over the wedge is around 7×10^{-7} g/s. With the reduction in freestream pressure and the onset of cavitation, the gas flux increases by three orders of magnitude over the range of cavitation numbers tested. Note the sharp increase in the rate of gas flux when cavity flow changes from under-saturated ($c_O - c_S < 0$) to super-saturated ($c_O - c_S > 0$) based on the level of saturation in the free stream and the pressure at the apex of the wedge (*i.e.* the throat pressure). It is interesting to note that there is still outgassing and bubble production even when the average cavity flow is under-saturated, although the rate is much lower compared to the super-saturated conditions. This will be discussed in the next section.

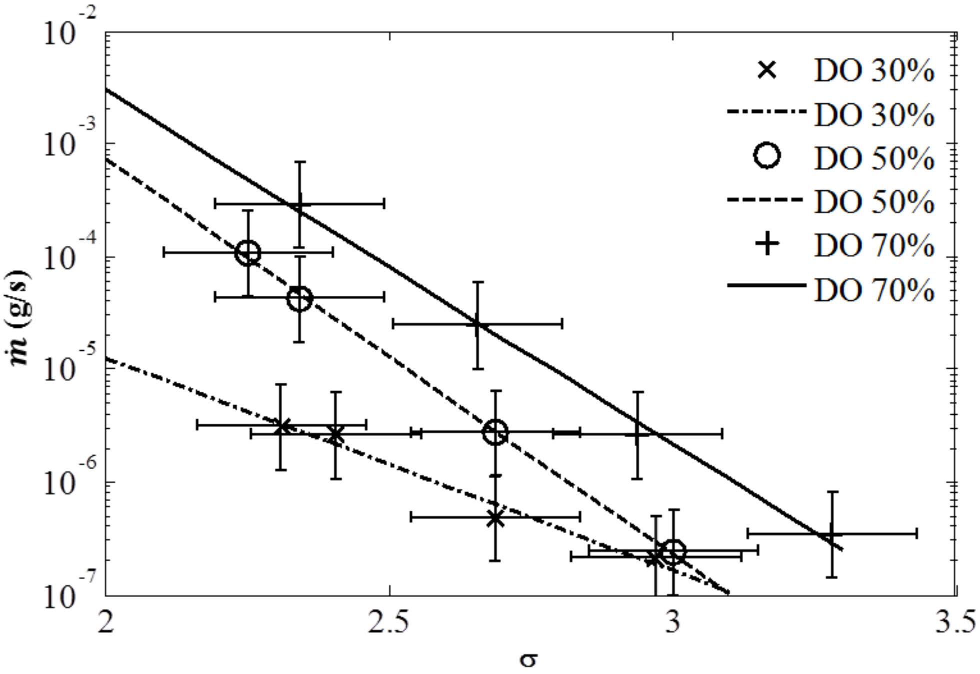

Figure 4.4 The measured net gas flux, $\dot{m}_B$, produced as a result of diffusion into the partial cavity as a function of cavitation number, σ. The uncertainty shown in $\dot{m}_B$ represents the span between 2 times and 0.5 times the values measured values.

4.2 Scaling of the gas dissolution rate

First, the measured gas flux data can be compared to the predicted gas flux from the previous models where the cavity was assumed to be a gas pocket at vapor pressure. Table 4.2 presents the scaled and measured gas diffusion rates. We compare the models of Parkin and Kermeen (1963)(with $D = 2 \times 10^{-5}\ \mathrm{cm}^2/\mathrm{s}$), Parkin and Ravindra (1991) (with $\delta = 1$ mm), and the Slug Flow Model.

DO%	σ	L_C (cm)	$c_O - c_S$ (ppm)	$\dot{m}_B$ (g/s) x 10^7	$\dot{m}_{BPK}$ (g/s) x 10^7	$\dot{m}_{BPR}$ (g/s) x 10^7	$\dot{m}_{BSF}$ (g/s) x 10^7
30	3.0	0.6	-5.8	2	-153	-30,200	-53,100
30	2.7	1.1	-3.7	5	-139	-27,500	-34,200
30	2.4	2.1	-1.7	27	-82	-16,300	-15,300
30	2.3	2.6	-1.0	31	-52	-10,200	-8,960
50	3.0	0.6	-1.4	2	-36	-7,040	-12,400
50	2.7	1.1	1.0	27	4	6,970	8,660
50	2.3	2.4	3.5	423	171	33,900	31,800
50	2.3	3.0	4.2	1064	219	43,400	38,100
70	3.3	0.3	1.3	3	3	6,580	11,600
70	3.0	0.7	3.8	26	18	23,400	34,700
70	2.7	1.2	5.9	249	218	43,200	53,600
70	2.3	2.4	8.2	2805	401	79,500	74,600

Table 4.2 The measured gas flux, $\dot{m}_B$, and scaled gas flux from natural cavities for varying cavitation number and dissolved oxygen contents, employing the previously proposed scaling models; $U_C = 12m/s$, and δ=1mm; "PK", "PR", and "SF" refers to the models of Parkin and Kermeen (1963), Parkin and Ravindra (1991), and the Slug Flow model (Parkin and Ravindra (1991)).

Comparing the cases with super-saturated flow at the cavity interface, the results of Table 4.2 indicate that laminar diffusion model under-predicts the gas diffusion rate by one order of magnitude, while the models that assume turbulent diffusion at the cavity interface over-estimate the gas diffusion by up to two orders of magnitude. These observations are consistent with those of Yu and Ceccio (1997), and they motivate a reexamination of the basic scaling assumptions. Moreover, the data presented in Figure 4.4 illustrate that the gas flux increases exponentially with cavitation number, while these models predict a much slower rate of increase with decreasing cavitation number.

It is clear from the void fraction measurements that the mean cavity void fraction is much less than unity for these flows and a free surface does not exist at the cavity interface. Hence, gas diffusion is not taking place at a stratified gas-liquid interface, but within a low-pressure bubbly zone. We therefore expect that we must include the cavity void fraction, α_C, in the scaling.

The cavity is a recirculating bubbly mixture, with freestream fluid continually being entrained and expelled in the cavity wake. Bubbles within the cavity region grow via gas diffusion as they reside in the low-pressure regions where the flow is locally super-saturated, and then they are expelled from the cavity as the bubbly flow is entrained in the cavity closure. We first consider the gas diffusion rate into a single bubble, $\dot{m}_{SB}$, in the recirculating zone. The rate of ingassing into an individual bubble is scaled by the following relation, following that of Epstein and Plesset (1950):

$$\dot{m}_{SB} = 4\pi D R_{BC}^2 (c_O - c_S)/L_{D\delta} \tag{4.1}$$

where R_{BC} is the average bubble radius within the cavitating region, and $L_{D\delta}$ is a length scale related to the local diffusion boundary layer at the bubble surface. The total amount of in-gassing per unit volume of the cavity is related to the number of bubbles, N_B, the cavity volume, V_C, and the residence time of the bubbles in the super-saturated region pressure, t_b:

$$M_B = \dot{m}_{SB} N_B t_B / V_C \tag{4.2}$$

where

$$N_B = \alpha_C V_C / \tfrac{4}{3}\pi R_{BC}^3 \tag{4.3}$$

and α_C is the average cavity void fraction. The residence time of the bubbles in the cavity is related to the cavity volume and the net volume flux of flow in and out of the cavity:

$$t_B = V_C / q_C \tag{4.4}$$

Thus, the net mass flux of gas out of the cavity will be given by

$$\dot{m}_{B,Sat} = M_B q_C = \frac{3\alpha_C V_C D(c_O - c_S)}{R_{BC} L_{D\delta}} \tag{4.5}$$

Note that $3\alpha_C V_C / R_{BC}$ is the interfacial area of the bubbles within the cavity. Interestingly, the flow speed over the cavity does not appear directly in this scaling, since the flux of liquid in and out of the cavity would increase with increasing speed, while the residence time for bubbles in the cavity will decrease with increasing speed. As the cavitation number decreases, the cavity volume, void fraction, and concentration difference all increase. Hence, this scaling yields an exponential growth in the gas diffusion, as observed in the measured bubble populations.

We can modify this scaling for the cases when the cavity flow is on average under-saturated, based on the average throat pressure. For limited cavities, there is still a suction peak near the position of flow separation at the wedge apex. Therefore, there may be a local portion of the cavity volume that is, on average, super-saturated. Then, the scaling would be appropriate for a smaller portion of cavity volume near the suction peak. Also, the saturation pressure would be lower and sufficient to produce in-gassing into the bubbly flow. Such a modified scaling would take the form

$$\dot{m}_{B,USat} = \frac{3\alpha_C V_{C,US} D\left(c_O - c_{S,US}\right)}{R_{BC} L_{D\delta}} \tag{4.6}$$

where the subscript "US" denotes the under-saturated condition when $(c_O - c_S) < 0$ for the average cavity pressure, but $\left(c_O - c_{S,US}\right) > 0$ in the low pressure region near the cavity separation. In this scaling, the void fraction and the level of super-saturation will increase with decreasing cavitation number, but the portion of the cavity volume where outgassing occurs would remain relatively constant, even with decreases in pressure. Hence, the rate of mass diffusion would increase with decreasing cavitation number, but at a much lower rate, as observed for the cases where $(c_O - c_S) < 0$.

To perform the scaling, we must make some assumptions. First, we assume that the average bubble radius in the cavity is of the order of $R_{BC} \sim 100$ µm. The diffusion length scale increases as $L_{D\delta} {\sim} \sqrt{\pi D t}$, and if we assume a residence time on the order of a few millisecond then $L_{D\delta} \sim 10$ µm. For the under-saturated cases, we will assume that the local suction peak leads to a pressure that is about half the average throat pressure and that the volume with the reduced pressure extends about 1 cm from the wedge apex.

Table 4.3 shows the scaled and measured gas fluxes as a function of cavitation number after employing these assumptions. The raw scaling predicts gas flux that is on the order of that of the observed values, but the effective scaling factor can be changed with changes in the assumed average bubble size in the cavity, the diffusion length scale, or other model parameters. More importantly, the scaling successfully captures increase in gas flux with lowering of the cavitation number, and this trend suggests that the basic physical reasoning behind the proposed scaling is valid.

DO%	σ	V_C **(m^3) x 10^6**	α_C **x 10^2**	$c_O - c_S$ **(ppm)**	$\dot{m}_B$ **(g/s) x 10^7**	$\dot{m}_{B,USat}$ **(g/s) x 10^7**	$\dot{m}_{B,Sat}$ **(g/s) x 10^7**	$\frac{\dot{m}_B}{\dot{m}_{B,Scaled}}$
30	**3.0**	**0.4**	**6.5**	**-5.8**	**2**	**3**		**0.7**
30	**2.7**	**1.2**	**8.5**	**-3.7**	**5**	**9**		**0.5**
30	**2.4**	**4.0**	**11.1**	**-1.7**	**27**	**19**		**1.4**
30	**2.3**	**6.0**	**12.1**	**-1.0**	**31**	**23**		**1.3**
50	**3.0**	**0.3**	**6.3**	**-1.4**	**2**	**20**		**0.1**
50	**2.7**	**1.2**	**8.5**	**1.0**	**27**		**80**	**0.3**
50	**2.3**	**5.2**	**11.7**	**3.5**	**423**		**1786**	**0.2**
50	**2.3**	**7.8**	**12.8**	**4.2**	**1064**		**3506**	**0.3**
70	**3.3**	**0.1**	**4.8**	**1.3**	**3**		**5**	**0.7**
70	**3.0**	**0.4**	**6.7**	**3.8**	**26**		**86**	**0.3**
70	**2.7**	**1.4**	**8.7**	**5.9**	**249**		**581**	**0.4**
70	**2.3**	**5.2**	**11.7**	**8.2**	**2805**		**4193**	**0.7**

Table 4.3 The measured and scaled gas flux from natural cavities for varying cavitation number and dissolved oxygen content employing the proposed scaling models for saturated and under-saturated conditions.

4.3 Conclusions

We have shown that the significant quantities of non-condensable gas bubbles can be produced in the wake of a partial cavity as a result of outgassing into the low-pressure cavitating region. Previously proposed scalings for this process have been offered that are based on the presence of a free surface at the cavity interface. However, the cavities under consideration here are not gas pockets but are, instead, bubbly mixtures. A new scaling has been proposed that captures the order of magnitude of the gas flux due to diffusion into the bubbly flow, along with the strong change in mass diffusion as a result of changing flow parameters (*i.e.* the cavitation number and dissolved gas content). This scaling is based on the average properties of the bubbly cavitating flow. However, we found that net outgassing was observed, even when the flow in the cavitating region was, on average under-saturated. We accounted for this by assuming that there may be a local region of strongly negative pressure near the cavity suction peak that leads to outgassing. Therefore, improved scaling may be devised which take into account the flow structure of the local cavity flow where both the mean and unsteady pressures may be much lower than the average cavity pressure, such as in the cavitating shear layer at the point of cavity detachment.

For further study on this research, examining quantities of non-condensable gas bubbles at higher Reynolds number is suggested. Also, understanding the bubble size distribution in wake of partial cavity is very interesting and important subject.

CHAPTER 5

Interaction of Jet of Fluid with Cross-flow

5.1 Background

Since interaction of a jet of fluid and cross-flow is very common, the phenomenon has been found in a number of previous studies. This chapter provides a background on the scientific framework for examining the interaction of a gas jet into a cross-flow of liquid. There are numerous possible combinations of fluids and flows (*i.e.* types of fluid, directions, speed range of jet and cross-flow), and the structure of jet and cross-flow interaction varies significantly by definitions. Since this study is about gas jet injection into liquid cross-flow beneath surface, only similar previous studies are presented in this summary. The first subsection of the chapter is focused on cases of a jet injected vertically (against gravity) through orifice into horizontal cross-flow. Then, cases of jet injected horizontally into vertical (along gravity) cross-flow are followed in the subsequent subsection. In the last subsection, case of jet injected vertically (along gravity) into horizontal cross-flow are presented.

5.1.1 Vertical jet injection against gravity direction into horizontal cross-flow

Investigations of jets in cross-flow are typically conducted with the jet injected against gravity (*i.e.* vertically) into a horizontal cross-flow. Most of them were focused on homogenous or single-phase jets and cross-flows emitted through a circular hole flush mounted on a flat wall. Figure 5.1 shows a schematic diagram of such a jet and a cross-flow. Speed of jet, speed of cross-flow, density of fluid of a jet and that of a cross-flow are U_i, U_∞, ρ_i, and ρ_∞, respectively. Researchers focused on the jet trajectory and the evolution of the flow along the trajectory in the earlier time, including Keffer and Baines(1963), Kamotani and Graber(1972), and Chassaing *et al.* (1974). In addition, researches on prediction of the velocity field and trajectories of the jet (Sucec and Bowley (1976) and Patankar *et al.* (1977)), surface pressure distribution (Andreopoulos (1982) and Kavsaoglu and Schetz (1989)), and visualization of surface streakline patterns (Krothapalli *et al.* (1990)) were followed.

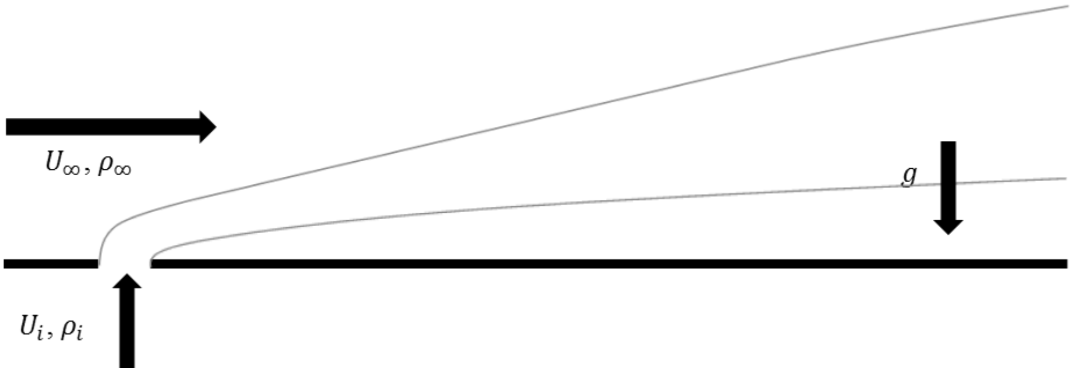

Figure 5.1 Schematic diagram of vertical jet injection against gravity direction into horizontal cross-flow

It has long been known that the jet deflects in direction of cross-flow and forms bent-over jet. Mainly, four structures can be discerned in the resulting flow. Figure 5.2 presents the structure; (1) the jet shear-layer vortices, (2) the system of horseshoe vortices, (3) the counter-rotating vortex pair, and (4) the wake vortices.

Jet shear-layer vortices dominate the initial portion of the jet. This is a result of the Kelvin-Helmholtz instability of the shear layer that separates from the jet orifice (Fric and Roshko (1994)). This is the same type of structures as the vortex ring of free jets (Freymuth (1966) and Gutmark and Ho (1983)).

Horseshoe vortices form from both the jet and the cylinder when cross-flow boundary layer encounters an adverse pressure gradient ahead of the obstacle. Krothapalli *et al.* (1995) studied horseshoe vortex upstream of a rectangular jet in cross-flow and found that the formation and roll up of the vortices can be periodic. Kelso and Smith (1995) found unsteady horseshoe vortex system with a round jet in cross-flow. Also, it is shown that the velocity ratio, $r\ (= U_i/U_\infty)$, is critical parameter that scales development of the vortices. Further observations of the horseshoe vortices were made by Andreopoulus (1982), Fric and Roshko (1994), and Shang *et al.* (1989).

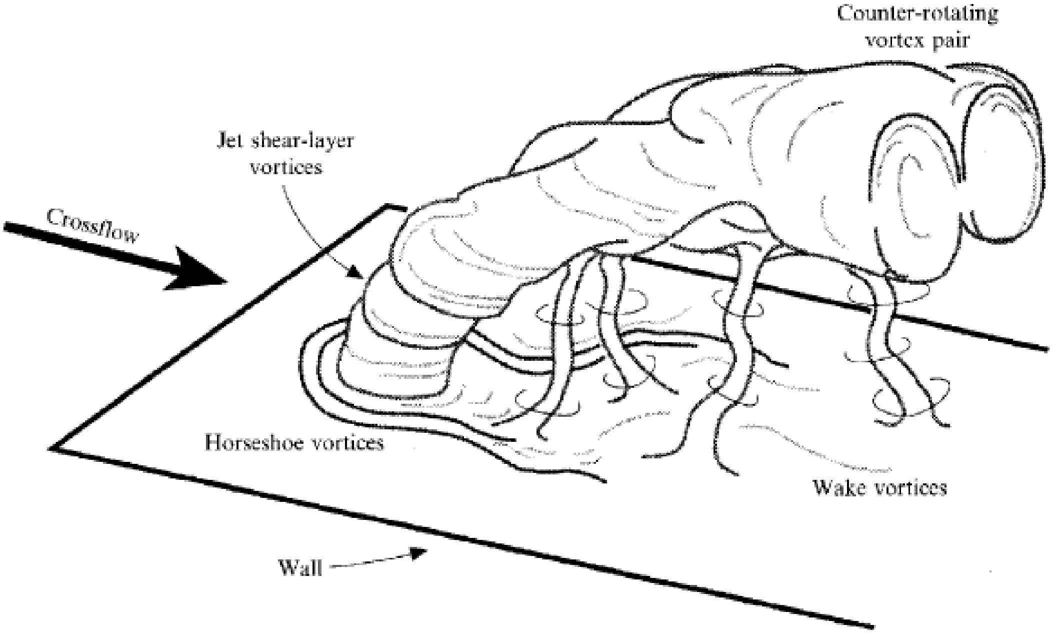

Figure 5.2 Cartoon depicting four types of vertical structure associated with the transvers jet near field: jet shear-layer vortices at the perimeter of the bending jet, the developing counter-rotating vortex pair, horseshoe vortices on the wall, and wake vortices

Counter-rotating vortex pair has been considered as signature feature of jets in crossflow. This vortex pair is highly unsteady and asymmetric. Kamotani and Greber (1972) examined how far an original jet persisted and observed vortex pair dominated the far field. Although numerous investigations were made, different mechanisms of counter-rotating vortex pair were suggested. Broadwell and Breidnthal (1984) explained this vortex pair occurred as a result of the impulse of a jet on a cross-flow. An alternative explanation considers the formation resulting from modification of a jet vorticity by cross-flow in a near field (Moussa *et al.* (1977), Andreopoulos and Rodi (1984), Skypes *et al.* (1986), and Coelho and Hunt (1989)). Kelso *et al.* (1996) suggested jet shear-layer tilts, folds and contributes to the circulation of the vortex pair. Muppidi and Mahesh (2006) offered an explanation based on pressure. When a circular region of out-of-plane flow interacts with in-plane cross-flow, this circular region evolves to counter-rotating vortex pair with the acceleration that the jet experiences in the direction of cross-flow.

Wake vortices are observed in downstream of the jet. These upright vortices extend from the wall to the leeward side of the jet. Though these vortices resemble a vortex street behind solid cylinder, Fric and Roshko (1994) showed those two wake vortices are noticeably different. They suggested the wake vortices are originated from separation events in the cross-flow boundary layer downstream of the jet. Kelso *et al.* (1996) suggested that vortices extend from the wall and incorporate into the wake vortex system where sign of vorticity agrees of horseshoe vortices and that of cross-flow boundary layer. Additional investigations were concerning entrainment, mixing, and stability of the jet in cross-flow for both incompressible and compressible regimes (Mahesh 2013).

5.1.2 Horizontal jet injection into vertical cross-flow along gravity direction

Investigation on horizontal gas jet injection into vertical liquid cross-flow parallel to the direction of gravity was made by Dawleh (1996). A schematic drawing of the jet and the cross-flow is presented Figure 5.3. He showed that the horizontally injected gas jet is strongly deflected by the vertical liquid flow. The structure of resulting flow was very different from a jet and counter flow of fluids with the same density that form a counter-rotating vortex pair. Its structure can be divided into three regions. The first region is gas pocket spread against the wall with turbulent gas-liquid interface. The second region is vortical structure with a strong mixture of two phases, which is also called recirculation region. At the third region, the jet loses its cohesion, breaks down into bubbly flow, and is carried away into the cross-flow. Figure 5.4 presents the structure with three regions.

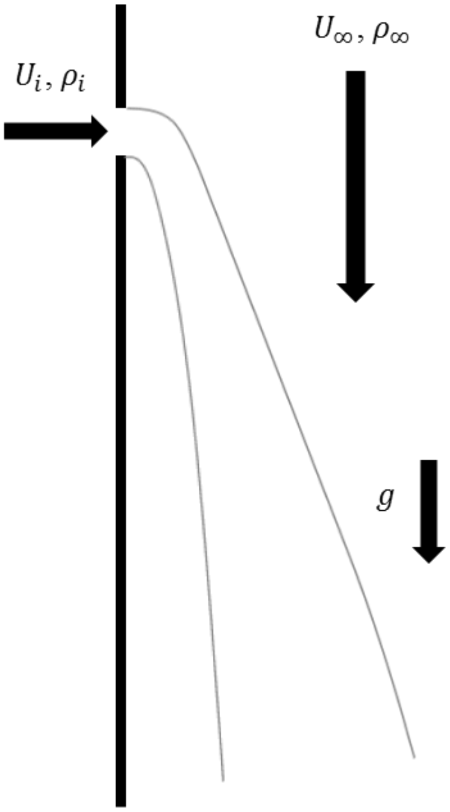

Figure 5.3 Schematic diagram of horizontal jet injection into vertical cross-flow along gravity direction

Noticeable difference between two flows is existence of counter-rotating vortex pair. It was impossible to measure velocity inside the gas pocket due to insufficient optical transparency for Dewlah (1996). Pignoux (1998) measured the void fraction in the gas pocket using phase detector, and showed very little phase mixing unlike the jet from above section. Also, it was noted that mean transverse velocity component was always oriented toward the exterior of pocket, which also indicated that mixing was insignificant. Moreover, the existence of a single large vortex with a transverse axis was inconsistent with the existence of counter-rotating vortex pair. Further investigation of Vigneau *et al.* (2001) showed boundary layer of the cross-flow had no influence on jet development in this case.

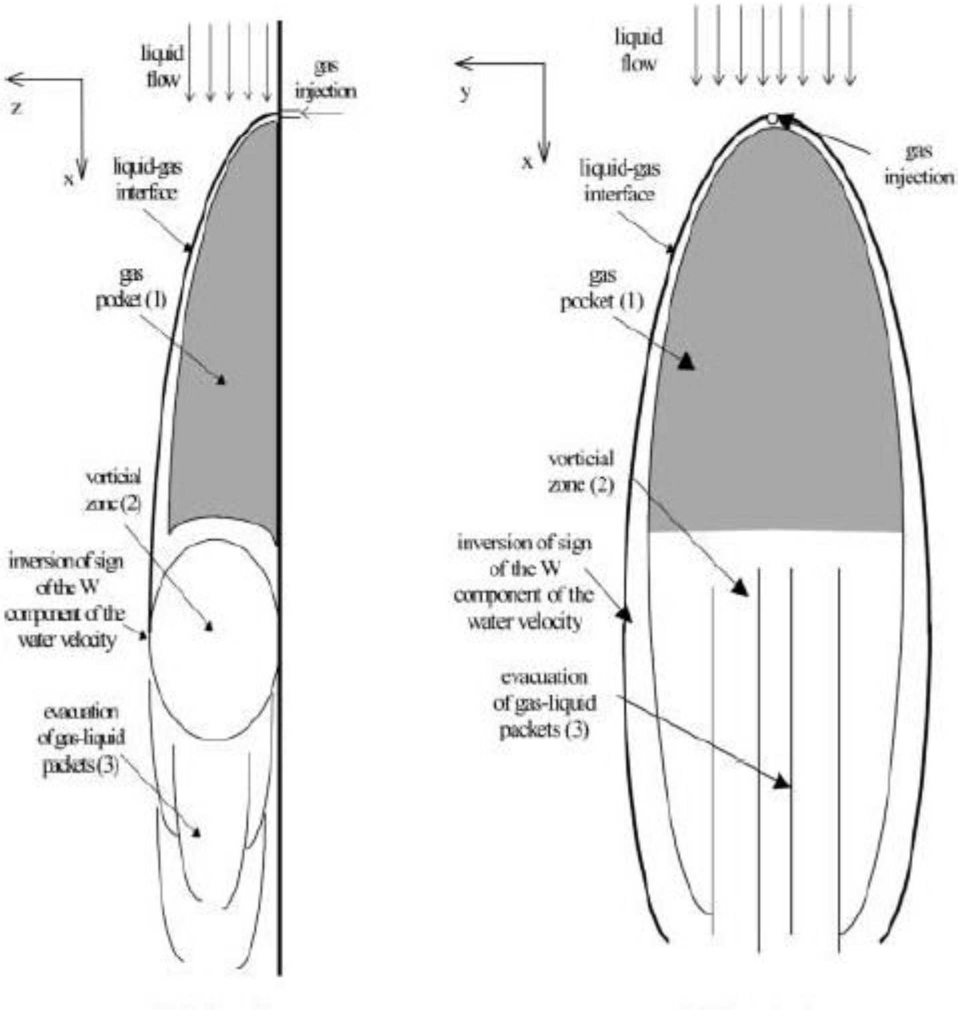

a) Side view b) Front view

Figure 5.4 Structure of a gas jet horizontally injected into a liquid vertical cross-flow (Vigneau et al. 2001)

Figure 5.5 presents image of physical experiment of gas jet injection horizontally into vertical cross-flow. Structures described above can be seen in the figure. Flow after the injection hole forms gas pocket, which is transparent, and flow breaks down to mixture of bubbly flow.

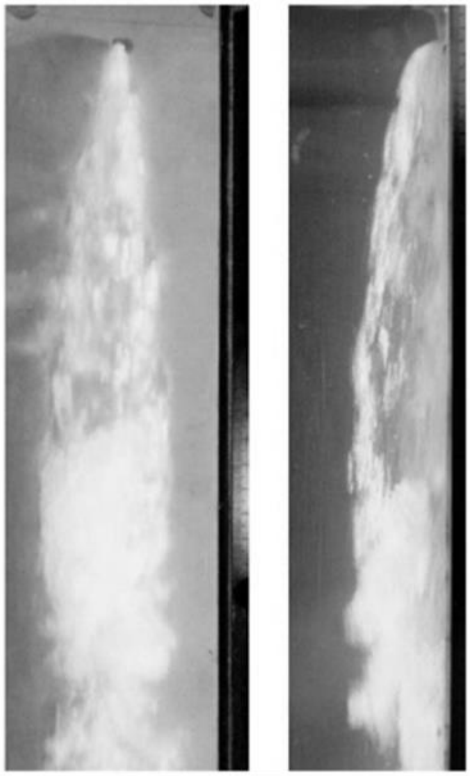

(a) (b)

Figure 5.5 Image of a gas jet horizontally injected into a liquid vertical cross-flow. U_∞=3.0$\mathrm{m/s}$, Q_i=2.67E-4m^3/s, D_i=1.0mm (Pignoux 1998)

5.1.3 Vertical jet injection along gravity direction into horizontal cross-flow

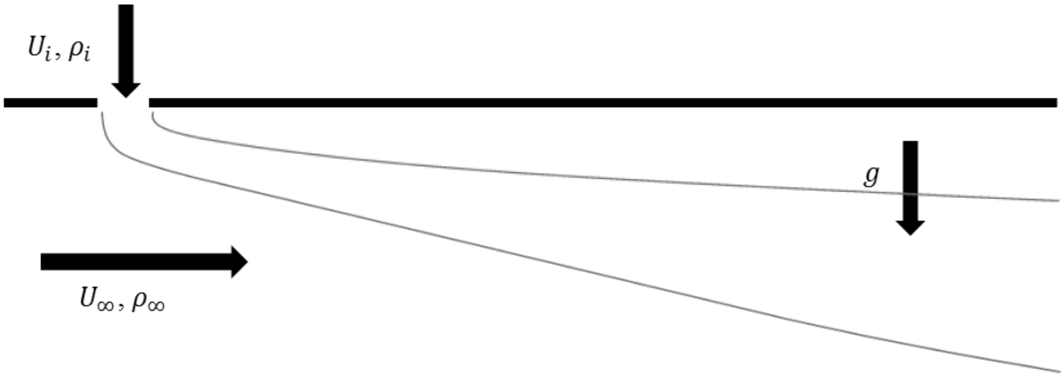

Figure 5.6 Schematic diagram of vertical jet injection along gravity direction into horizontal cross-flow

Schematic drawing of the jet injected vertically along gravity direction into horizontal cross-flow is presented Figure 5.6. Few investigators have reported on this case. Menoret and Bonazzi (1985) and Morton and Ibbetson (1996) showed vertically injected jet splits into two distinct regions generated, they believed, by the growth of counter-rotating vortex pair. Figure 5.7 presents the structure with two split regions. Insel (2010) performed physical experiment of air injection through circular orifice beneath ship hull. The study showed that the flow splits into two regions, described as "V" shape. Spreading angles between two regions were measured and analyzed with different cross-flow speeds and air injection rates. Figure 5.8 shows an image of physical experiment of gas jet injection through circular hole on the bottom hull into cross-flow (Insel 2010).

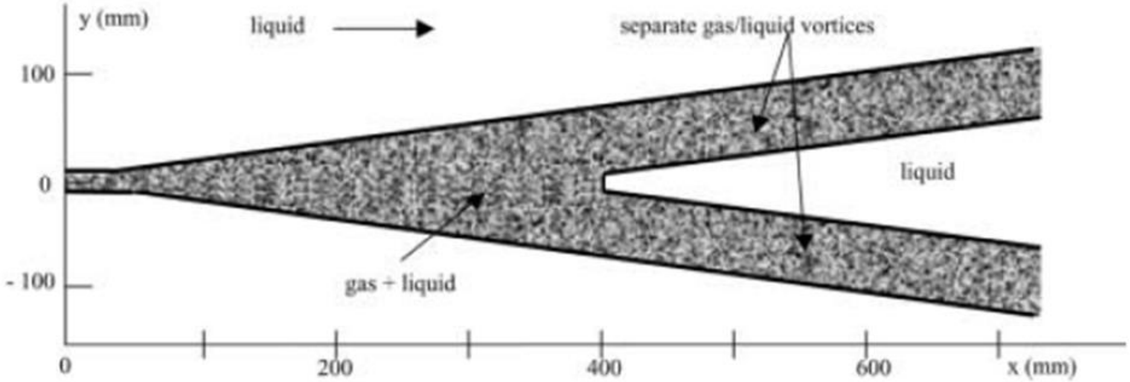

Figure 5.7 Diagram of a vertical jet injected along gravity direction into horizontal liquid cross-flow: Π=1, Re_{D_i}=2.5E+4 (Originally Menoret and Bonazzi 1985, Extracted from Pignoux 1998)

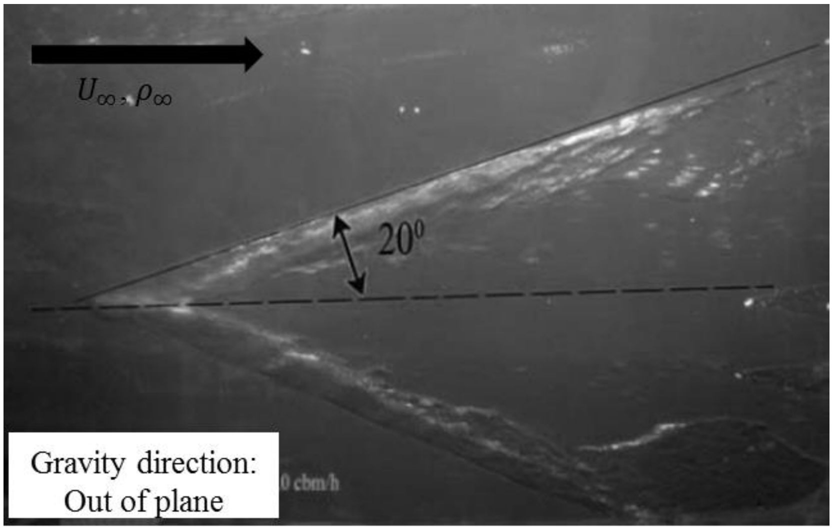

Figure 5.8 Image of vertical air jet injected which splits into two legs along gravity into horizontal liquid cross-flow. Fr=0.158 and Q_i=1.0m^3/h. (Insel 2010)

5.2 Present study

In the present study, a vertical gas jet is injection along the gravity direction into a horizontal cross-flow, and its topology is visualizing the flow using high and low speed cinematography. In the study of Morton and Ibbetson (1996) and Insel (2010), cross-flow condition was laminar flow and range of jet injection rate was relatively low. Hence, turbulent cross-flow condition and higher range of jet injection are applied in the present study. The topology of the jet is examined for a range of flow conditions. Then, a scaling is proposed using a range of independent parameters.

5.3 Roadmap

Second part of the thesis will be mapped in the following order. Experimental setup is introduced in Chapter 6. Properties and description of facilities, barge models, measuring instruments, and imaging system are presented. Chapter 7 lays out results from the experiment; general topologies of vertical jet into cross-flow, sweep angle (φ), chord length of the leg (C), and equivalent diameter of the air jet (D_E). Scaling of vertical jet injection along gravity direction into cross-flow beneath horizontal surface is presented in Chapter 8. Chapter 9 discusses the physical explanation of the study, concludes the chapter, and presents future work.

CHAPTER 6

Experimental Setup

6.1 Overall setup and parameters

The experiments were performed in the Physical modeling basin in Marine Hydrodynamic Laboratory, University of Michigan. The Basin has $109.7m$ running room with $6.7m$ width and $3.2m$ depth. A manned bridge and unmanned trailer type carriage can transport instruments and model along the basin. The carriage has speed range from $0.08m/s$ to $6.10m/s$. A beach on one end of the basin and a wavemaker on the other end can make or reduce surface waves. During testing, a 15-minute to 30-minute break was taken between every experimental run to ensure calm water condition. The water level was adjusted every day before the experiments were performed since the water level varies due to evaporation. An image of the basin is presented in Figure 6.1.

Two barge models with circular hole on the bottom were used to realize horizontal surface with inflow. Tubes connected to gas injection system were inserted in the bottom hole to realize vertical gas injection. The air flow rate (Q_i) and cross-flow speed (U_∞) were controlled by the gas injection system and the carriage system, respectively. The overall setup with critical parameters is shown in Figure 6.2. Optical measurements were taken around the gas injection location using various imaging system from the side and the bottom of the models. Detail descriptions of the setup are presented in the following subsections.

Figure 6.1 Photograph of the physical modeling basin in Marine Hydrodynamic Laboratory, University of Michigan

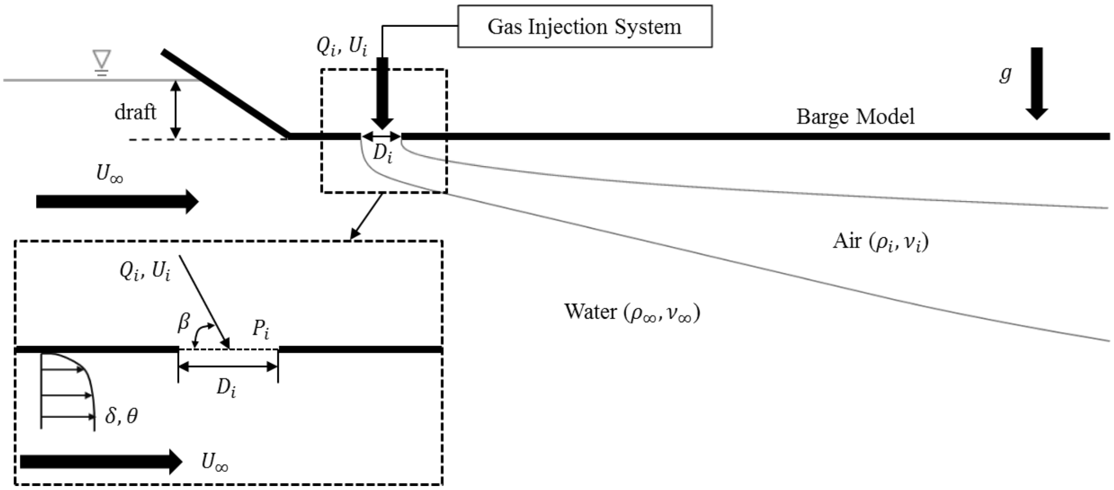

Figure 6.2 Diagram of overall experimental setup with critical parameters

6.2 Barge models

Two different barge models, Barge model I and Barge model II, were used which have different boundary layer thickness at the location of gas injection. Both models had transparent bottom to observe behavior of injected air underneath the surface. The models were fixed with struts on the carriage to prevent any motion relative to the carriage. Struts were vertically attached on each bulkhead, bow/body and body/stern. Two horizontal struts were fixed on the carriage catwalk. Care was taken to ensure that models were well-leveled all time during experiments with fixed draft of 0.076m.

6.2.1 Barge model I

Barge model I is a modified model of *Olympic Spirit*. It has overall dimension of 4.30m length, 0.73m width, and 0.34m height (81.28mm draft). Dimensions and arrangements of Barge model I are specified in Figure 6.3 The bow part is modified from original in order to have less air ingestion with lower slope, 8°, and uniform 2-D inflow spanwise. 150μm size particles were uniformly fixed across the span of the model 1.0 m from the nose of the model on a strip 0.1m wide to induce turbulent boundary layer profile. Boundary layer profile measurement device and air injection hole are located at the center transversely and 0.4m after 8° slope longitudinally in order to have enough room for flow development.

6.2.2 Barge model II

Barge model II has overall dimension of 5.84m length, 1.52m width, and 0.27m height (81.28mm draft). Dimensions and arrangements of Barge model II are specified in Figure 6.4. The bow part has half-ellipse shape flat bottom to reduce air ingestion and sharp angle structure, ~40°, on the flat plate to break wave. A schematic drawing of the bow part is presented in Figure 6.5. Extra struts were attached on the bow part to reinforce structural support. Likewise Barge model I, 150μm size particles were uniformly tripped spanwise with 0.2m length to induce turbulent boundary layer profile. A 0.28m long and 1.42m wide slot is located at the beginning of the body part, and this slot was used to mount a plate with a fixture for the boundary layer profile measurement device and injection holes. Inserting plates are presented in Figure 6.6. Three injection holes enabled to test multiple gas injection. Boundary layer profile measurement device and middle injection hole are at the same location, center transversely and 0.7m after boundary layer trip longitudinally in order to provide enough room for flow development of the turbulent boundary layer.

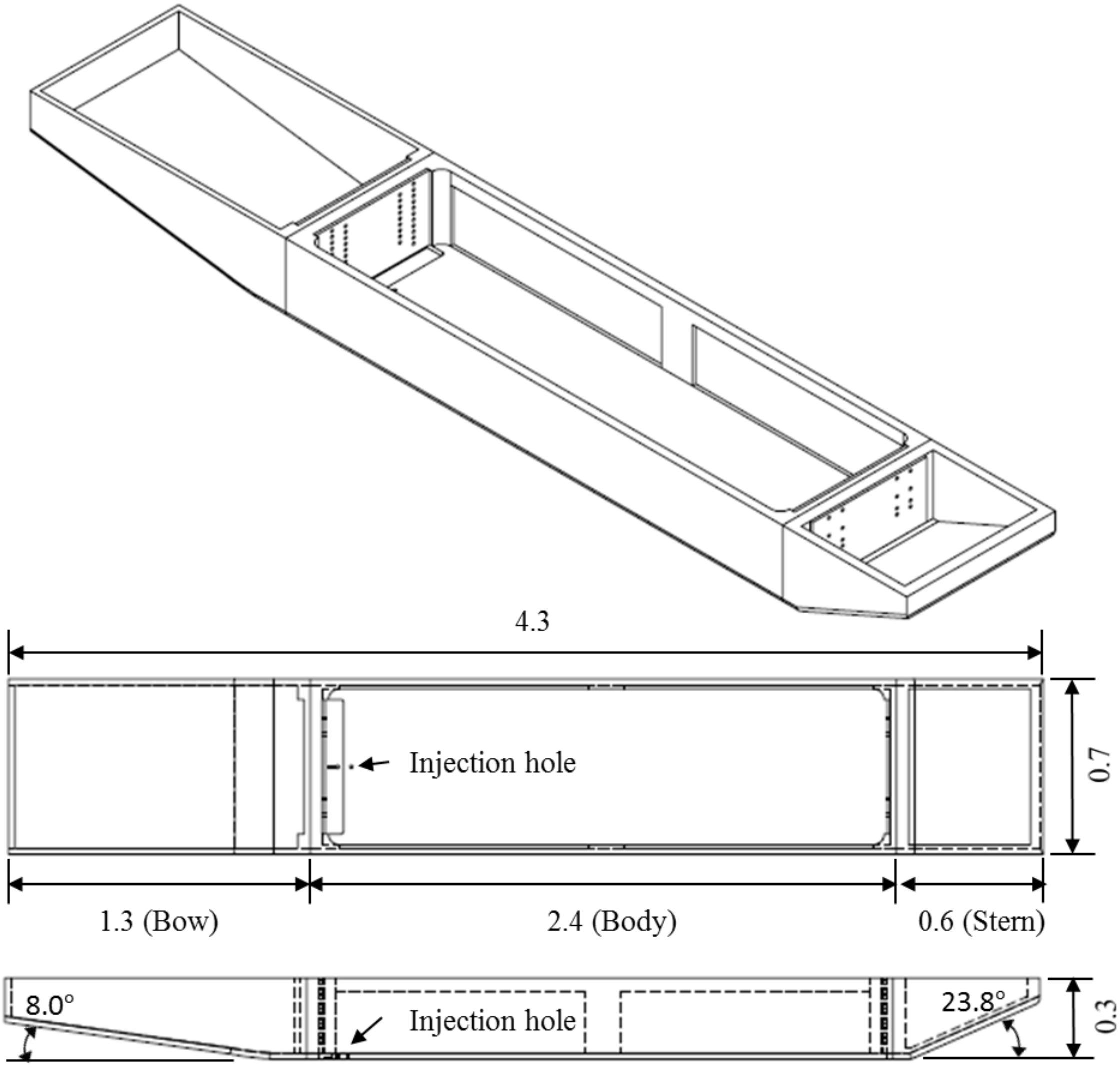

Figure 6.3 Dimensions and arrangements of Barge model I. All dimensions are in meters.

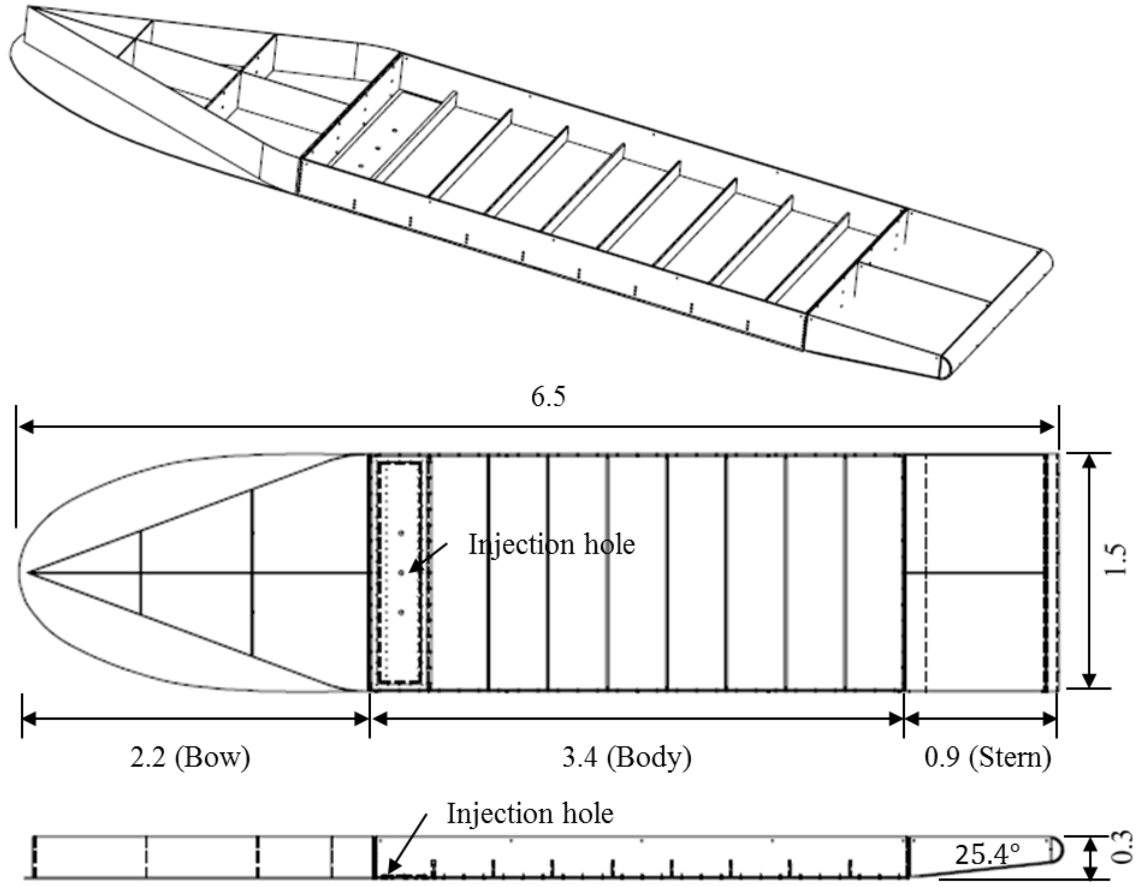

Figure 6.4 Dimensions and arrangements of Barge model II. All dimensions are in meters.

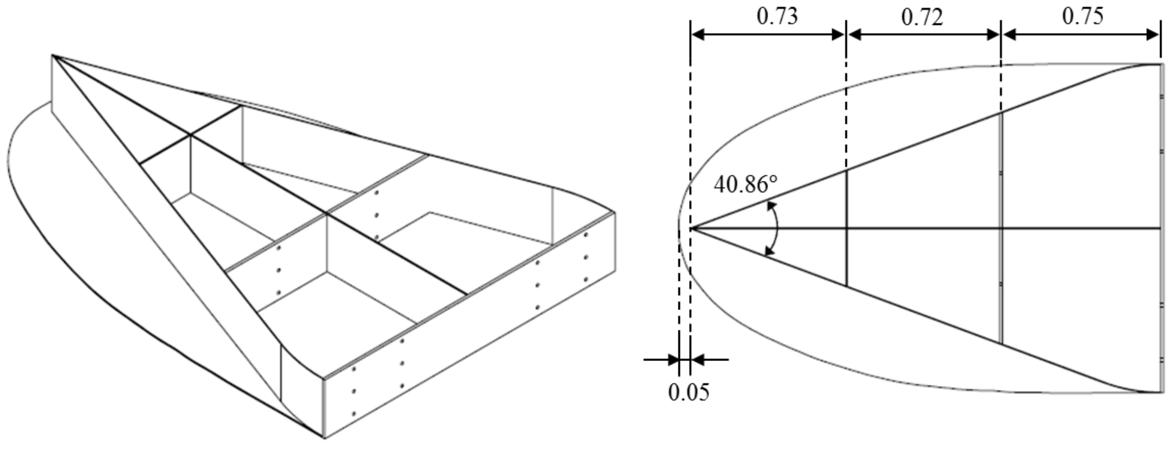

Figure 6.5 Dimensions of bow part of the Barge model II. All dimensions are in meters.

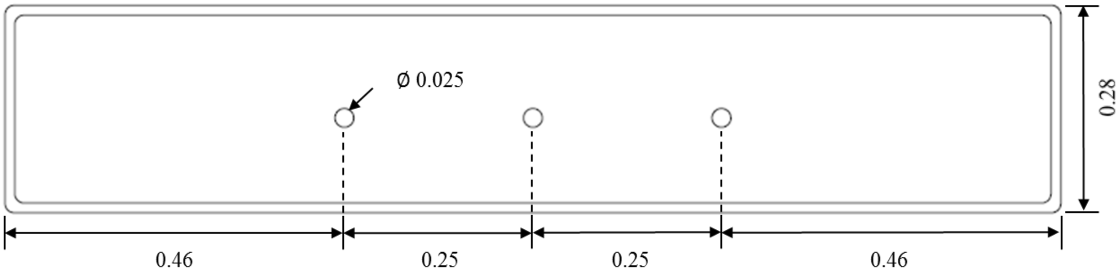

Figure 6.6 Dimensions of inserting plate with injection holes. All dimensions are in meters.

6.3 Instruments

This section presents instruments that control and measure air injection rate (Q_i), injection hole size (D_i), injection angle (β), pressure at the injection hole (P_i), boundary layer thickness (δ), and so on.

6.3.1 Gas injection system

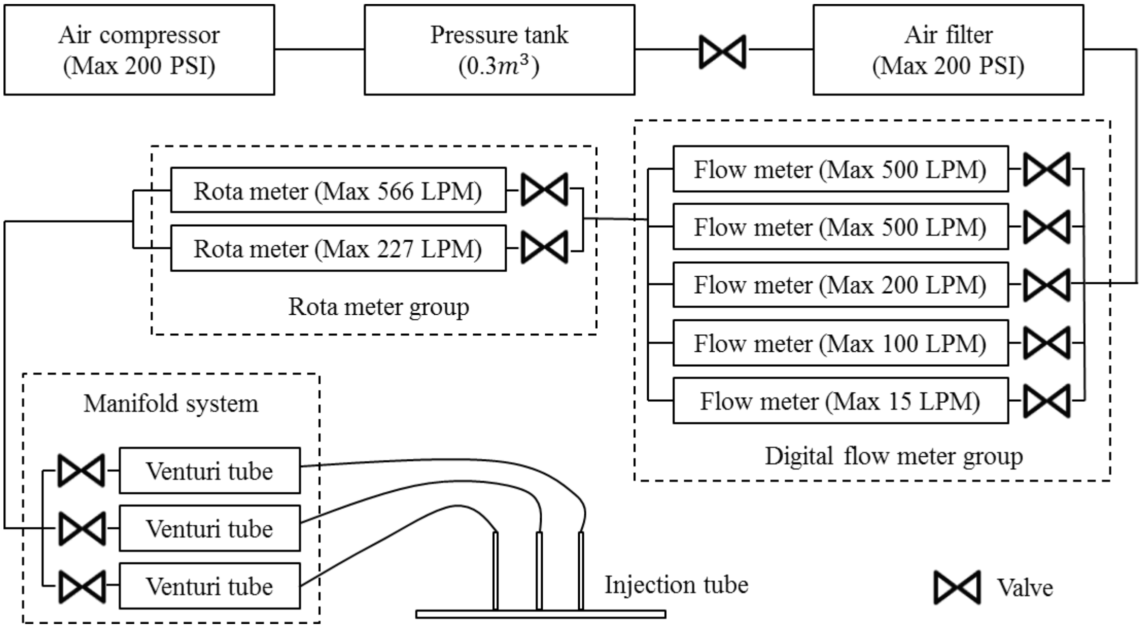

Figure 6.7 Block diagram of gas injection system

The gas injection system was designed to generate, regulate, and measure stable air flow rate beneath the barge model on moving carriage system. Figure 6.7 shows the block diagram of the gas injection system. An air compressor (Dewalt) with a power of 1.6 HP continuous, and a pressure of 1400 kPa was used to compress air into $0.30\ m^3$ capacity ASME-Code pressure tank. Air flows from the pressure tank to flow meters through pressure regulator and air filter.

Flow meters were composed of two groups in series; a group of digital flow meters (Omega FMA 5400/5500 series) for measurement/flow control and another group of rotameters for confirmation of the flow rate. The first group was consisted of five digital flow meters with different capacities, two-8.3E-3m^3/s(Omega FMA5544), 3.3E-3m^3/s(Omega FMA5543), 1.7E-3m^3/s (Omega FMA5542), and 2.5E-4m^3/s(Omega FMA5532). Digital flow meters were connected in parallel with valves so that one or two chosen flow meters were used in combinations as needed. Accuracy of the digital flow meters is $\pm 3\%$ of full scale. The second group of meters consisted of six rotameters with different capacities, and two of them were used in this experiment. Either rotameter (Omega FL2003) with capacity 3.8E-3m^3/s or rotameter (Omega FL2001) with capacity 9.4E-3m^3/s were used according to the air flow rate condition and their accuracies are each $\pm$1.1E-4m^3/s and $\pm$1.9E-4m^3/s.

A manifold system could be used to split the flow equivalently for multiple injection experiment. Through this system, main flow from flow meters could be divided into three flows. Valves and Venturi tubes were installed to control and measure flows. Venturi tubes were design to measure the flow speed using the Venturi effect. When there is constricted tube and pressures at each cross section are identified, flow speed can be calculated with Bernoulli's equation assuming incompressible flow:

$$\frac{{U_1}^2}{2} + \frac{P_1}{\rho_i} = \frac{{U_2}^2}{2} + \frac{P_2}{\rho_i} \tag{6.1}$$

U_1, U_2, P_1 and P_2 are flow speed and pressure at location 1 and 2. Design of Venturi tube is presented in Figure 6.8. Diameters of the tube, D_1 and D_2, were decided considering range of the flow rate. From continuity, U_2 can be substituted by U_1 and cross section area ratio:

$$\Delta P = P_1 - P_2 = \frac{1}{2}\rho_i {U_1}^2 \left[\left(\frac{{D_1}^2}{{D_2}^2} - 1\right)\right] \tag{6.2}$$

Solving U_1 and multiplying by cross section area gives the volumetric flow rate Q. A discharge coefficient, $C_{DC} = 0.98$, is introduced here to consider the viscosity of actual fluid (Fluid Flow 4th edition, Sabersky, R. H.).

$$Q = C_{DC}\sqrt{\frac{2\Delta P}{\rho_i}}\,\frac{\frac{\pi}{4}{D_1}^2}{\sqrt{\frac{{D_1}^2}{{D_2}^2} - 1}} \tag{6.3}$$

Pressures were measured at two locations specified in Figure 6.8 using differential pressure transducer (Omega PX138-001D5V).

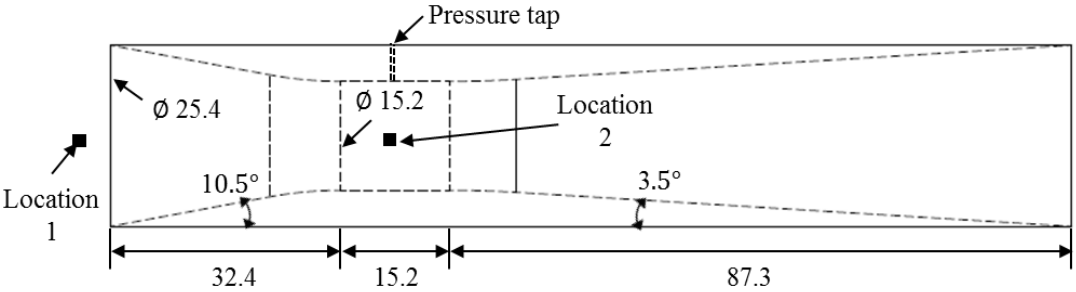

Figure 6.8 Dimensions of venture tube. All dimensions are in millimeters.

6.3.2 Injection tubes

The injection tube was inserted in the hole located at the center transversely of the Barge model. Shaft collars were fixed on the injection tube so that bottom surface of the

Barge model was flush with the tube end. Tubes were fabricated with fixed outer diameter, 19.1mm for Barge model I and 25.4mm for Barge model II, and various inner diameter, $D_i = 5.0$mm ~ 20.0mm. 3D-printing was used to fabricate injection tubes with angle using resin material. Tubes with angles have straight lead-up section with at least $20\ D_i$ length before the angled exit passage to ensure that a nearly developed flow occurs in hole with D_i. The injection angle, β, is defined as the angle between the bottom surface of the barge and the upstream direction, and the injection angle varied from $22.5°$ to $157.5°$. The outlet pressure was measured *via* a pressure tap with 1.59mm diameter located at 50.0mm or 75.4mm from the top of the tube using pressure transducer (Omega PX309-050AV). Figure 6.9 presents dimensions of injection tubes.

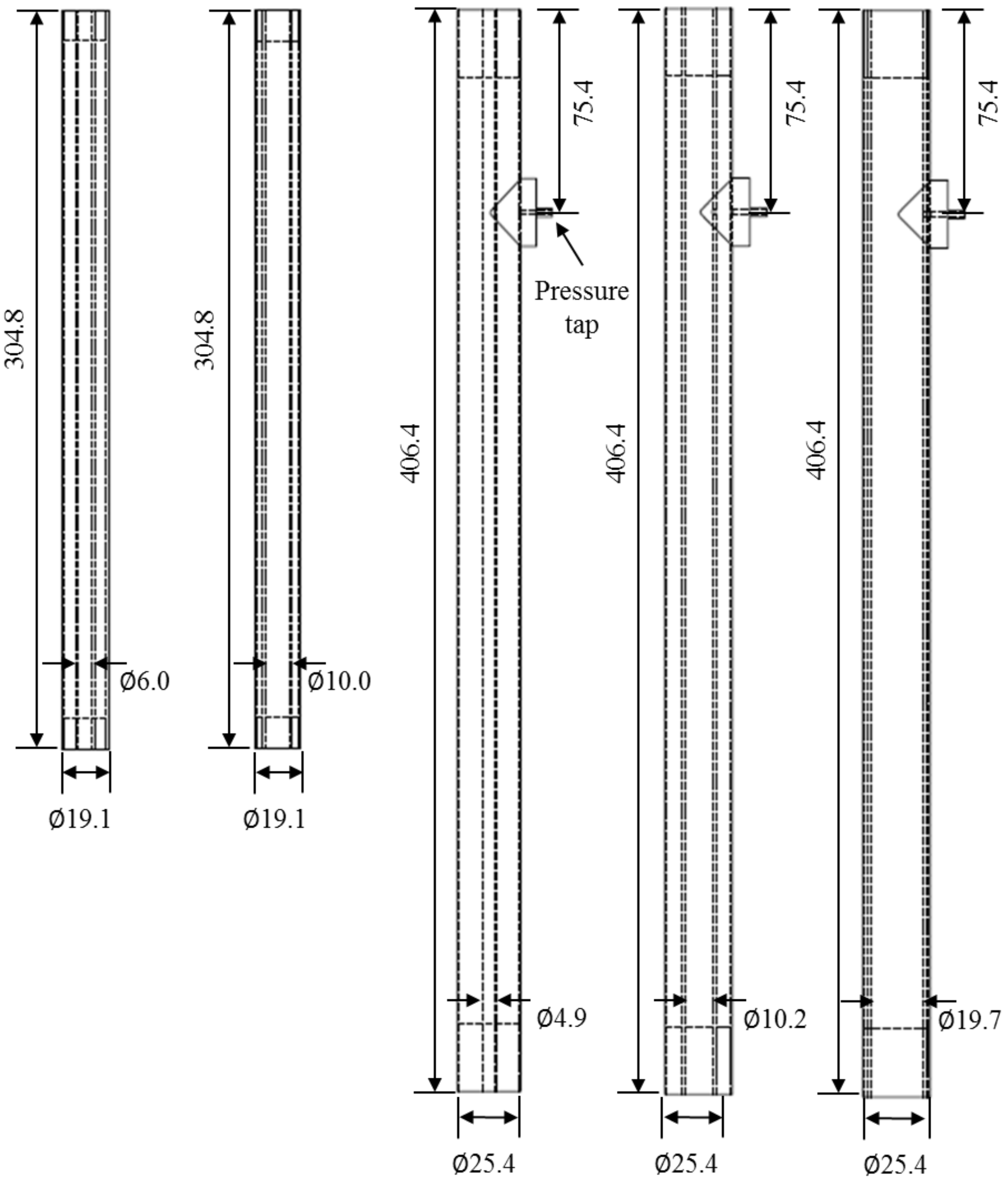
304.8
Ø6.0
Ø19.1
304.8
Ø10.0
Ø19.1
406.4
75.4
Pressure tap
Ø4.9
Ø25.4
406.4
75.4
Ø10.2
Ø25.4
406.4
75.4
Ø19.7
Ø25.4

(a)

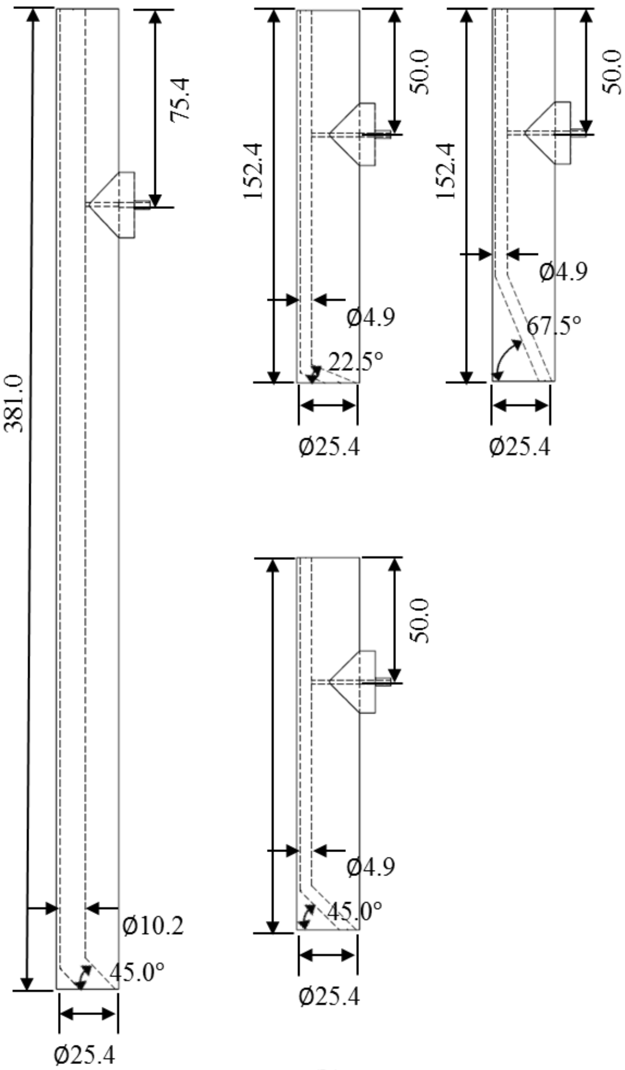

(b)

Figure 6.9 Dimensions of injection tubes. All dimensions are in millimeter. (a) Straight injection tubes (β=90°).Two injection tubes on the left are used with Barge model I and the other three tubes are used with Barge model II (b) Injections tube with angle. All tubes are used with Barge model II.

The pressure drop between the outlet and pressure tap was measured with same flow rate conditions with ambient pressure (but without water or flow present at the exit). Then pressure at the injection outlet was calculated by subtracting measured pressure drop in ambient condition from pressure measured at specified draft and flow.

6.3.3 Boundary layer profile measurement

The boundary layer profile for each barge model and flow speed was measured at the location of the air injection hole. A pitot tube (Omega PBE-H-M) was used to measure the conditions across the boundary layer profiles at each free stream speed. The pitot was fixed on a stage that was translated in vertical direction with 2.54 mm increments. The range of the stage translation was from 0 mm, on the bottom of the Barge model surface, to 12 mm. By changing the height of the stage at fixed free stream speed, the stagnation pressure at each height was measured by pressure transducer (Omega PX409-2.5DWU5V) which was connected to the pitot. Velocity profiles were obtained using Bernoulli's equation. Boundary layer profiles of each barge models are presented in Figure 6.10. δ_1 and δ_2 represents boundary layer thickness of Barge model I and II.. Their ranges were δ_1= 15.8 ~ 19.1 mm and δ_2= 50.7 ~ 57.4 mm.

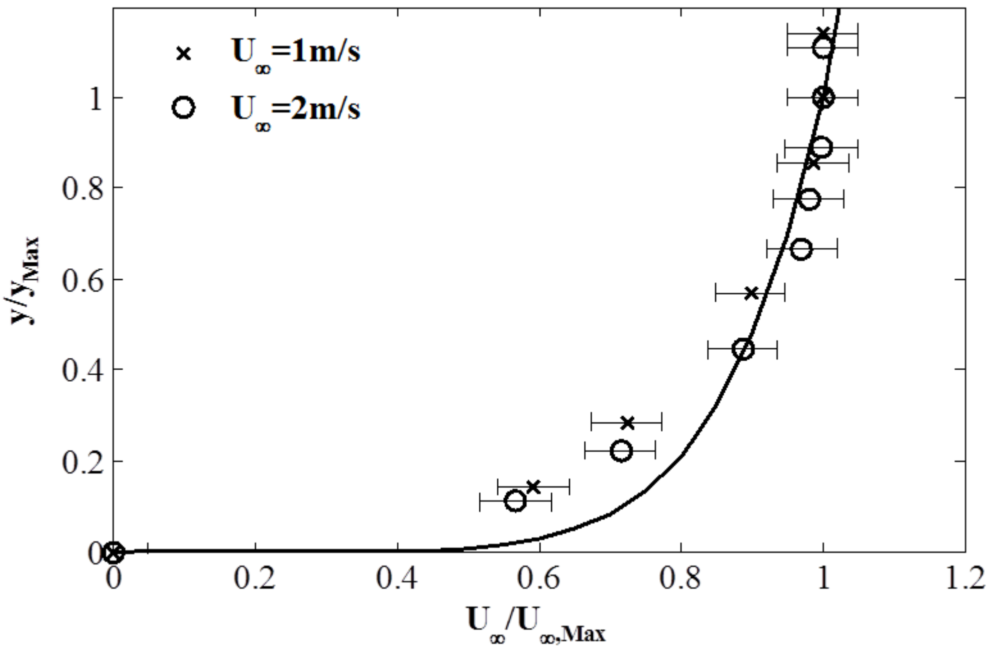

(a)

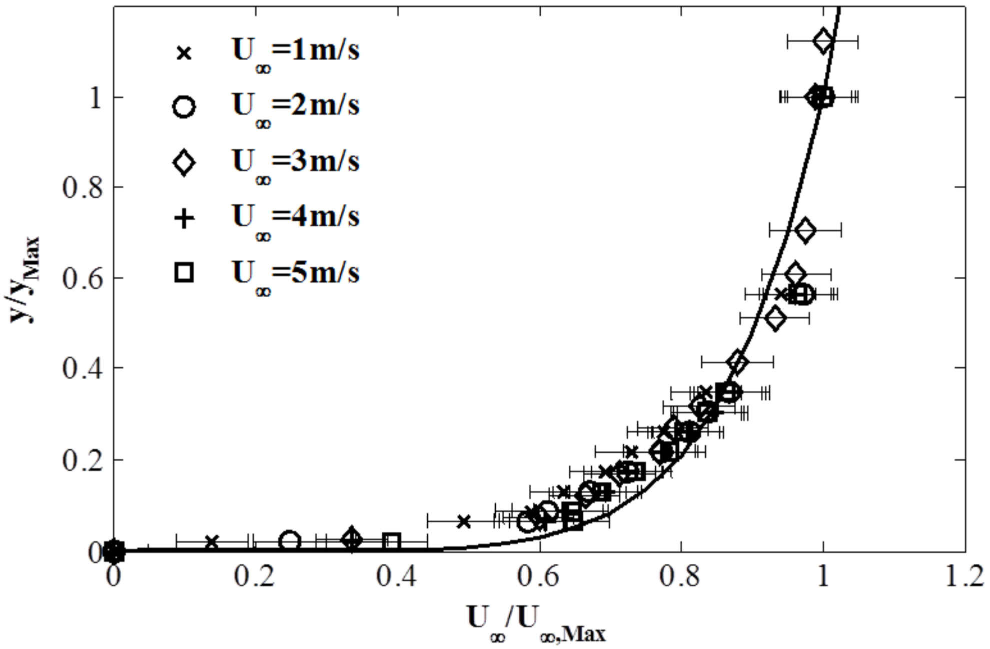

(b)

Figure 6.10 Boundary layer profiles of each Barge model. (a) δ_1 (Barge model I) and (b) δ_2 (Barge model II). Solid line is profile of 1/7th law. y_{Max} is about 18mm for δ_1 and about 53mm for δ_2 on average. $U_{\infty,Max}$ varies from 1~5m/s.

6.4 Imaging system

Two different imaging systems were used to observe the topology of the gas flow, the process of injected air development, from the side and from the bottom of the Barge model. Detail setup of each cinematography and illumination is described in the following sub sections.

6.4.1 Low Speed Cinematography

The low speed cinematography system was fixed on the carriage to view the side of the target. A GoPro Black edition camera was used as the low speed cinematography system, and this camera was fixed on the catwalk of the carriage. The camera was placed about $0.6\,m$ beneath the free surface. Videos were taken with 1280×960 pixel resolution and 30 fps sampling rate.

6.4.2 High Speed Cinematography

The high speed cinematography system was stationary and placed at the bottom of the basin, $3m$ from the free surface, focusing on the bottom surface of the Barge model. A Phantom V710 camera was enclosed in a water proof container. The camera was placed at the mid-tank, $49.2\,m$ from the starting point of the carriage. Location of the camera with carriage speed curves is presented in Figure 6.11. The acceleration of the carriage was $0.20\text{m}/s^2$ and $0.40\text{m}/s^2$ at $1\text{m}/\text{s}$ and $2\text{m}/\text{s}$. And $0.52\text{m}/s^2$ of acceleration was used for higher speed ($3\text{m}/\text{s}$, $4\text{m}/\text{s}$, and $5\text{m}/\text{s}$). Videos were taken with 1440×1080 pixel resolution at 200 fps sampling rate, with $5\,ms$ of exposure time, and 5 sec of acquisition time. Recording was manually triggered to start recording as the barge approaches the camera and stopped at 5 sec of recording time.

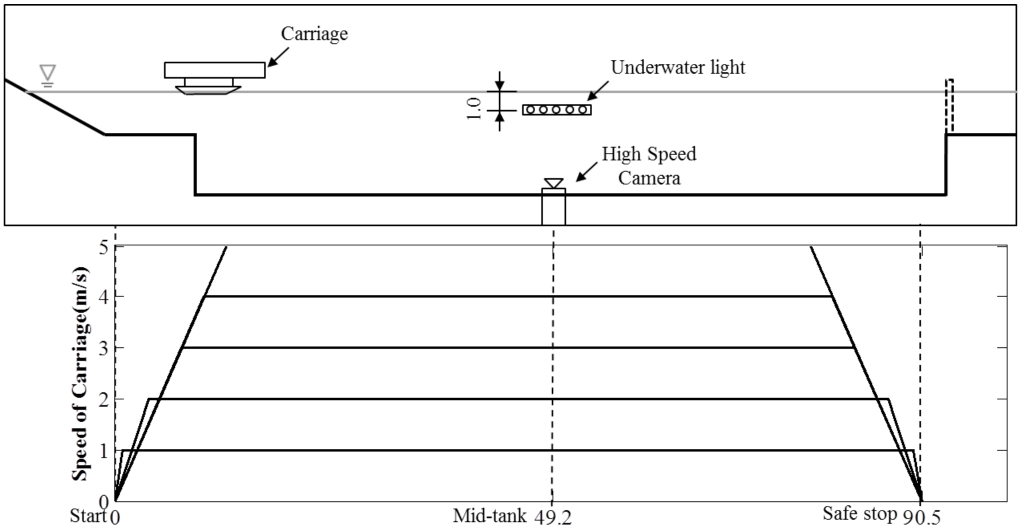

Figure 6.11 Location of High speed camera and underwater LED lamps. All dimensions are in meter. Bottom plot is the carriage speed profile (U_∞=1,2,3,4,and 5 m/s)

Ten 100W high power LED light lamps were used to illuminate the target. Water-proof containers on each side of the basin holding five of LED light lamps were mounted on each side wall of the mid-tank at about $0.9\ m$ deep from the free surface directing toward the carriage. The average intensity of each LED light lamp is $8000{\sim}9000\ lm$. The locations of the lights are shown in Figure 6.11.

6.5 Test matrix

Table 6.1 summarizes test matrix of dimensional parameters.

Parameter	**Range**	**Note**
$\boldsymbol{U_\infty}$ (m/s)	**1.0 ~ 5.0 ±0.4%**	**Cross-flow speed = Carriage speed**
$\boldsymbol{\delta}$ (mm)	$\boldsymbol{\delta_1}$ **= 15.8, 19.1 ±1.0** $\boldsymbol{\delta_2}$ **= 50.7~57.4 ±2.8**	$\boldsymbol{\delta_1}$ **and** $\boldsymbol{\delta_2}$ **are boundary layer thickness of each Barge model I and Barge model II**
$\boldsymbol{D_i}$ (mm)	**Nominal inner diameters are 5.0, 10.0, and 20.0.** **Actual diameters are** **Barge model I : 6.0 and 10.0** **Barge model II : 4.9, 10.2, 19.7**	
$\boldsymbol{\beta}$ (°)	$\boldsymbol{D_i}$**=5.0;** $\boldsymbol{\beta}$**= 22.5, 45.0, 67.5, 90, 112.5, 135.0, and 157.5** $\boldsymbol{D_i}$**=10.0;** $\boldsymbol{\beta}$**= 45.0, 90, and 135.0** $\boldsymbol{D_i}$**=20.0; β= 90**	
$\boldsymbol{Q_i}$ $(\boldsymbol{m^3/s})$	**1.01E-04 ~ 1.16E-02 ±2.0E-4**	**Volume flow rate at atmospheric pressure**
$\boldsymbol{P_\infty}$ $(\boldsymbol{kPa})$	**102.07 ±0.04**	**Hydrostatic pressure with fixed draft with atmospheric pressure**

Table 6.1 Test matrix of dimensional parameters of vertical jet into cross-flow beneath horizontal surface experiment

CHAPTER 7

Results

7.1 Topology of deflected jet

When the gas jet discharges from the injection hole into the cross-flow, the diameter of the jet increases, and the gas forms a single pocket near the injector. The gas jet is deflected by the oncoming liquid flow, but it often undergoes a “puffing” behavior where the volume flux appears to vary around a mean level with some fixed frequency. Farther downstream from the injection location, the gas pocket reaches a maximum depth and then begins to close on the model surface. As the gas pocket closes, it cleaves into two distinct pockets of gas (“legs”). In some cases, the vast majority of the gas is directed into the legs, while in others some gas fills in between the legs. As the flow develops along the surface, the gas legs were stable until they either impinges on the boundary of the barge model or broke down after loss of gas as a result of entrainment in the leg cavity closure. Figure 7.1 presents schematic drawing of resulting flow.

Measurements of the topology of the jet were taken from image of high speed cinematography. Three major measurements were taken for all conditions, sweep angle of the legs (φ), chord length of the leg (C), and equivalent diameter of the jet (D_E). Two of the first measurements represent the far-field flow and equivalent diameter of the jet represents the near-field flow. Sweep angle of the leg (φ) was measured from the plane perpendicular to the cross-flow direction to the edge of the leg. Average thickness of the leg is defined to be chord length of the leg(C). Equivalent diameter of the jet (D_E) was measured at the close view of injection hole. As the diameter of the jet fluctuates, the thickest moment was captured and equivalent diameter was measured.

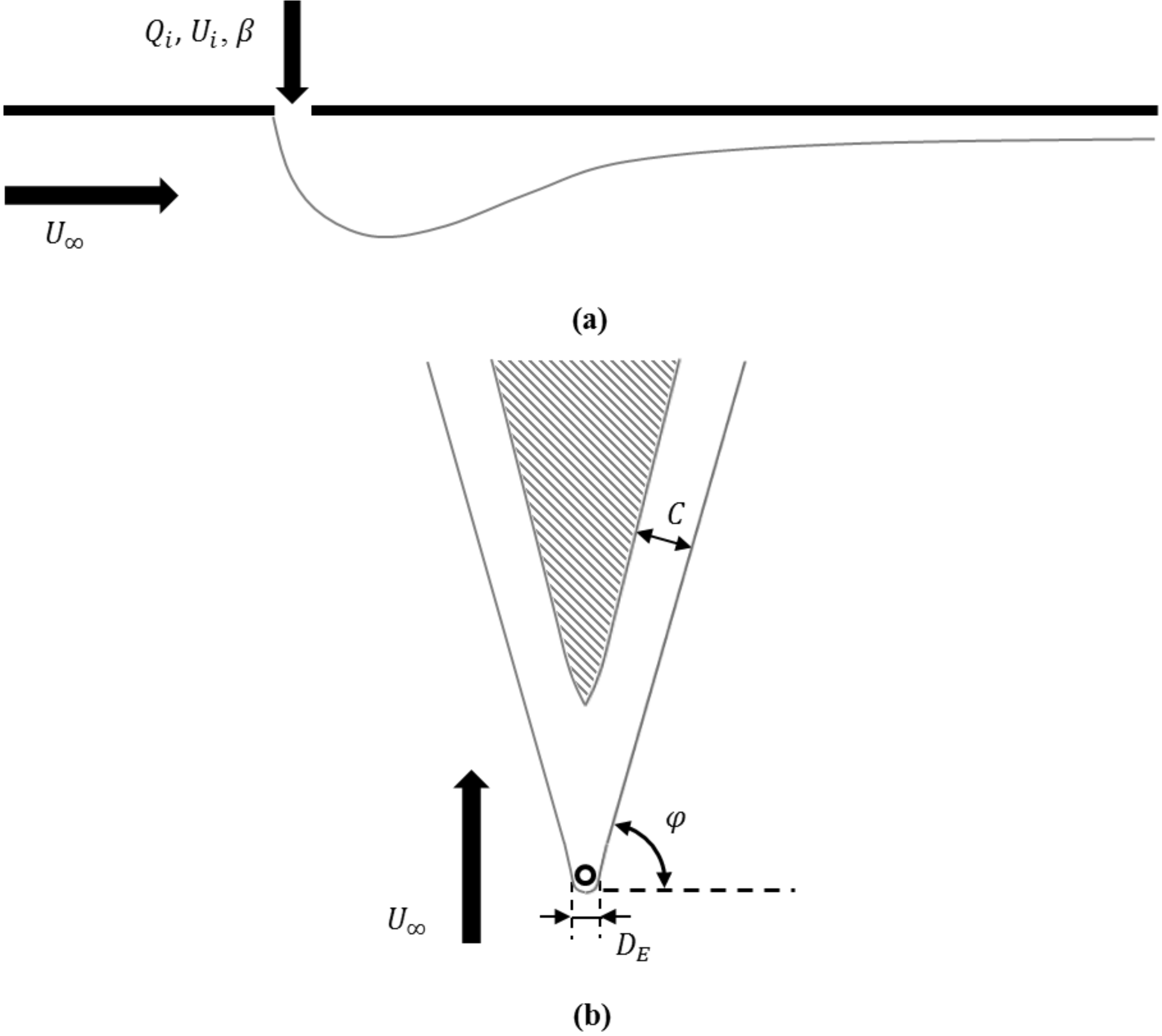

Figure 7.1 Schematic drawing of resulting flow topology is presented with parameters, sweep angle φ, average chord length of the leg C, and equivalent diameter of the jet D_E. Each drawing is (a) side view and (b) bottom view of the deflected jet. Delta type(Δ) has gas filled in between legs(area with diagonal pattern) and Lambda type(Λ) has no gas in it.

From input variables and measurements, the non-dimensional parameters that take dominant role in the physics are listed in Table 7.1. ρ_i and ρ_∞ are density of the jet and the cross-flow. They are both assumed to be constant value throughout the experiment; ρ_i=1.205kg/m^3 and ρ_∞=1000 kg/m^3.

Parameter	**Range**	**Note**
Fr_δ	**1.33~7.10 ±0.2**	$Fr_\delta = \frac{U_\infty}{\sqrt{g\delta}}$
$\frac{Q_i}{U_\infty \delta^2}$	**6.74E-2 ~ 1.34E+1 ±0.2**	**Ratio of jet volume flow rate and displaced volume flow rate of cross-flow in the boundary layer**
$\frac{D_i}{\delta}$	**0.08 ~ 0.63 ±0.03**	**Ratio of injection hole and boundary layer thickness**
$\frac{U_i sin\beta}{U_\infty}$	**0.94 ~ 163.12 ±1.0**	**Ratio of vertical component of jet speed and cross-flow speed**
$\frac{U_i cos\beta}{U_\infty}$	**-75.34 ~ 159.66 ±1.0**	**Ratio of horizontal component of jet speed and cross-flow speed**
$\frac{\rho_i}{\rho_\infty}$	**1.21E-3**	**Ratio of density** ρ_i**=1.205kg/**m^3**,** ρ_∞**=1000kg/**m^3
Π	**1.07E-3 ~ 6.14E+1**	$\Pi = \frac{\rho_i {U_i}^2}{\rho_\infty {U_\infty}^2}$
Re_{D_i}	**3.69E+3~9.57E+4**	$Re_{D_i} = \frac{U_i D_i}{\nu_i}$
We	**5.86E-5~4.54E-3**	$We = \frac{S}{\rho {U_\infty}^2 \delta}, S = 0.072N/m$
Ma	**1.91E-3~1.56E-1**	$Ma = \frac{U_i}{c}, c = 1481\ m/s$

Table 7.1 Test matrix of non-dimensional parameters of vertical jet into cross-flow beneath horizontal surface experiment

Topologies of the resulting flow can be classified into three different types, “Delta” type (Δ), “Lambda” type (Λ), and transition type. Three types are distinguished by existence of air in between legs. Delta type topologies (Δ) have a bubbly flow or thin air layer between the legs, Lambda type (Λ) has little to no air, and transition type has air partially filled in between legs. Figure 7.2 through Figure 7.4 present images of each type of the topologies.

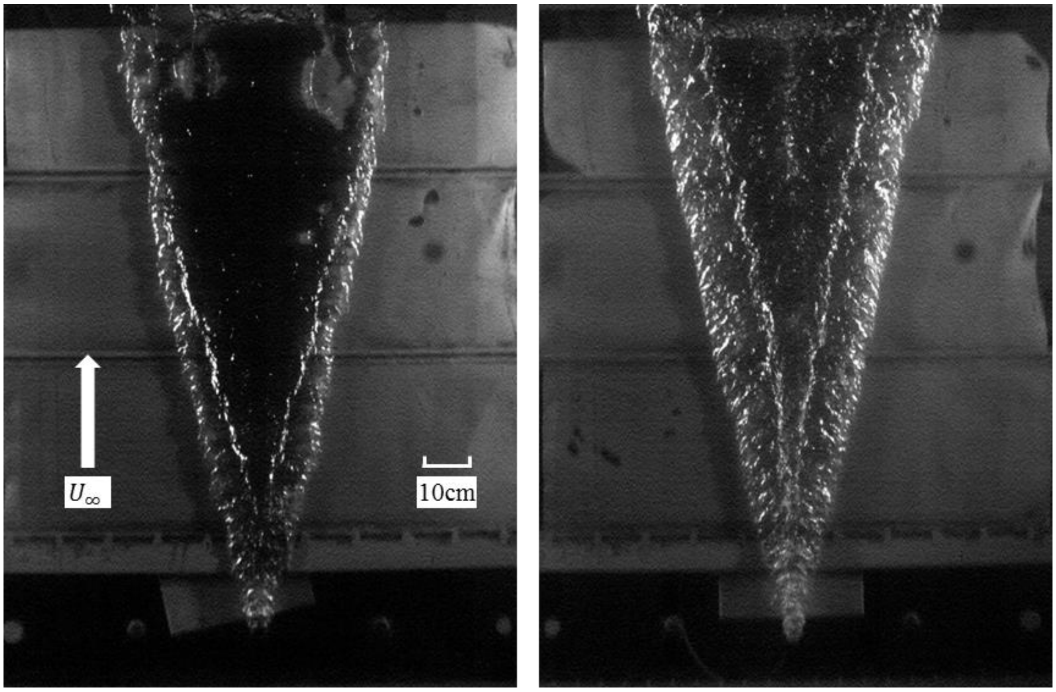

(a) (b)

Figure 7.2 Image of Delta type (Δ) jet. Condition of each cases are (a) D_i~ 20.0mm, β= 90°, U_∞= 2.0m/s, Q_i=4.3E-3m^3/s, and (b) D_i ~5.0mm, β =112.5°, U_∞ =3.0m/s, Q_i =2.5E-3m^3/s.

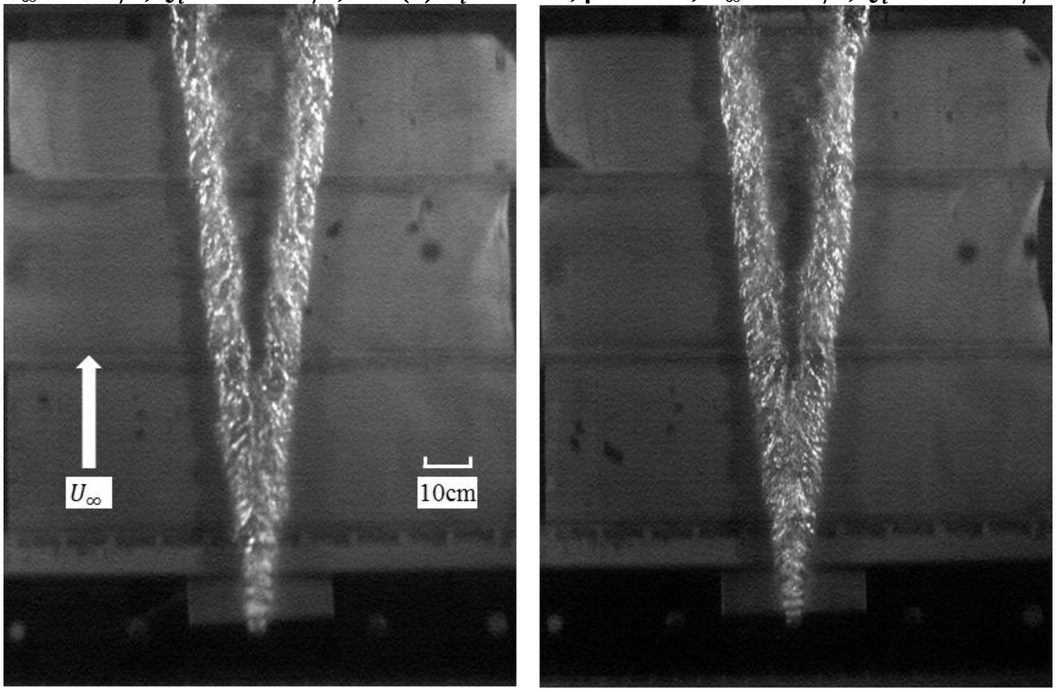

(a) (b)

Figure 7.3 Image of Lambda type (Λ) jet. Condition of each cases are (a) D_i~10.0mm, β =90.0°, U_∞=4.0m/s, Q_i=6.7E-3m^3/s, and (b) D_i ~10.0mm, β =45.0°, U_∞ =4.0m/s, Q_i =6.7E-3m^3/s.

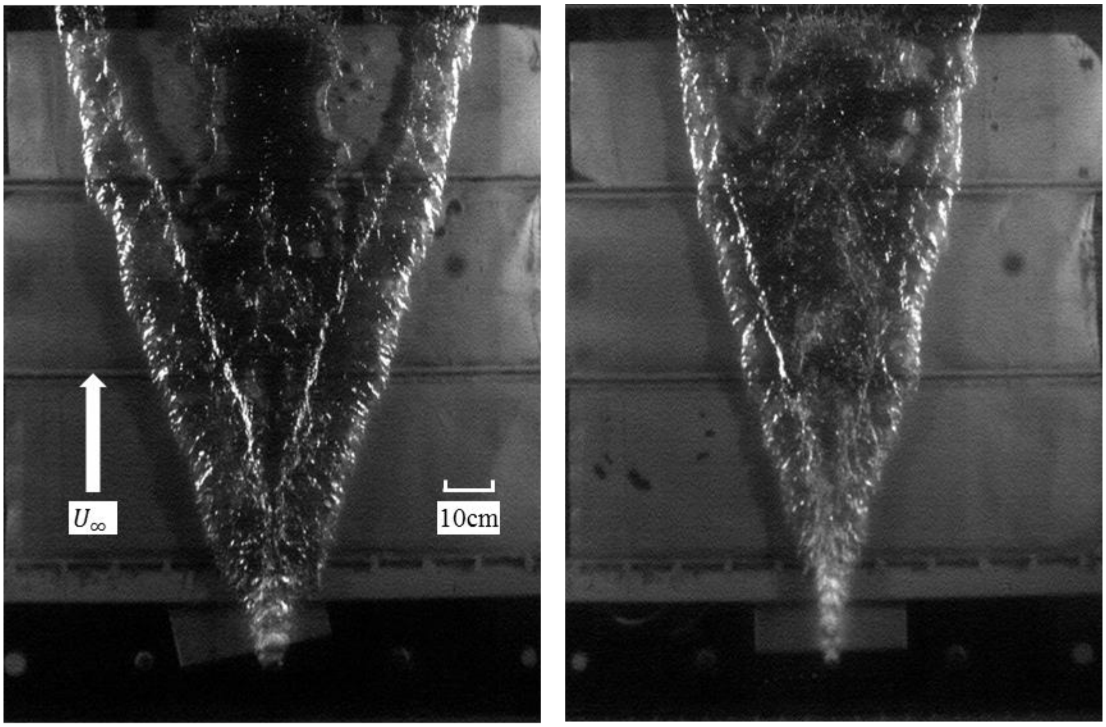

(a) (b)

Figure 7.4 Image of Transition type jet. Condition of each cases are (a) D_i ~20.0mm, β =90.0°, U_∞=2.0m/s, Q_i=1.1E-2m^3/s, and (b) D_i ~5.0mm, β =22.5°, U_∞ =2.0m/s, Q_i =3.0E-3m^3/s.

Figure 7.5 and Figure 7.6 present time series of the cavity topology for cases of Delta type (Δ) and Lambda type (Λ) as the barge passes over the stationary camera. Time interval of each case was chosen to show the flow from the injection hole to the end of the barge in 4 steps. The jet splits into two legs around the location where deflected jet meets the surface and size of the leg remains for certain length. As the flow develops along the surface, legs and air in between them flatten gradually. Then the flow broke down into bubbly flow.

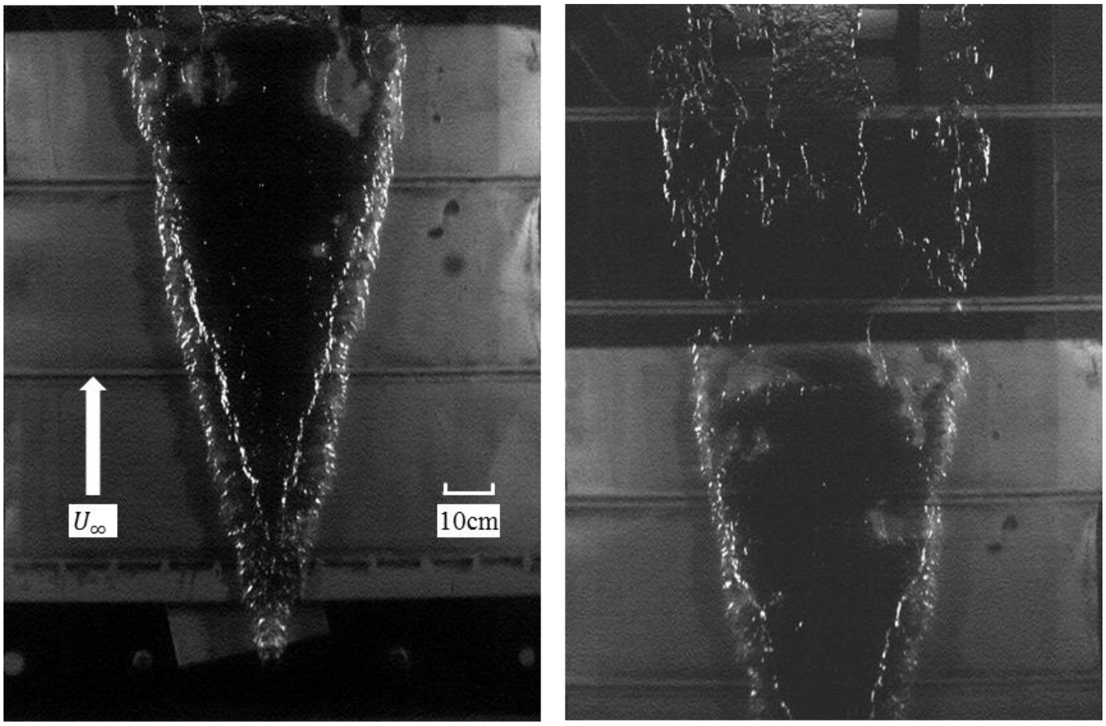

t = 0.00 sec t = 0.32 sec

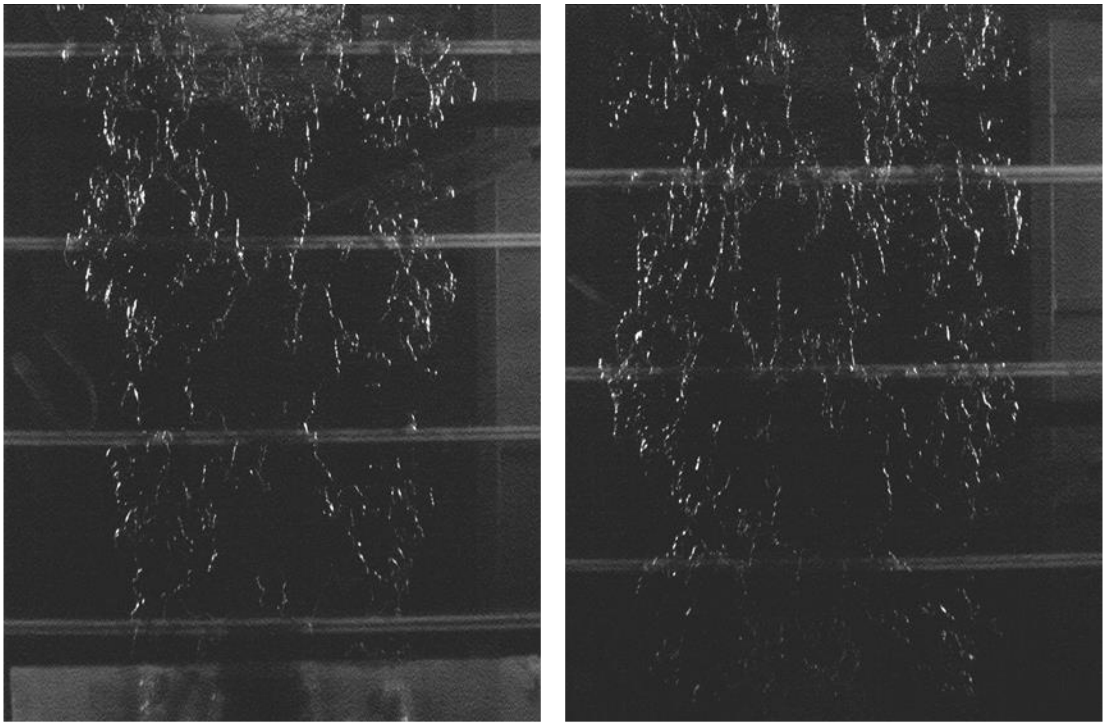

t = 0.64 sec t = 0.96 sec

Figure 7.5 Time series of Delta type (Δ) jet development from injection area to end of the barge. Condition of the case is D_i~ 20.0mm, β= 90°, U_∞= 2.0m/s, and Q_i=4.3E-3m^3/s.

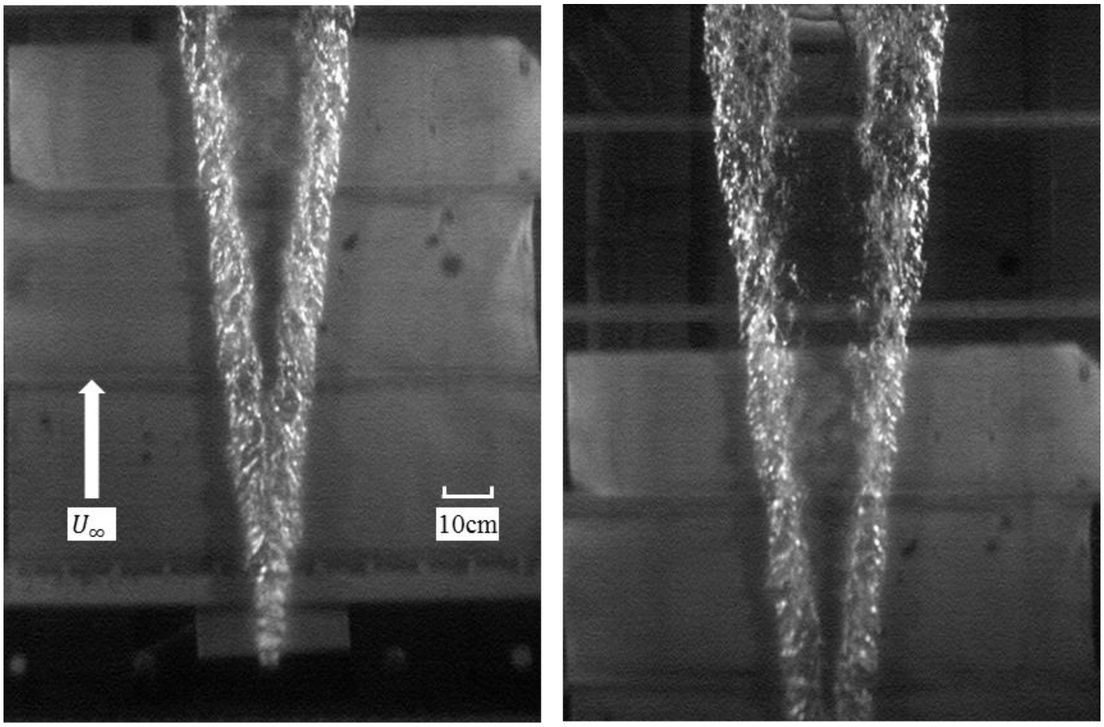

t = 0.00 sec　　t = 0.16 sec

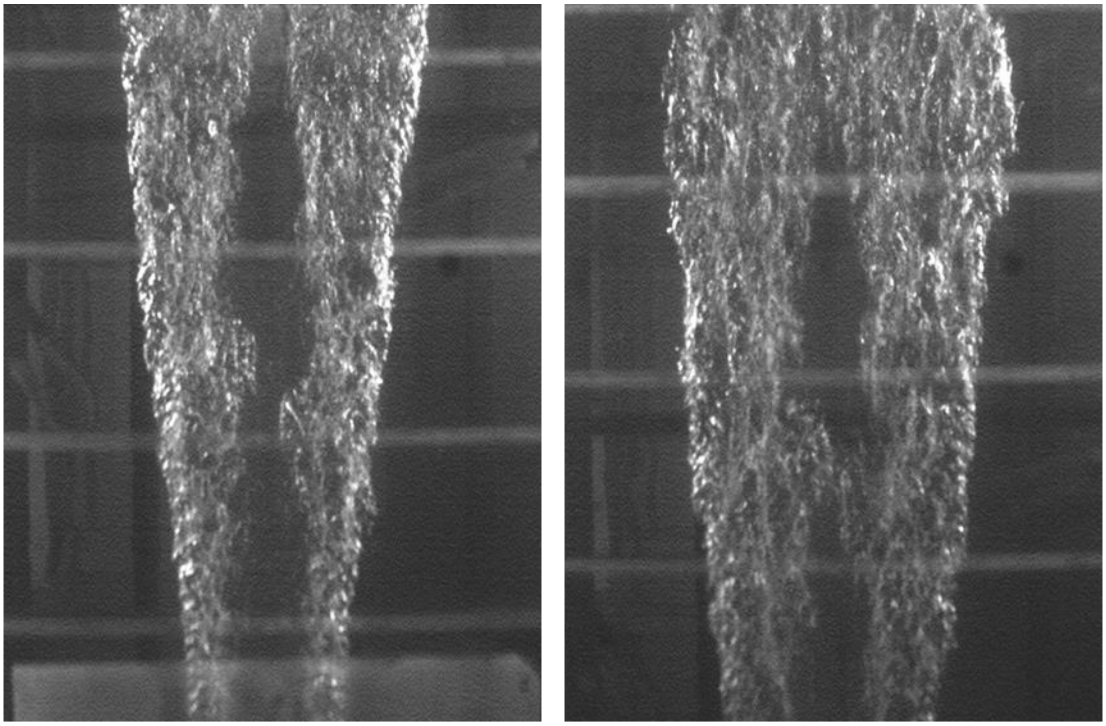

t = 0.32 sec　　t = 0.48 sec

Figure 7.6 Time series of Lambda type (Λ) jet development from injection area to end of the barge. Condition of the case is D_i ~10.0mm, β =90.0°, U_∞=4.0m$/s$, and Q_i=6.7E-3m^3/s.

7.2 Sweep angle of the leg (φ)

The sweep angle of the leg (φ) is measured and analyzed in this section. As it is presented in Figure 7.1, the sweep angle is the angle between the plane perpendicular to the cross-flow and leading edge of the leg. Angles were measured on images from at least 3 time frames and the average value was taken. Uncertainty of the measurement occurs due to fluctuation of the edge of the leg. Uncertainty of the sweep angle (φ) is $\pm 1.5°$.

Figure 7.7 through Figure 7.10 show how the sweep angle changes by varying cross-flow speed (U_∞), jet volume flow rate (Q_i), injection angle (β), and injection hole diameter (D_i). The sweep angle of the leg (φ) significantly varies with different cross-flow speed (U_∞), jet volume flow rate (Q_i), and injection hole diameter (D_i) when other conditions are fixed. Though varying injection angle (β) changes sweep angle (φ), variation is not significant and the trend is not consistent.

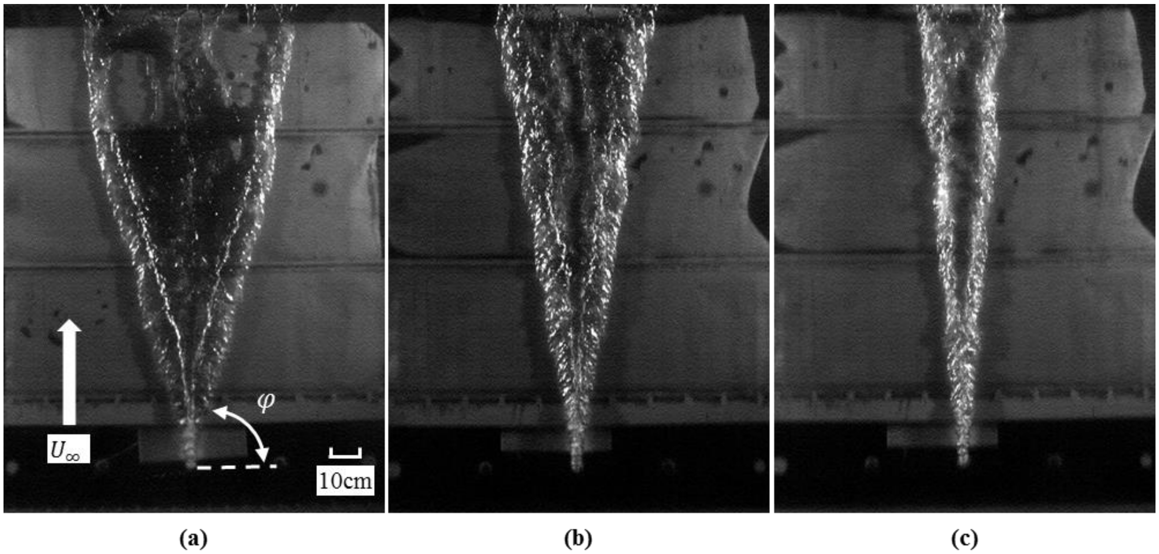

Figure 7.7 Comparison of sweep angle (φ) with changing cross-flow speed(U_∞); (a) U_∞=2.0m/s, (b) U_∞=3.0m/s, and (c) U_∞=4.0m/s. Other conditions are fixed; D_i~5.0mm, β =90.0°, and Q_i=2.0E-3m^3/s. Measured vortex sweep angles are (a) φ =74.2°, (b) φ =79.9°, and (c) φ =84.6°.

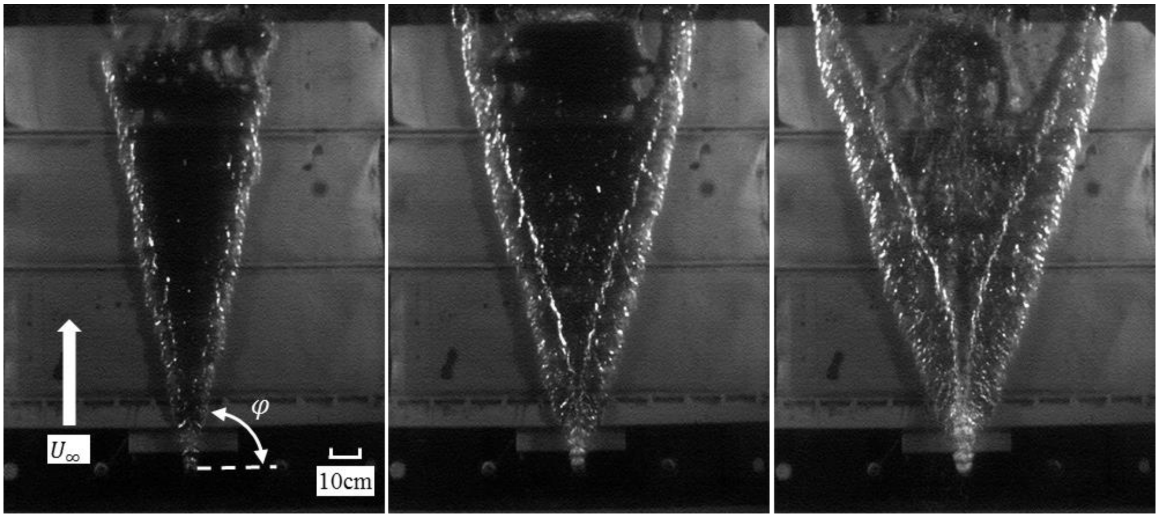

(a) (b) (c)

Figure 7.8 Comparison of sweep angle (φ) with changing jet volume flow rate (Q_i); (a) Q_i=1.7E-3m^3/s, (b) Q_i=3.3E-3m^3/s, and (c) Q_i=6.5E-3m^3/s. Other conditions are fixed; D_i~10.0mm, β =90.0°, and U_∞=2.0m$/s$. Measured vortex sweep angles are (a) φ =76.7°, (b) φ =72.2°, and (c) φ =68.8°.

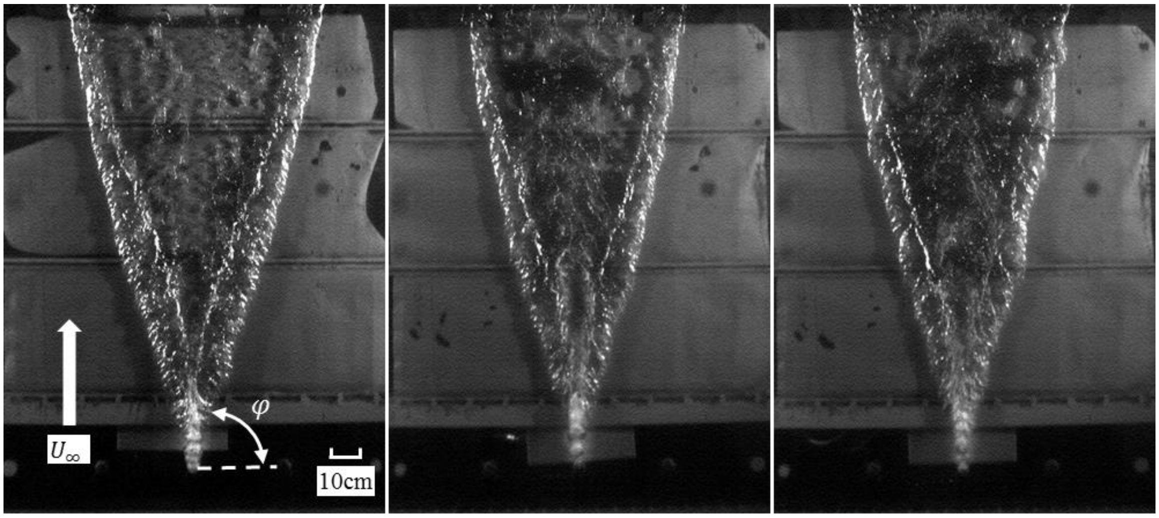

(a) (b) (c)

Figure 7.9 Comparison of sweep angle (φ) with changing injection angle (β); (a) β=90.0°, (b) β=45.0°, and (c) β=22.5°. Other conditions are fixed; D_i~5.0mm, U_∞=2.0m$/s$, and Q_i=3.0E-3m^3/s. Measured vortex sweep angles are (a) φ =71.7°, (b) φ =74.1°, and (c) φ =74.0°.

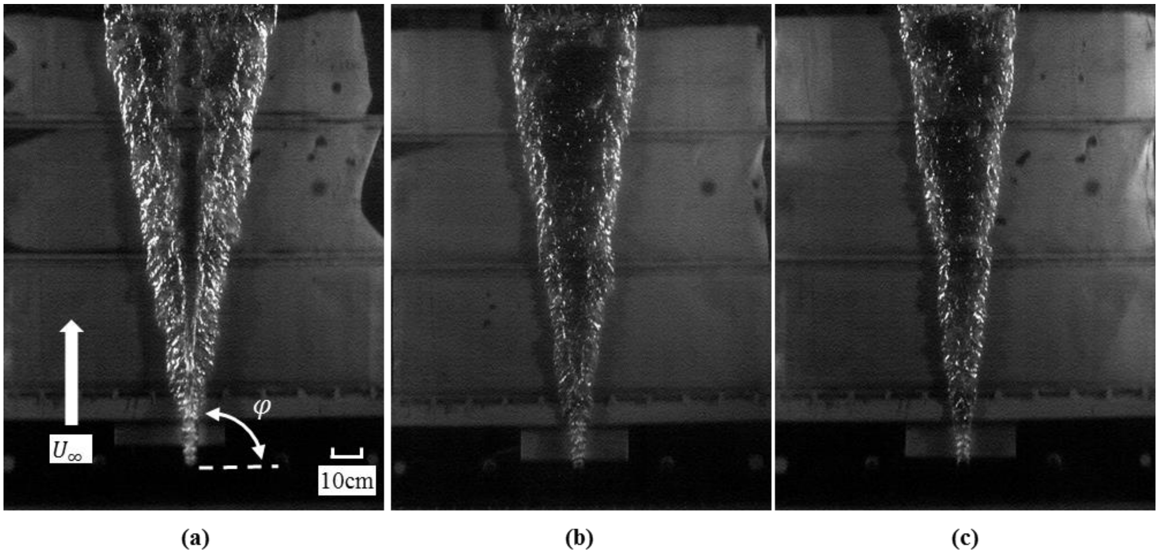

Figure 7.10 Comparison of sweep angle (φ) with changing injection hole diameter (D_i); (a) D_i~5.0mm, (b) D_i~10.0mm, and (c) D_i~20.0mm. Other conditions are fixed; β=90.0°, U_∞=3.0m/s, and Q_i=2.5E-3m^3/s. Measured vortex sweep angles are (a) φ =79.7°, (b) φ =81.8°, and (c) φ =82.4°.

Figure 7.11through Figure 7.26 present plots of sweep angle (φ) by varying cross-flow speed (U_∞), jet volume flow rate (Q_i), injection angle (β), and injection hole diameter (D_i). Throughout the plots, the marker type represents cross-flow speed, ○ U_∞=1.0m/s, ▷ U_∞=2.0m/s, ◁ U_∞=3.0m/s, ◇ U_∞=4.0m/s, and □ U_∞=5.0m/s. Solid marker(●)/dashed line represents data from Barge model I, δ_1, hollow marker(○)/solid line represents data from Barge model II, δ_2.

The sweep angle (φ) for different jet volume flow rate (Q_i) with varying injection hole diameter (D_i) and boundary layer profile (δ) are compared in Figure 7.11 through Figure 7.13. It was observed that the sweep angle (φ) significantly changes not only in magnitude but also in slope ($\frac{d\varphi}{dQ_i}$) by changing cross-flow speed (U_∞) at fixed injection hole diameter (D_i) and injection angle (β). Changes in the boundary layer thickness did not noticeably affect the sweep angle.

The sweep angle (φ) for different jet volume flow rate (Q_i) with varying injection angle (β) are compared in Figure 7.14 through Figure 7.21. The sweep angle (φ) decreases as jet volume flow rate (Q_i) increases in overall plots. However, changes of sweep angle by injection angle (β) is not significant considering the uncertainty of measurement ($\pm$1.5°). As shown in Figure 7.14 and Figure 7.18, the changing rate of sweep angle (φ) by jet volume flow rate (Q_i) at U_∞=1$\mathrm{m/s}$ is more rapid than other. Unusual aspect of cases with U_∞= 1$\mathrm{m/s}$ will be discussed in Chapter 9.

Figure 7.22 through Figure 7.26 show comparison of sweep angle(φ) for different jet volume flow rates (Q_i) with varying injection hole diameters (D_i). Changing the injection hole diameter also effect on the slope ($\frac{d\varphi}{dQ_i}$). Variation of the slope reduces as cross-flow speed (U_∞) increases, which means injection hole diameter (D_i) is critical parameter affecting on sweep angle (φ) but not as much as cross-flow speed (U_∞). Throughout all the conditions, sweep angle (φ) decreases with increasing jet volume flow rate (Q_i).

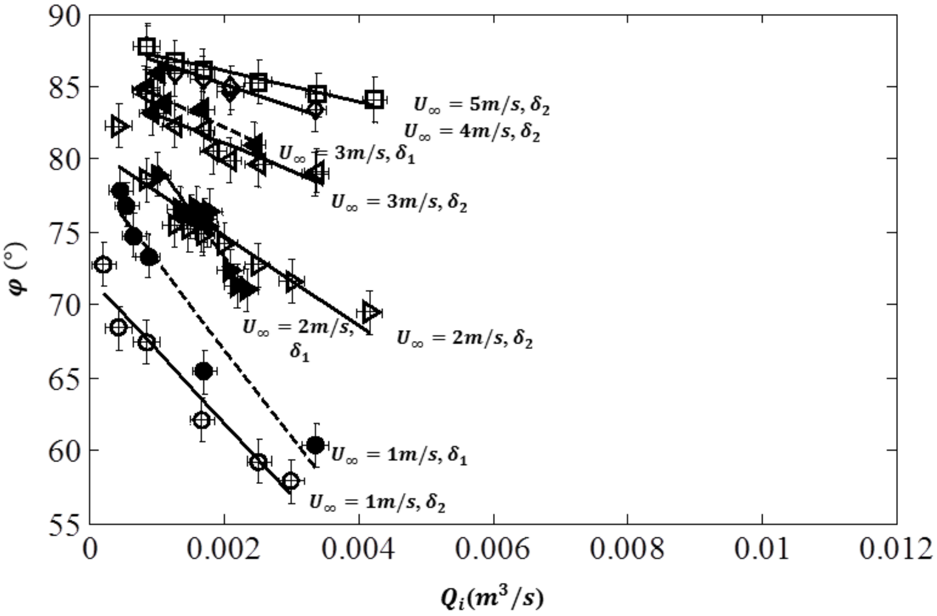

Figure 7.11 Sweep angle (φ) for different jet volume flow rate (Q_i) with varying cross-flow speed (U_∞) and boundary layer profile (δ) are compared. Diameter of injection hole (D_i) and injection angle (β) are fixed; D_i~5.0mm, β=90.0°.

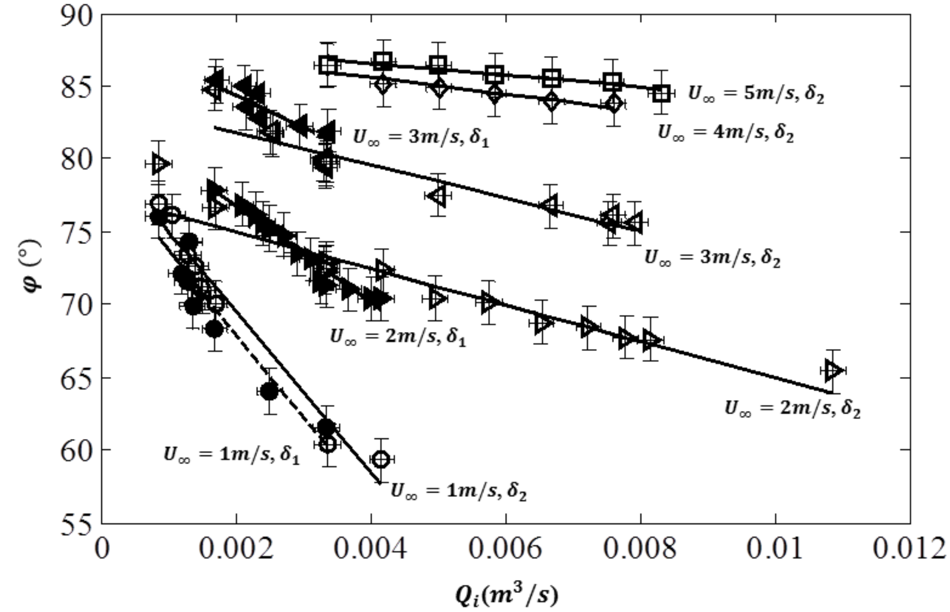

Figure 7.12 Sweep angle (φ) for different jet volume flow rate (Q_i) with varying cross-flow speed (U_∞) and boundary layer profile (δ) are compared. Diameter of injection hole (D_i) and injection angle (β) are fixed; D_i~10.0mm, β=90.0

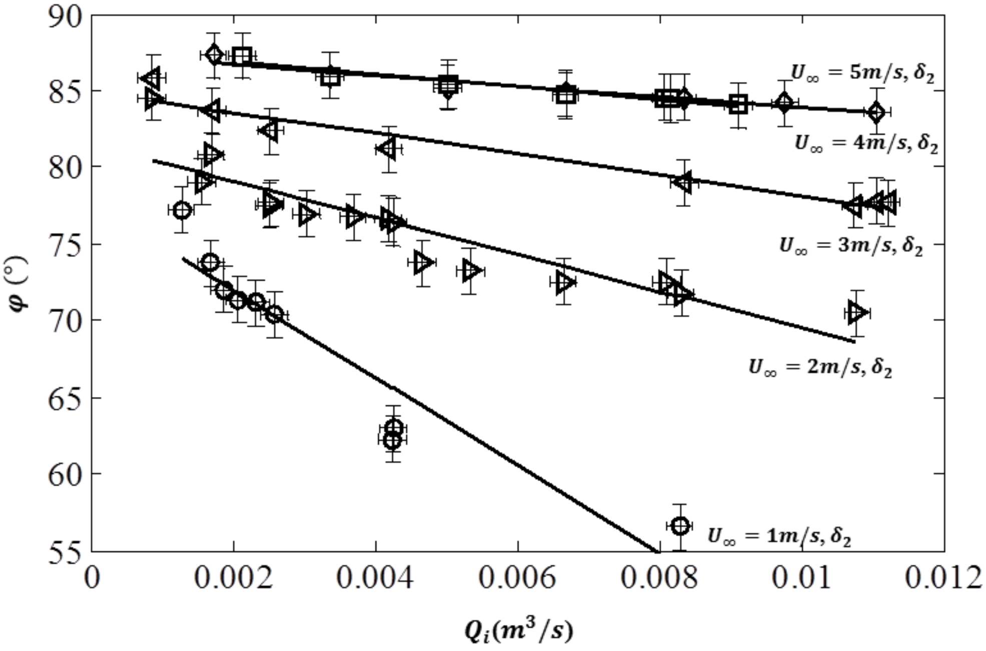

Figure 7.13 Sweep angle (φ) for different jet volume flow rate (Q_i) with varying cross-flow speed (U_∞) and boundary layer profile (δ) are compared. Diameter of injection hole (D_i) injection angle(β), and boundary layer profile(δ) are fixed; D_i~20.0mm, β=90.0°, $\delta = \delta_2$.

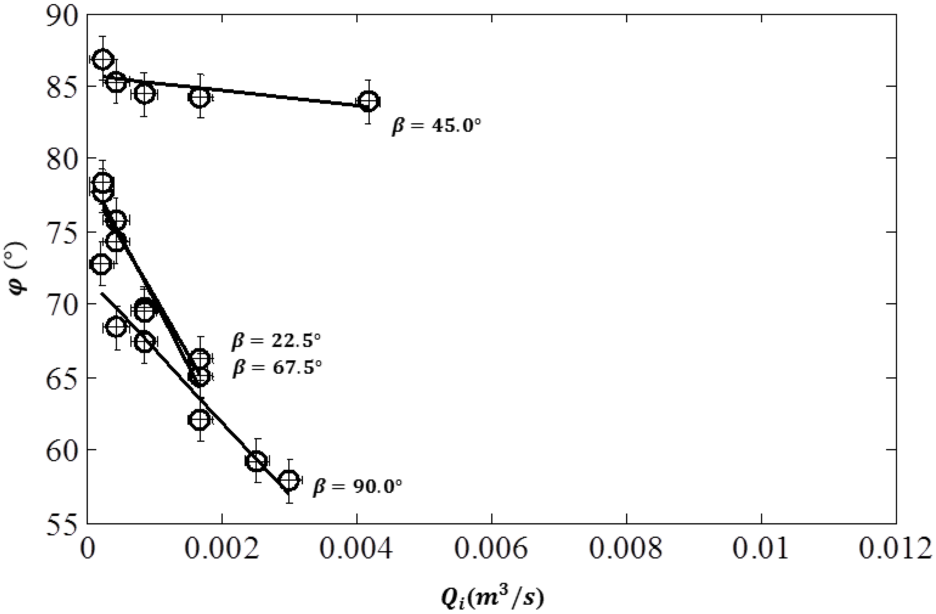

Figure 7.14 Sweep angle (φ) for different jet volume flow rate (Q_i) with varying injection angle (β) are compared. Diameter of injection hole (D_i) cross-flow speed (U_∞), and boundary layer profile (δ) are fixed; D_i~5.0mm, U_∞=1.0m/s, $\delta = \delta_2$

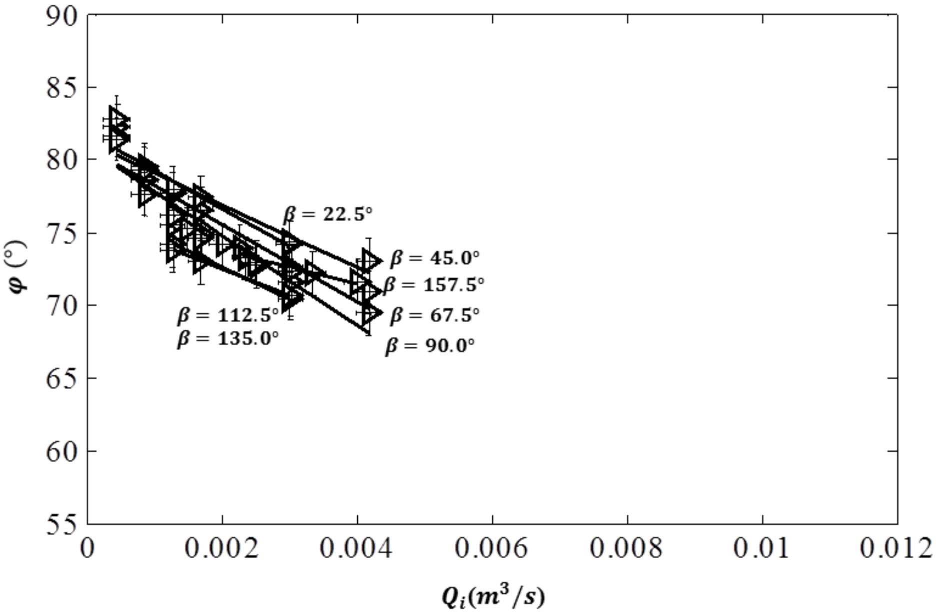

Figure 7.15 Sweep angle (φ) for different jet volume flow rate (Q_i) with varying injection angle (β) are compared. Diameter of injection hole (D_i) cross-flow speed (U_∞), and boundary layer profile (δ) are fixed; D_i~5.0mm, U_∞=2.0m/s, $\delta = \delta_2$

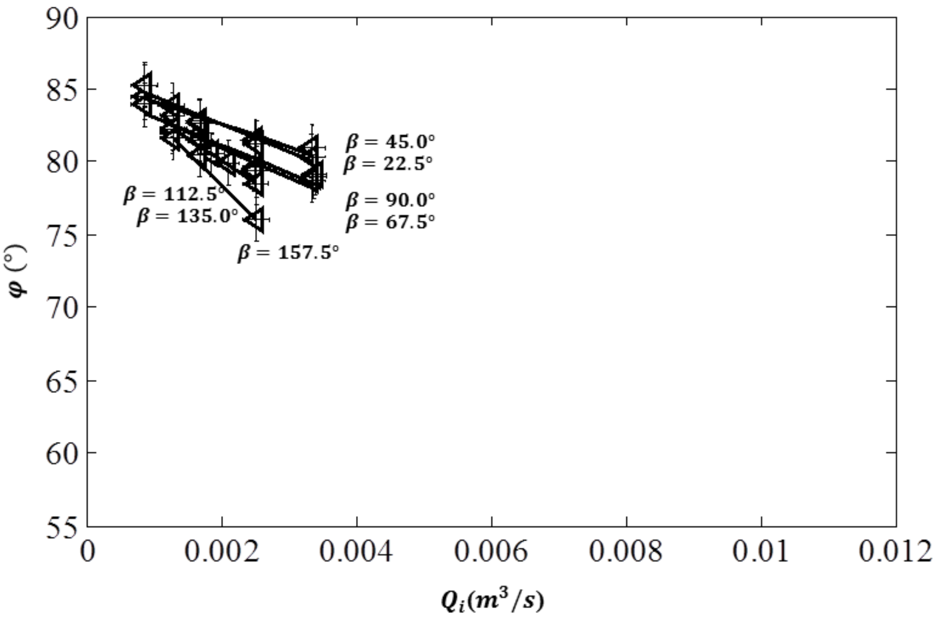

Figure 7.16 Sweep angle (φ) for different jet volume flow rate (Q_i) with varying injection angle (β) are compared. Diameter of injection hole (D_i) cross-flow speed (U_∞), and boundary layer profile (δ) are fixed; D_i~5.0mm, U_∞=3.0m/s, $\delta = \delta_2$

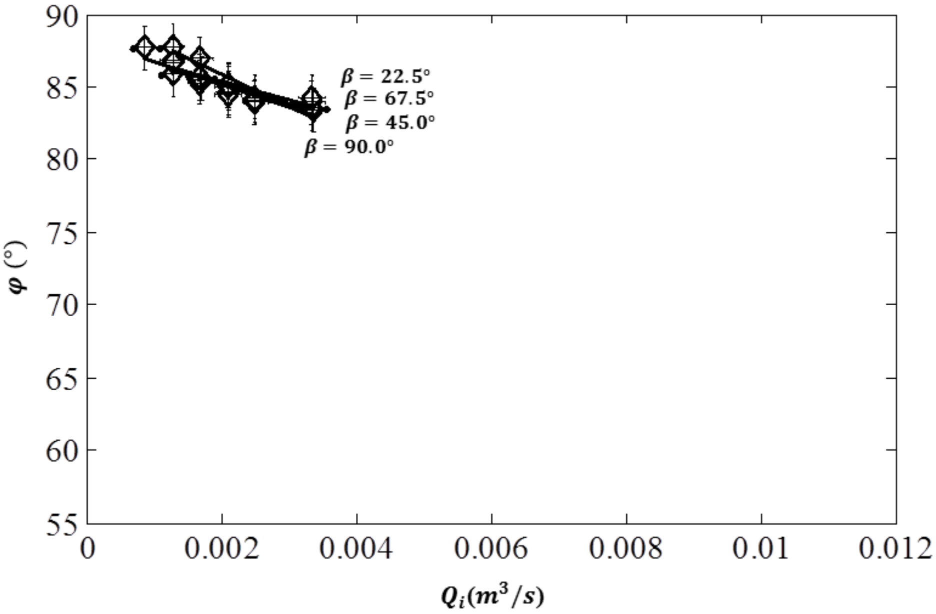

Figure 7.17 Sweep angle (φ) for different jet volume flow rate (Q_i) with varying injection angle (β) are compared. Diameter of injection hole (D_i) cross-flow speed (U_∞), and boundary layer profile (δ) are fixed; D_i~5.0mm, U_∞=4.0m/s, $\delta = \delta_2$

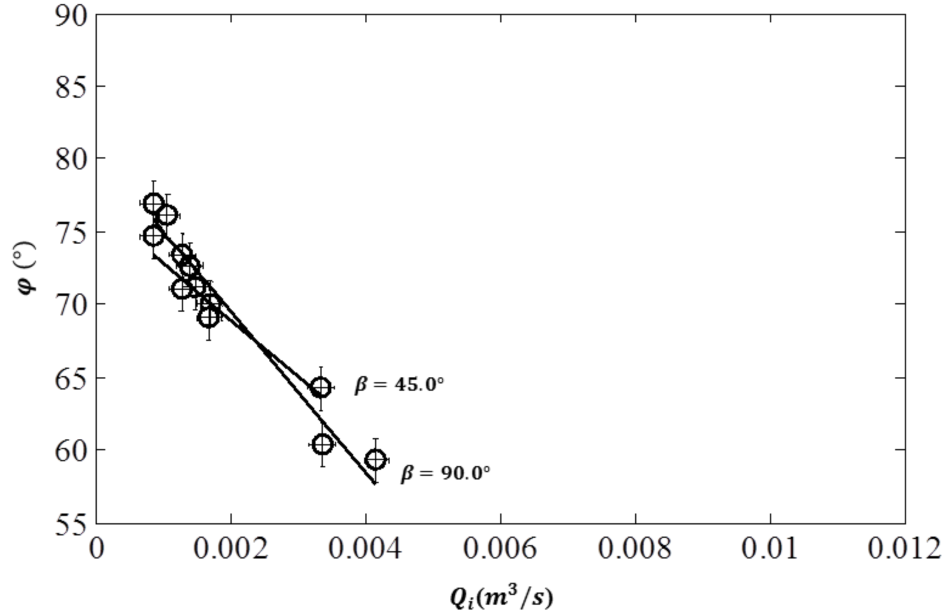

Figure 7.18 Sweep angle (φ) for different jet volume flow rate (Q_i) with varying injection angle (β) are compared. Diameter of injection hole (D_i) cross-flow speed (U_∞), and boundary layer profile (δ) are fixed; D_i~10.0mm, U_∞=1.0m/s, $\delta = \delta_2$

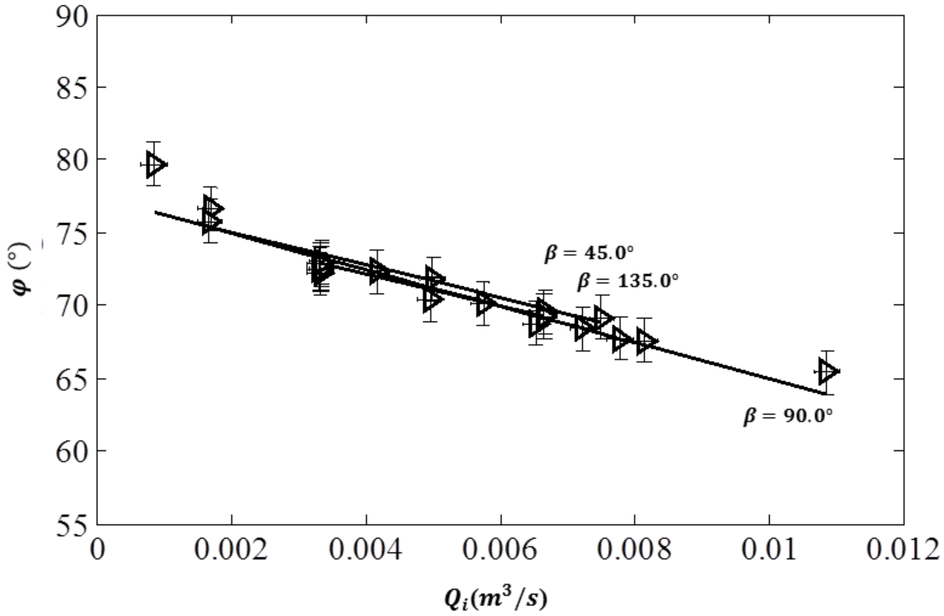

Figure 7.19 Sweep angle (φ) for different jet volume flow rate (Q_i) with varying injection angle (β) are compared. Diameter of injection hole (D_i) cross-flow speed (U_∞), and boundary layer profile (δ) are fixed; D_i~10.0mm, U_∞=2.0m/s, $\delta = \delta_2$

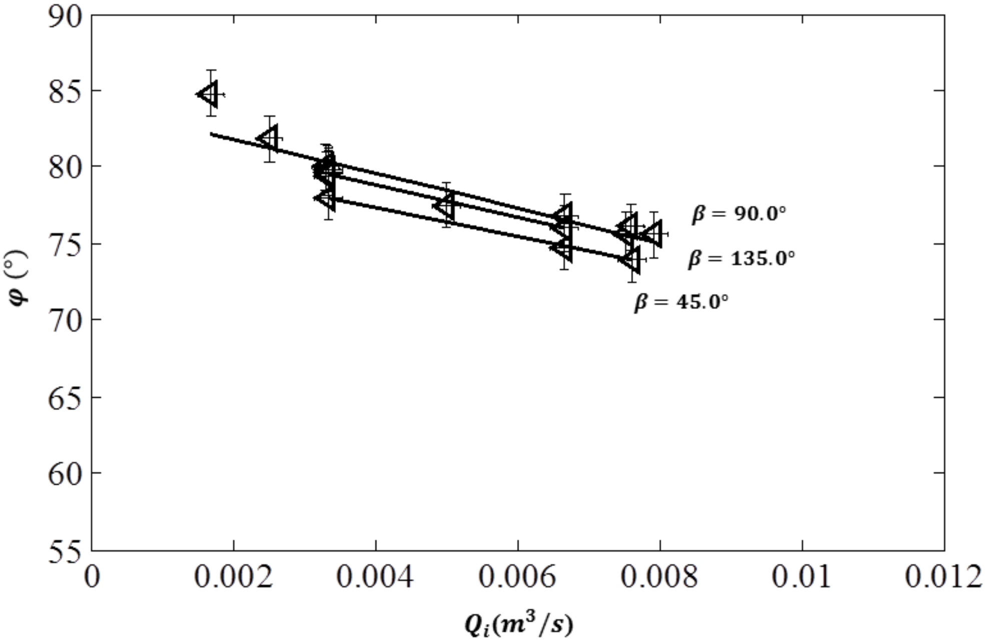

Figure 7.20 Sweep angle (φ) for different jet volume flow rate (Q_i) with varying injection angle (β) are compared. Diameter of injection hole (D_i) cross-flow speed (U_∞), and boundary layer profile (δ) are fixed; D_i~10.0mm, U_∞=3.0m/s, $\delta = \delta_2$

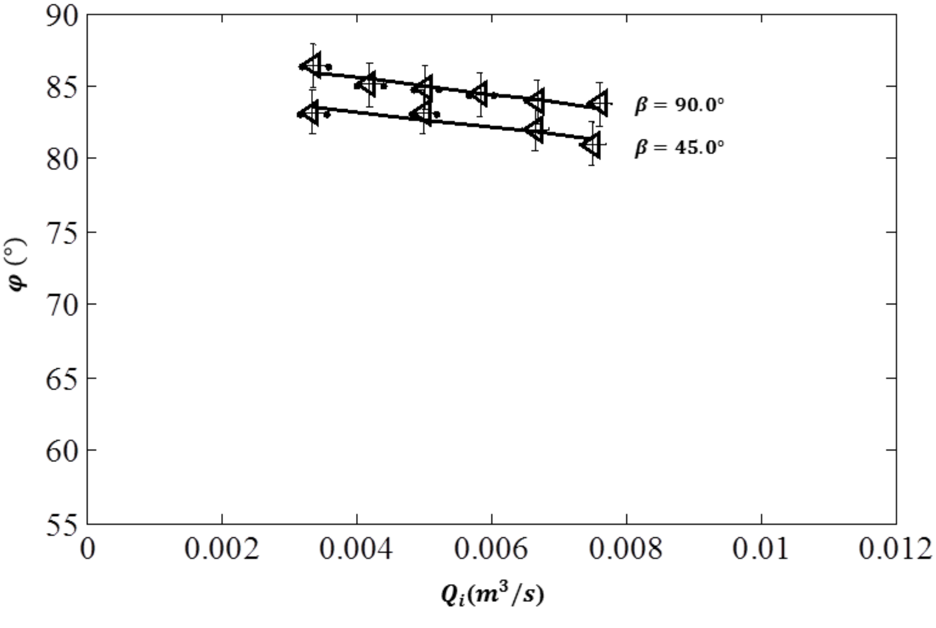

Figure 7.21 Sweep angle (φ) for different jet volume flow rate (Q_i) with varying injection angle (β) are compared. Diameter of injection hole (D_i) cross-flow speed (U_∞), and boundary layer profile (δ) are fixed; D_i~10.0mm, U_∞=4.0m/s, $\delta = \delta_2$

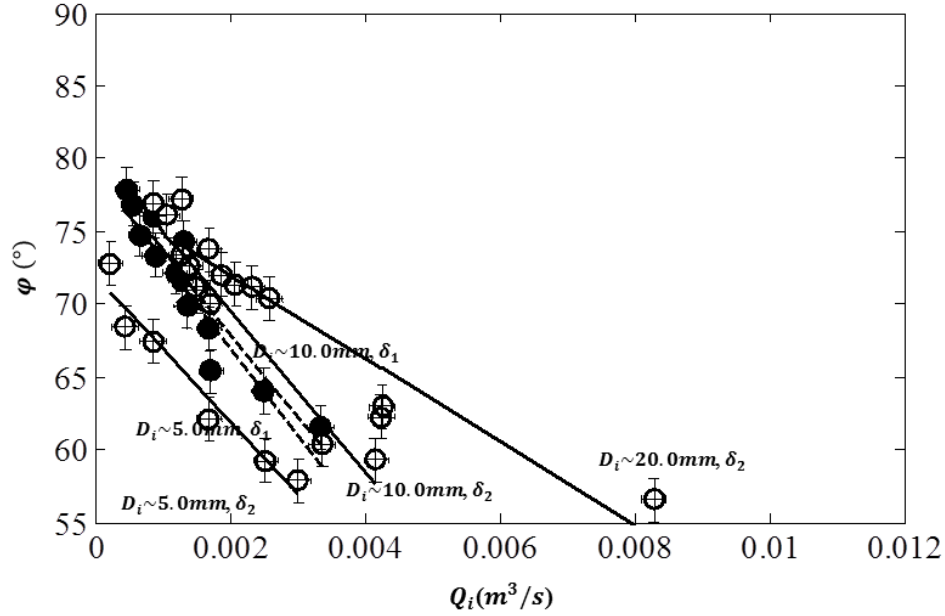

Figure 7.22 Sweep angle (φ) for different jet volume flow rate (Q_i) with varying injection hole diameter (D_i), and boundary layer profiles (δ) are compared. Injection angle (β) and cross-flow speed (U_∞) are fixed; β=90.0mm and U_∞=1.0m/s.

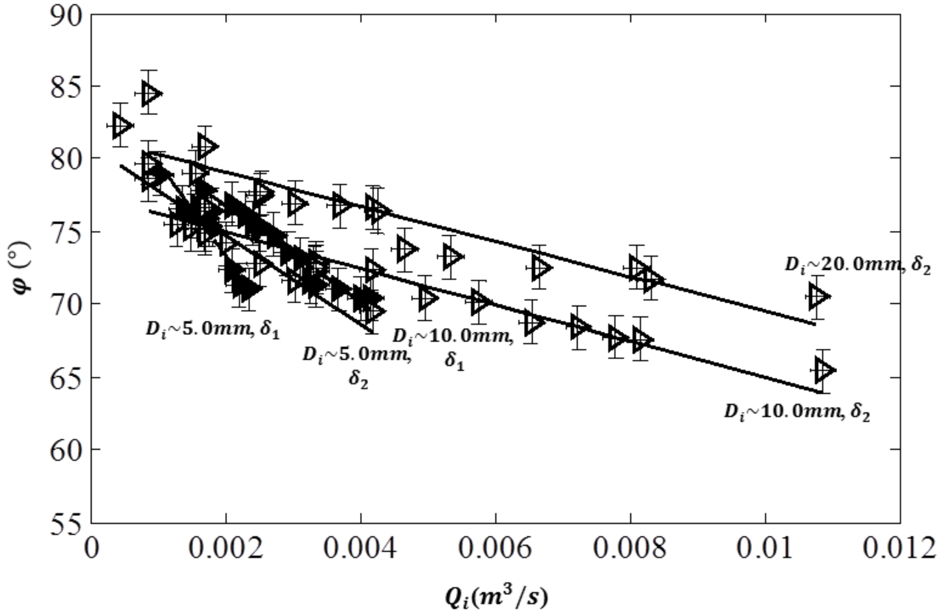

Figure 7.23 Sweep angle (φ) for different jet volume flow rate (Q_i) with varying injection hole diameter (D_i), and boundary layer profiles (δ) are compared. Injection angle (β) and cross-flow speed (U_∞) are fixed; β=90.0mm and U_∞=2.0m/s.

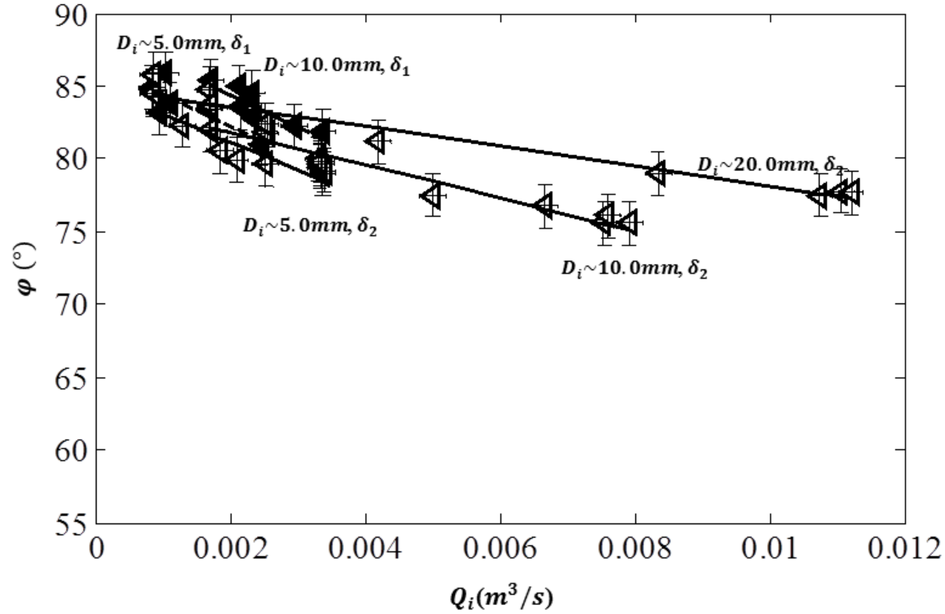

Figure 7.24 Sweep angle (φ) for different jet volume flow rate (Q_i) with varying injection hole diameter (D_i), and boundary layer profiles (δ) are compared. Injection angle (β) and cross-flow speed (U_∞) are fixed; β=90.0mm and U_∞=3.0m/s.

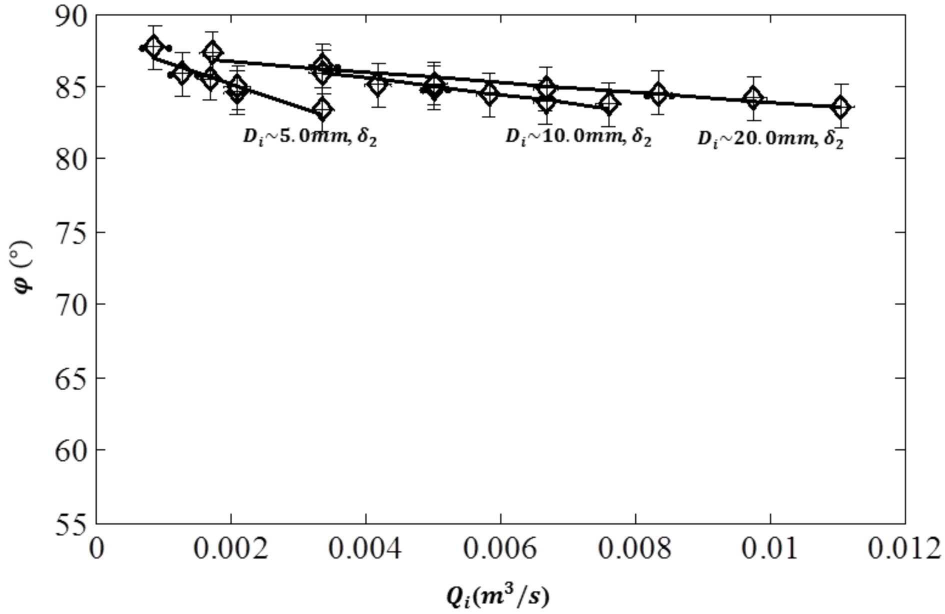

Figure 7.25 Sweep angle (φ) for different jet volume flow rate (Q_i) with varying injection hole diameter (D_i) are compared. Injection angle (β) and cross-flow speed (U_∞) are fixed; β=90.0mm and U_∞=4.0m/s.

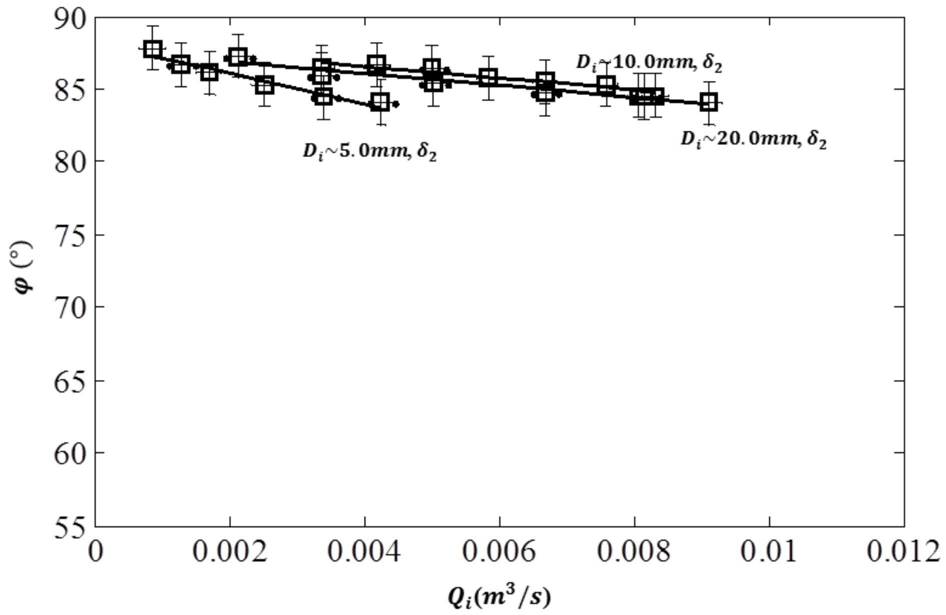

Figure 7.26 Sweep angle (φ) for different jet volume flow rate (Q_i) with varying injection hole diameter (D_i) are compared. Injection angle (β) and cross-flow speed (U_∞) are fixed; β=90.0mm and U_∞=5.0m$/s$.

In summary, cross-flow speed (U_∞), jet volume flow rate (Q_i), and injection hole diameter (D_i) are major parameters affecting the sweep angle (φ). However, the boundary layer thickness (δ) and injection angle (β) do not affect the sweep angle (φ) significantly.

7.3 Chord length of leg (C)

The chord of the gas leg measured perpendicular to its leading edge was measured and defined as "Chord length (C)". About 25cm long spanwise segments of the leg, which includes the thickest part of the leg, were chosen on legs to measure the chord. The distance between the edge on 3 to 4 locations on each segments were measured and average value was taken as the chord length. Figure 7.27 illustrates how the chord length was measured. The uncertainty of the measurement occurs due to fluctuation of the edge of the leg, and the uncertainty of the chord length (C) is $\pm$5mm.

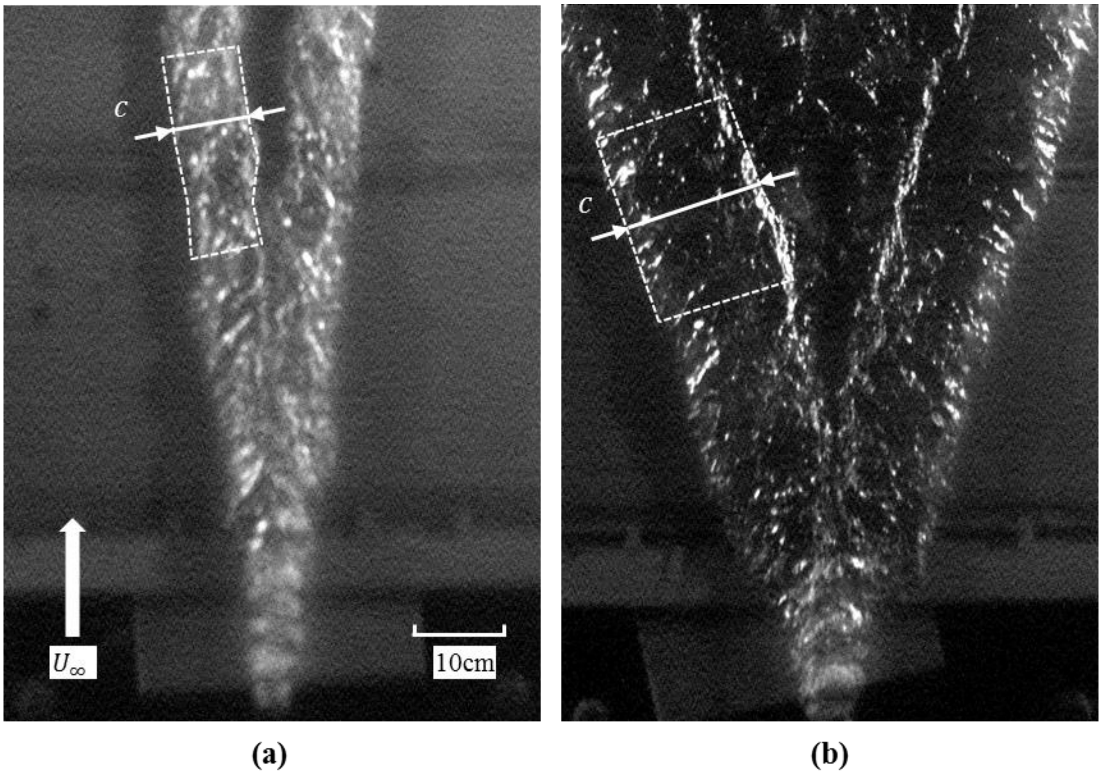

Figure 7.27 Chord length of the leg(C) is defined in the images of closer view on the jet in the vicinity of injection hole. Dashed box indicates part where chord length is measured. Condition of each cases are (a) D_i~10.0mm, β =90.0°, U_∞=4.0m/s, Q_i=6.7E-3m^3/s and (b) D_i~20.0mm, β =90.0°, U_∞=2.0m/s, Q_i=1.1E-2m^3/s.

In Figure 7.28 through Figure 7.31, the size of the leg are compared for different cross-flow speed (U_∞), jet volume flow rate (Q_i), injection angle (β), and injection hole diameter (D_i). There are noticeable changes on chord length (C) with different cross-flow speed (U_∞), jet volume flow rate (Q_i), injection hole diameter (D_i), and injection angle (β).

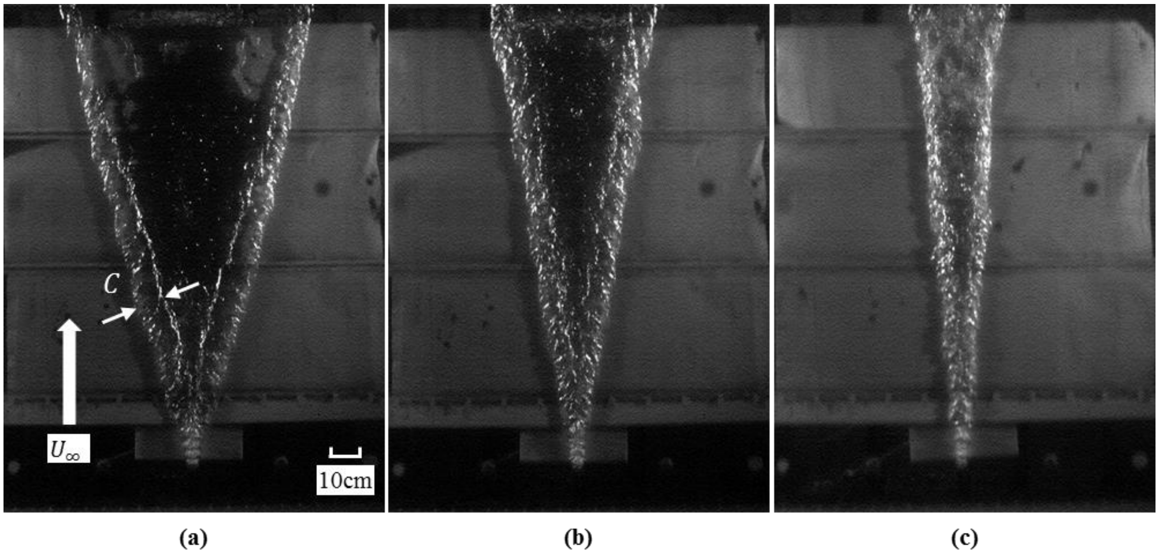

Figure 7.28 Comparison of Chord length of the leg (C) with changing cross-flow speed (U_∞); (a) U_∞=2.0m$/s$, (b) U_∞=3.0m$/s$, and (c) U_∞=4.0m$/s$. Other conditions are fixed; D_i~20.0mm, β =90.0°, and Q_i=3.4E-3m^3/s. Measured Chord lengths are (a) C =86.1mm, (b) C =69.7mm, and (c) C =46.8mm.

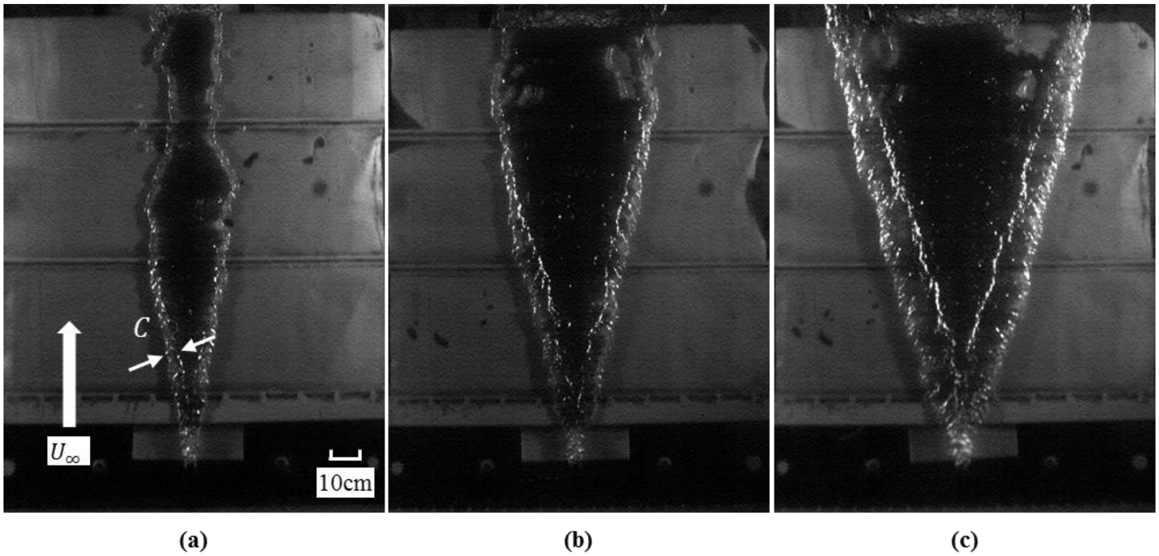

Figure 7.29 Comparison of Chord length of the leg (C) with changing jet volume flow rate (Q_i); (a) Q_i=1.7E-3m^3/s, (b) Q_i=3.0E-3m^3/s, and (c) Q_i=6.7E-3m^3/s. Other conditions are fixed; D_i~20.0mm, β =90.0°, and U_∞=2.0m$/s$. Measured Chord lengths are (a) C =23.0mm, (b) C =57.2mm, and (c) C =103.5mm.

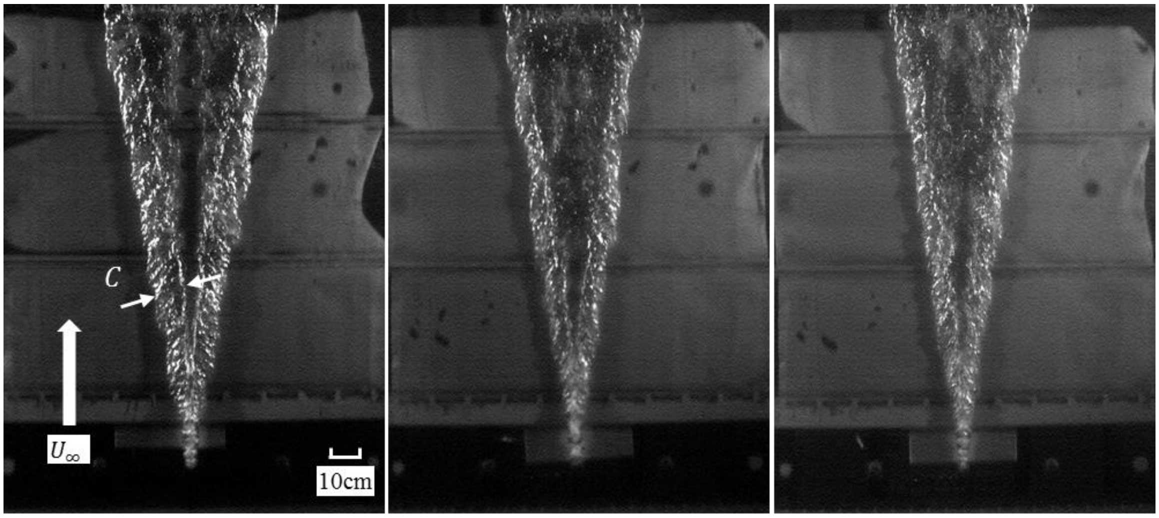

(a) (b) (c)

Figure 7.30 Comparison of Chord length of the leg (C) with changing injection angle (β); (a) β =90.0°, (b) β =45.0°, and (c) β =22.5°. Other conditions are fixed; D_i~5.0mm, Q_i=2.5E-3m^3/s , and U_∞=2.0m/s. Measured Chord lengths are (a) C =89.9mm, (b) C =68.4mm, and (c) C =62.8mm.

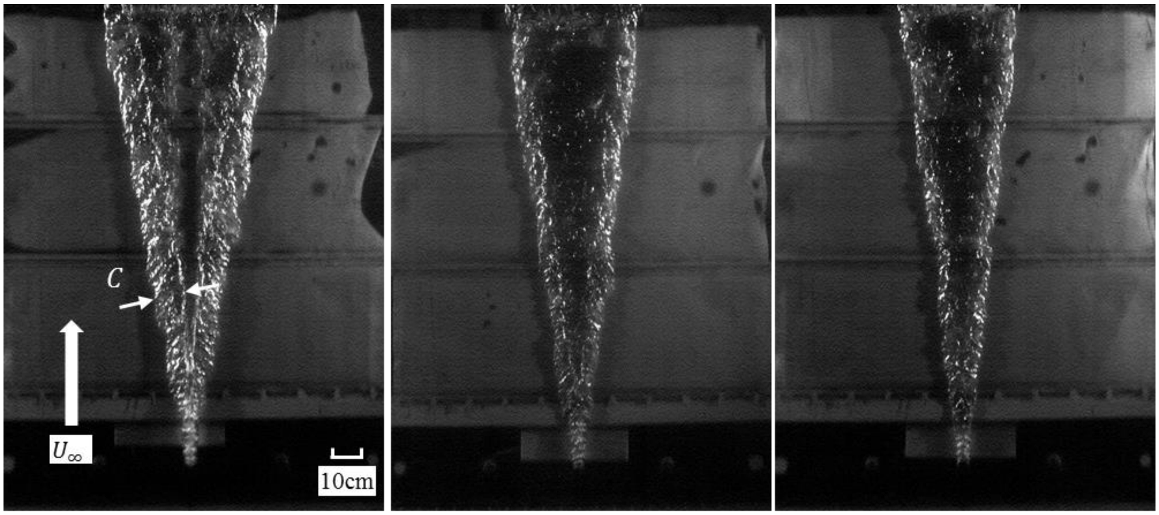

(a) (b) (c)

Figure 7.31 Comparison of Chord length of the leg (C) with changing injection hole diameter (D_i); (a) D_i~5.0mm, (b) D_i~10.0mm, and (c) D_i~20.0mm. Other conditions are fixed; β=90.0°, U_∞=3.0m/s, and Q_i=2.5E-3m^3/s. Measured Chord lengths are (a) C =89.9mm, (b) C =65.5mm, and (c) C =40.0mm.

Figure 7.32 through Figure 7.47 present plots of chord length (C) by varying cross-flow speed (U_∞), jet volume flow rate (Q_i), injection angle (β), and injection hole diameter (D_i). Throughout the plots, marker type represents cross-flow speed, ○ U_∞=1.0m/s, ▷ U_∞=2.0m/s, ◁ U_∞=3.0m/s, ◇ U_∞=4.0m/s, and □ U_∞=5.0m/s. Solid markers (●)/dashed lines represent data from Barge model I, δ_1, and hollow markers (○)/solid lines represent data from Barge model II, δ_2.

Chord length of leg (C) for different jet volume flow rates (Q_i) with varying injection hole diameter (D_i) and boundary layer thickness (δ) are compared in Figure 7.32 through Figure 7.34. Boundary layer thickness (δ) significantly effects the chord length of the legs. Response of the chord length to cross-flow speed tends to divide into two regime, high speed and low speed cases. Cases with U_∞=1m/s do not clearly belong to any regime.

Chord length (C) for different jet volume flow rate (Q_i) with varying injection angle (β) are compared in Figure 7.35 through Figure 7.42. Comparison of Chord length (C) for different jet volume flow rates (Q_i) with varying injection hole diameter (D_i) are presented in Figure 7.43 though Figure 7.47. Throughout all the plots, chord length (C) increases by increasing the jet volume flow rate (Q_i). From the figures, it is observed that injection angle (β) does not change the chord length significantly. However, the role of injection hole diameter (D_i) is noticeable. It is more significant in lower cross-flow speed (U_∞) than in higher cross-flow speed (U_∞).

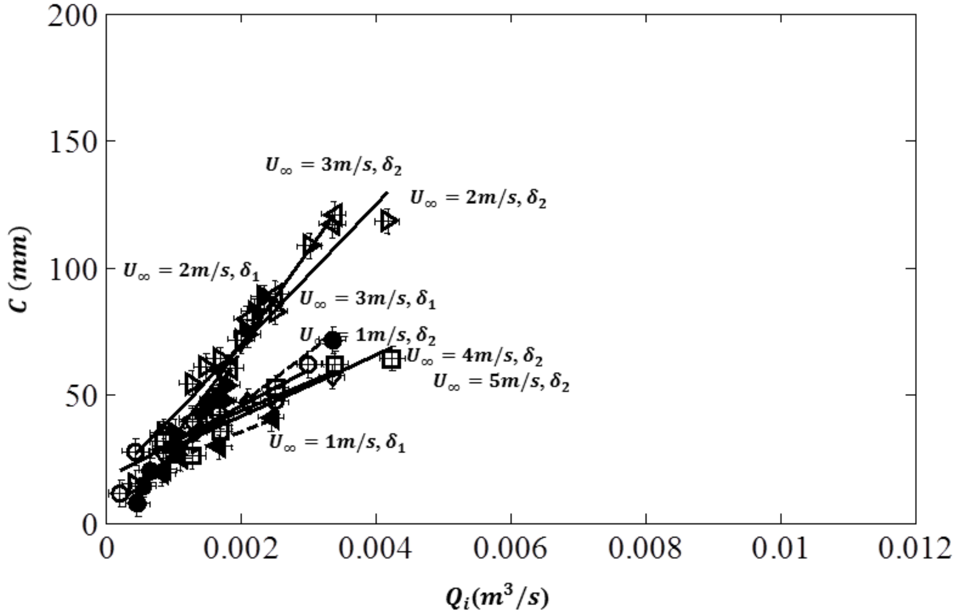

Figure 7.32 Chord length of the leg (C) for different jet volume flow rate (Q_i) with varying cross-flow speed (U_∞) and boundary layer profile (δ) are compared. Diameter of injection hole (D_i) and injection angle (β) are fixed; D_i~5.0mm, β=90.0°.

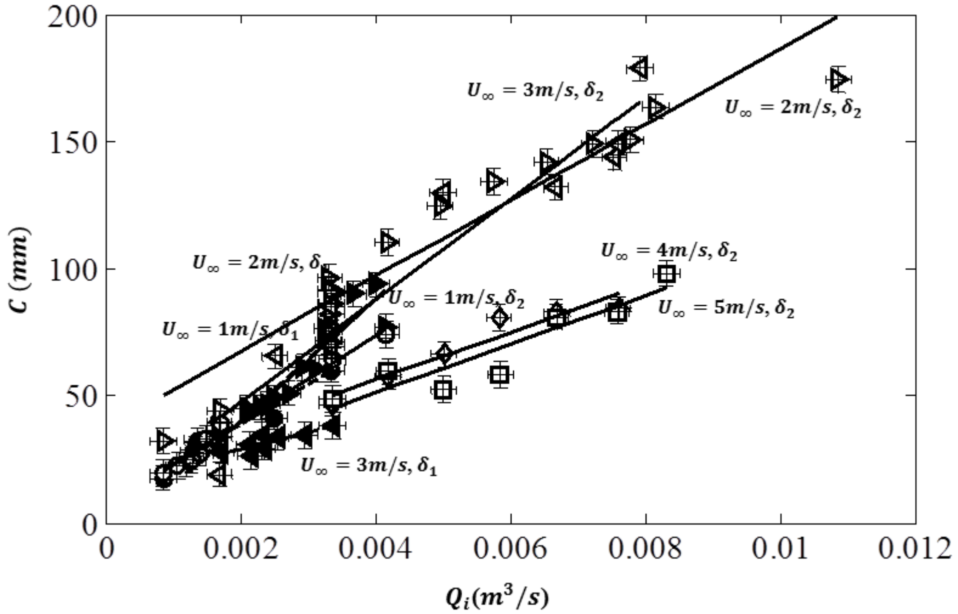

Figure 7.33 Chord length of the leg (C) for different jet volume flow rate (Q_i) with varying cross-flow speed (U_∞) and boundary layer profile (δ) are compared. Diameter of injection hole (D_i) and injection angle (β) are fixed; D_i~10.0mm, β=90.0°.

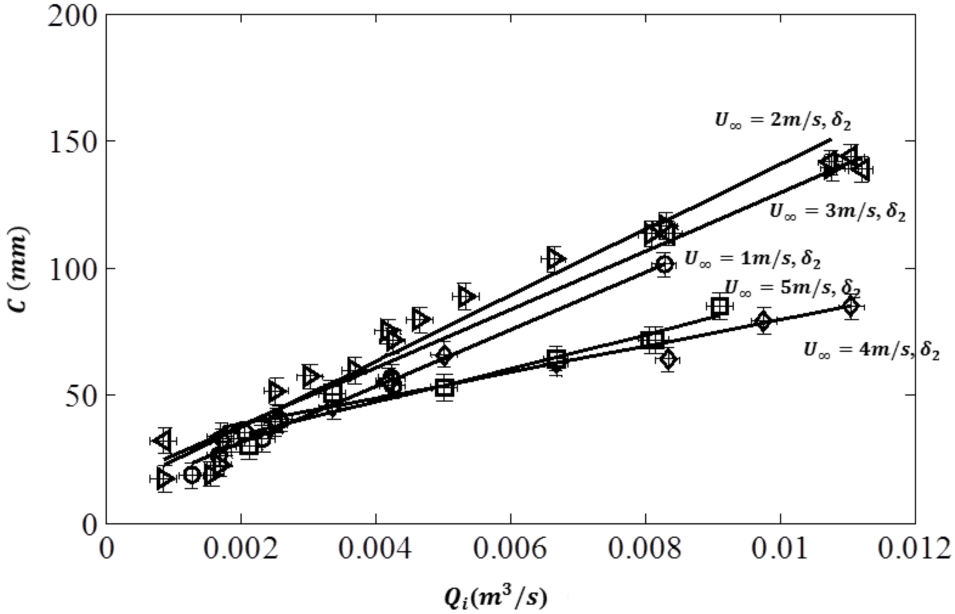

Figure 7.34 Chord length of the leg (C) for different jet volume flow rate (Q_i) with varying cross-flow speed (U_∞) and boundary layer profile (δ) are compared. Diameter of injection hole (D_i) and injection angle (β) are fixed; D_i~20.0mm, β=90.0°.

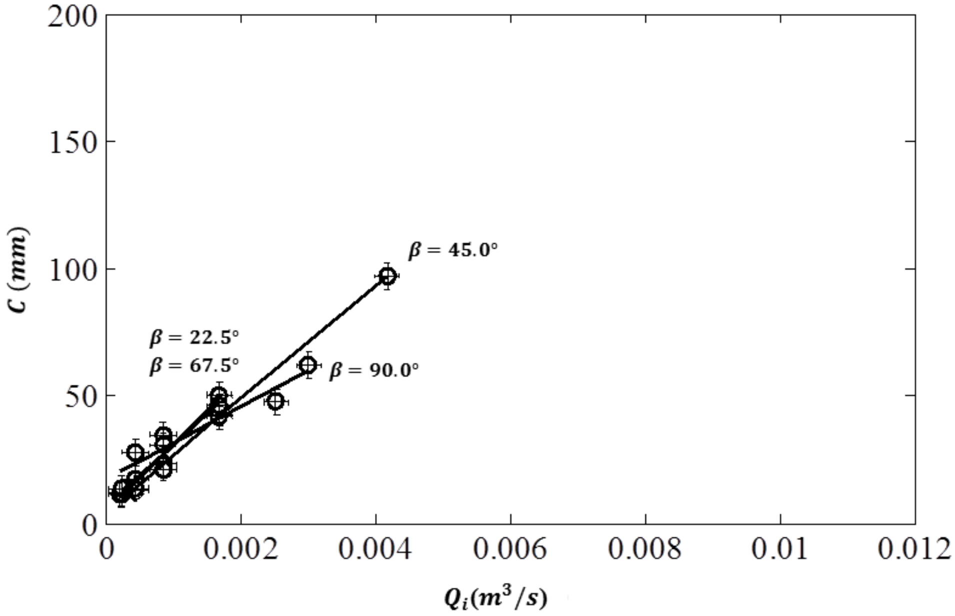

Figure 7.35 Chord length of the leg (C) for different jet volume flow rate (Q_i) with varying injection angle (β) are compared. Diameter of injection hole (D_i) cross-flow speed (U_∞), and boundary layer profile (δ) are fixed; D_i~5.0mm, U_∞=1.0m/s, $\delta = \delta_2$

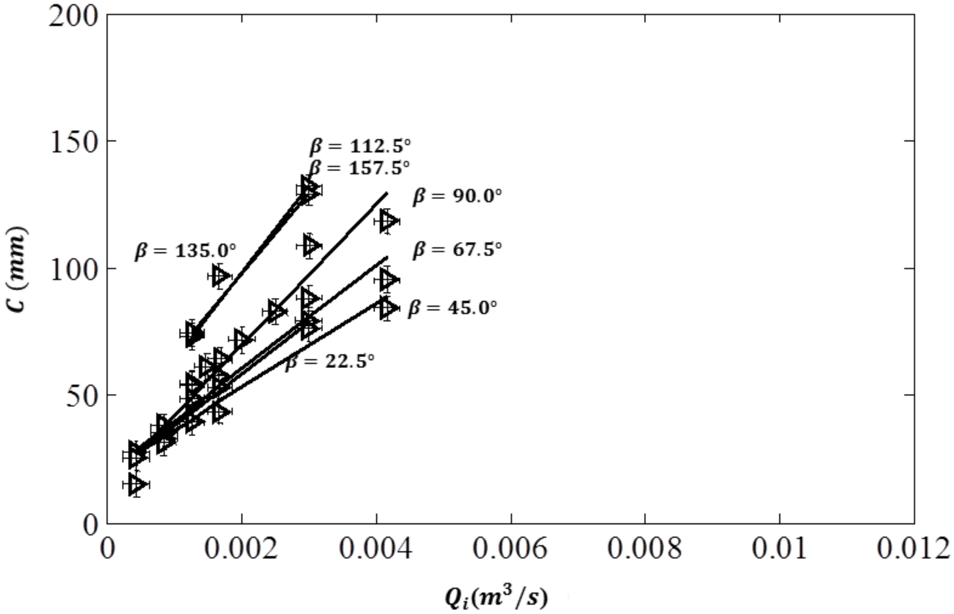

Figure 7.36 Chord length of the leg (C) for different jet volume flow rate (Q_i) with varying injection angle (β) are compared. Diameter of injection hole (D_i) cross-flow speed (U_∞), and boundary layer profile (δ) are fixed; D_i~5.0mm, U_∞=2.0m/s, $\delta = \delta_2$

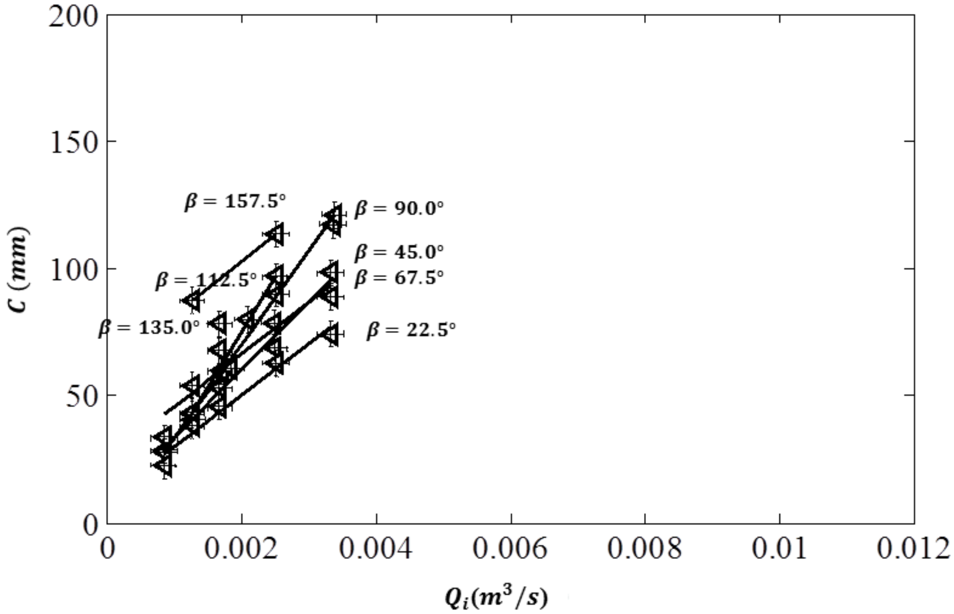

Figure 7.37 Chord length of the leg (C) for different jet volume flow rate (Q_i) with varying injection angle (β) are compared. Diameter of injection hole (D_i) cross-flow speed (U_∞), and boundary layer profile (δ) are fixed; D_i~5.0mm, U_∞=3.0m/s, $\delta = \delta_2$

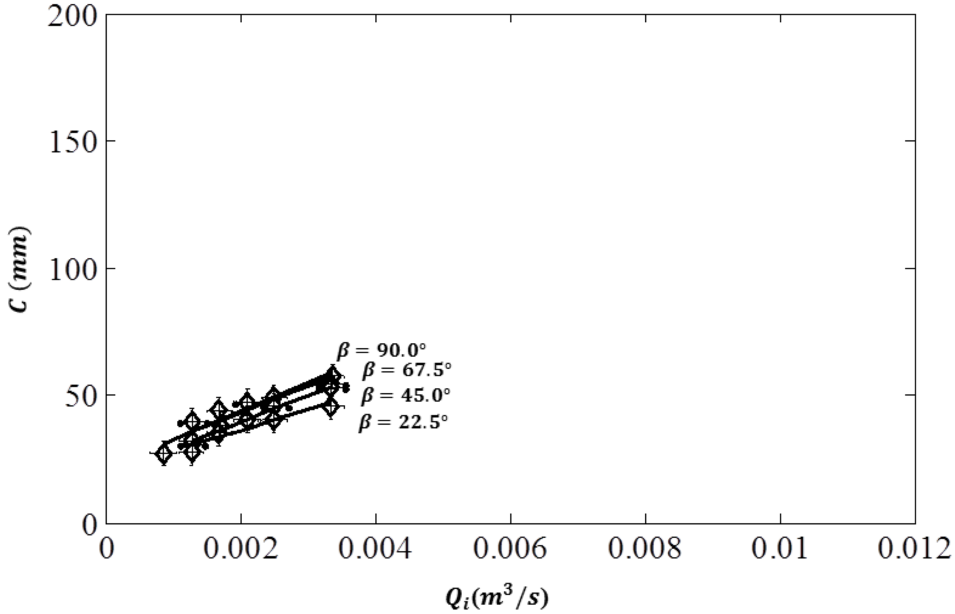

Figure 7.38 Chord length of the leg (C) for different jet volume flow rate (Q_i) with varying injection angle (β) are compared. Diameter of injection hole (D_i) cross-flow speed (U_∞), and boundary layer profile (δ) are fixed; D_i~5.0mm, U_∞=4.0m/s, $\delta = \delta_2$

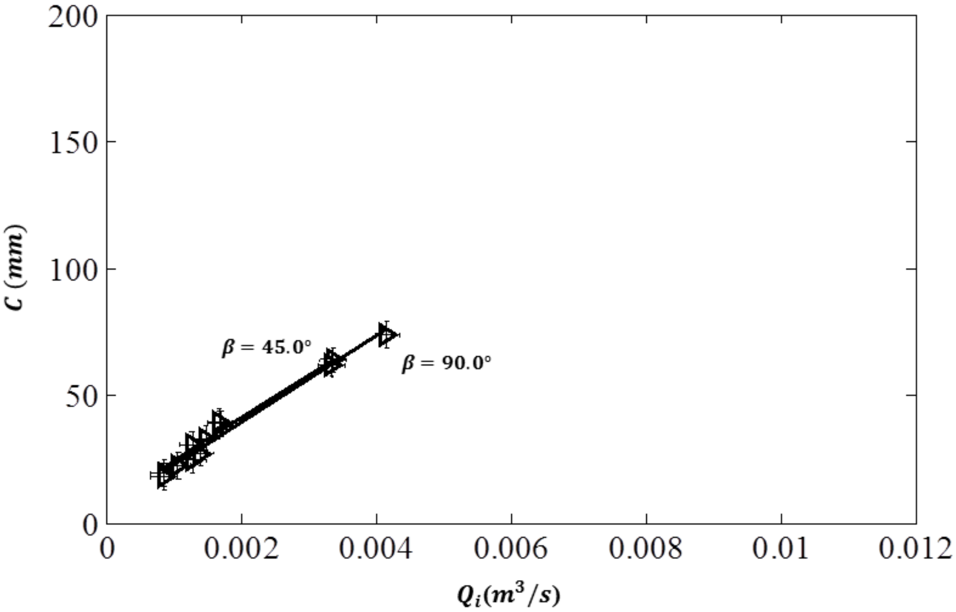

Figure 7.39 Chord length of the leg (C) for different jet volume flow rate (Q_i) with varying injection angle (β) are compared. Diameter of injection hole (D_i) cross-flow speed (U_∞), and boundary layer profile (δ) are fixed; D_i~10.0mm, U_∞=1.0m/s, $\delta = \delta_2$

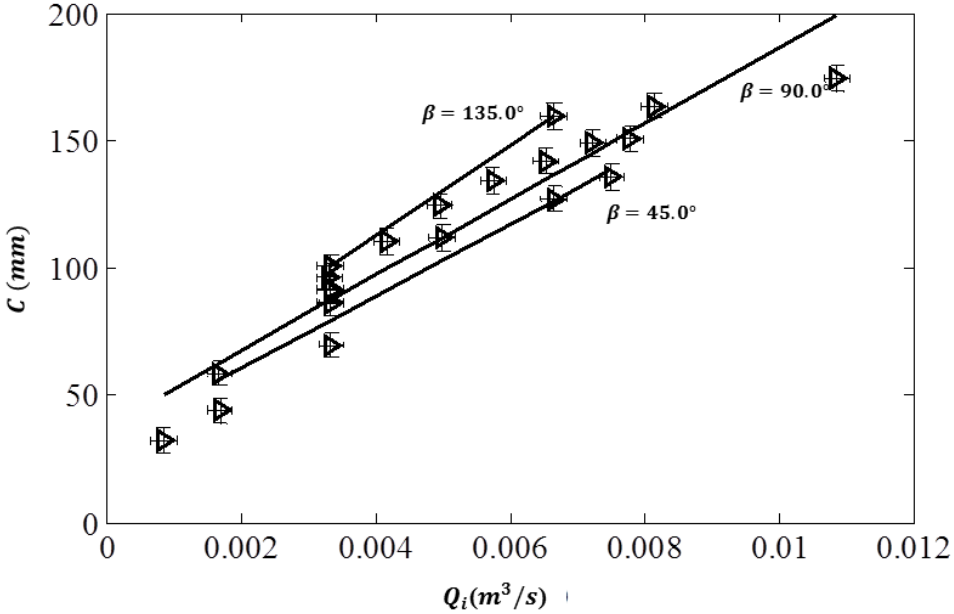

Figure 7.40 Chord length of the leg (C) for different jet volume flow rate (Q_i) with varying injection angle (β) are compared. Diameter of injection hole (D_i) cross-flow speed (U_∞), and boundary layer profile (δ) are fixed; D_i~10.0mm, U_∞=2.0m$/s$, $\delta = \delta_2$

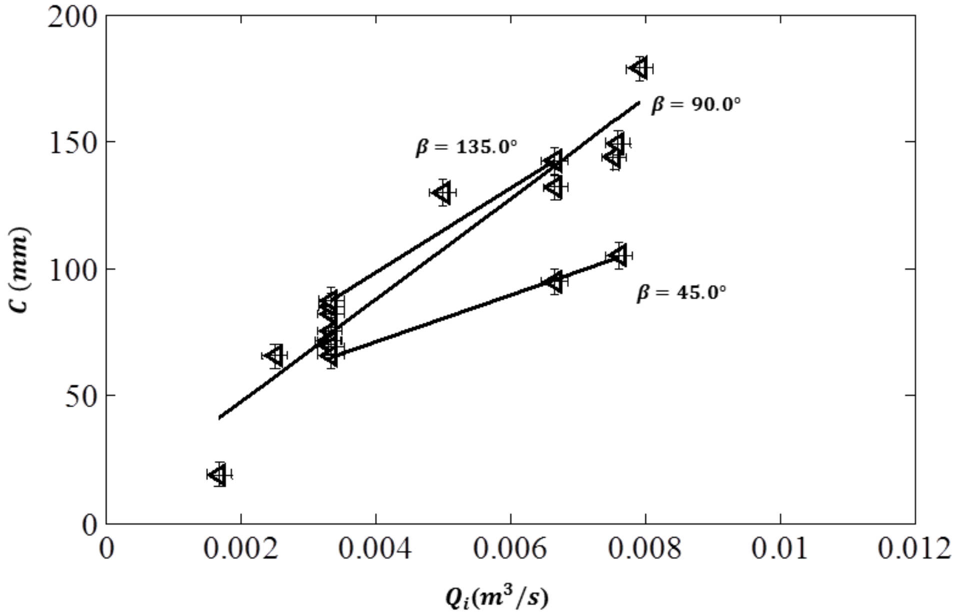

Figure 7.41 Chord length of the leg (C) for different jet volume flow rate (Q_i) with varying injection angle (β) are compared. Diameter of injection hole (D_i) cross-flow speed (U_∞), and boundary layer profile (δ) are fixed; D_i~10.0mm, U_∞=3.0m$/s$, $\delta = \delta_2$

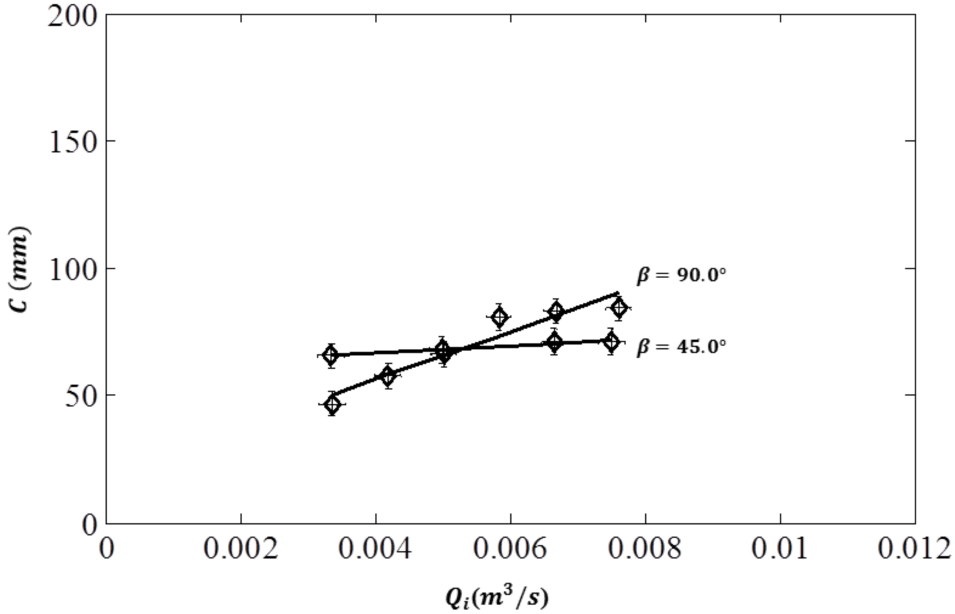

Figure 7.42 Chord length of the leg (C) for different jet volume flow rate (Q_i) with varying injection angle (β) are compared. Diameter of injection hole (D_i) cross-flow speed (U_∞), and boundary layer profile (δ) are fixed; D_i~10.0mm, U_∞=4.0$\frac{\text{m}}{s}$, $\delta = \delta_2$

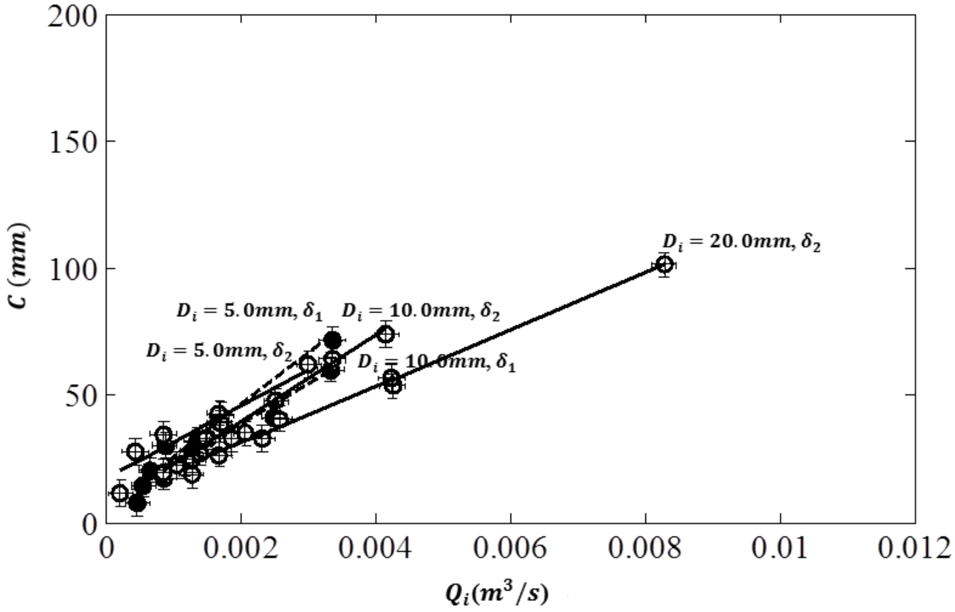

Figure 7.43 Chord length of the leg (C) for different jet volume flow rate (Q_i) with varying injection hole diameter (D_i), and boundary layer profiles (δ) are compared. Injection angle (β) and cross-flow speed (U_∞) are fixed; β=90.0mm and U_∞=1.0m$/s$.

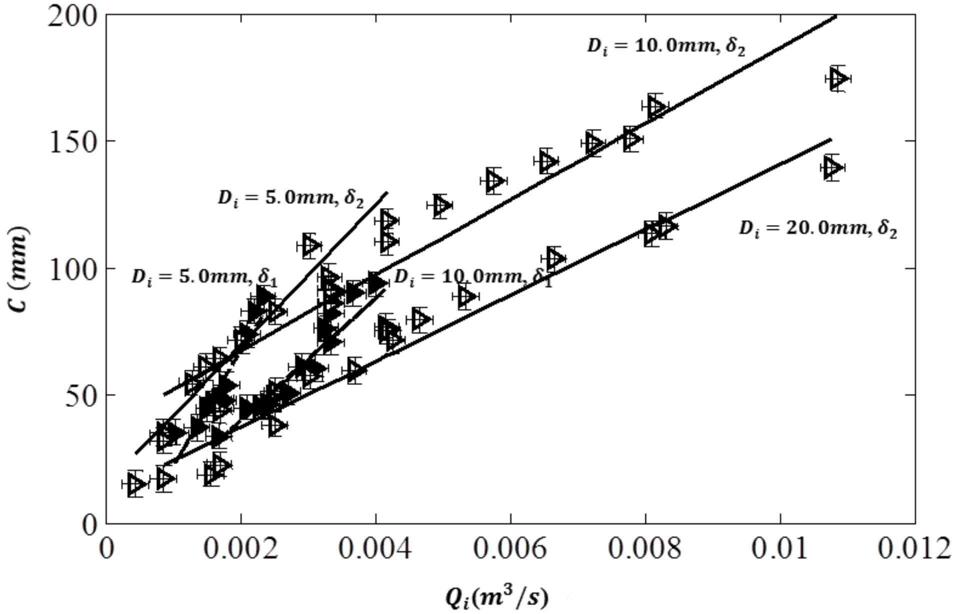

Figure 7.44 Chord length of the leg (C) for different jet volume flow rate (Q_i) with varying injection hole diameter (D_i), and boundary layer profiles (δ) are compared. Injection angle (β) and cross-flow speed (U_∞) are fixed; β=90.0mm and U_∞=2.0m/s.

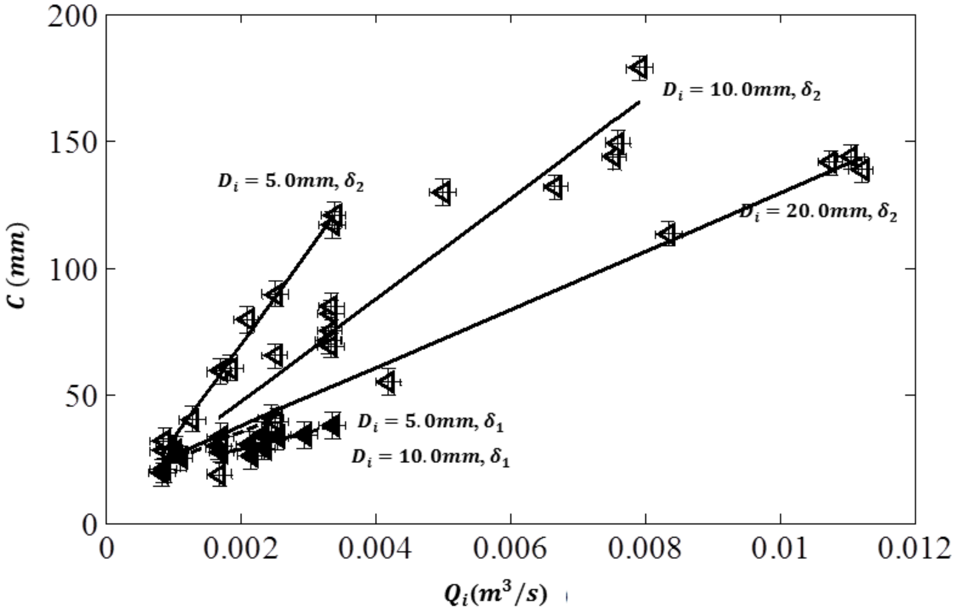

Figure 7.45 Chord length of the leg (C) for different jet volume flow rate (Q_i) with varying injection hole diameter (D_i), and boundary layer profiles (δ) are compared. Injection angle (β) and cross-flow speed (U_∞) are fixed; β=90.0mm and U_∞=3.0m/s.

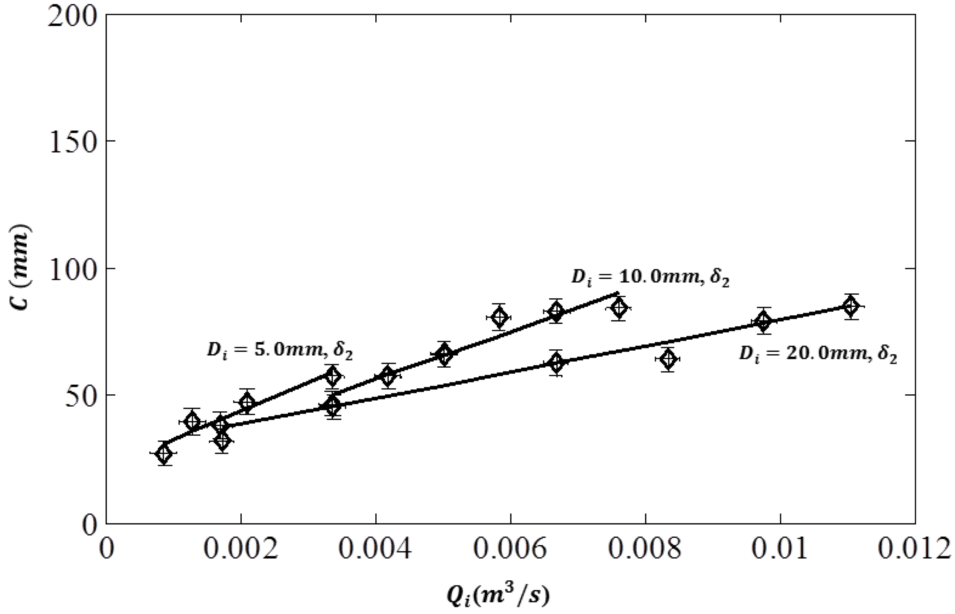

Figure 7.46 Chord length of the leg (C) for different jet volume flow rate (Q_i) with varying injection hole diameter (D_i), and boundary layer profiles (δ) are compared. Injection angle (β) and cross-flow speed(U_∞) are fixed; β=90.0mm and U_∞=4.0m$/s$.

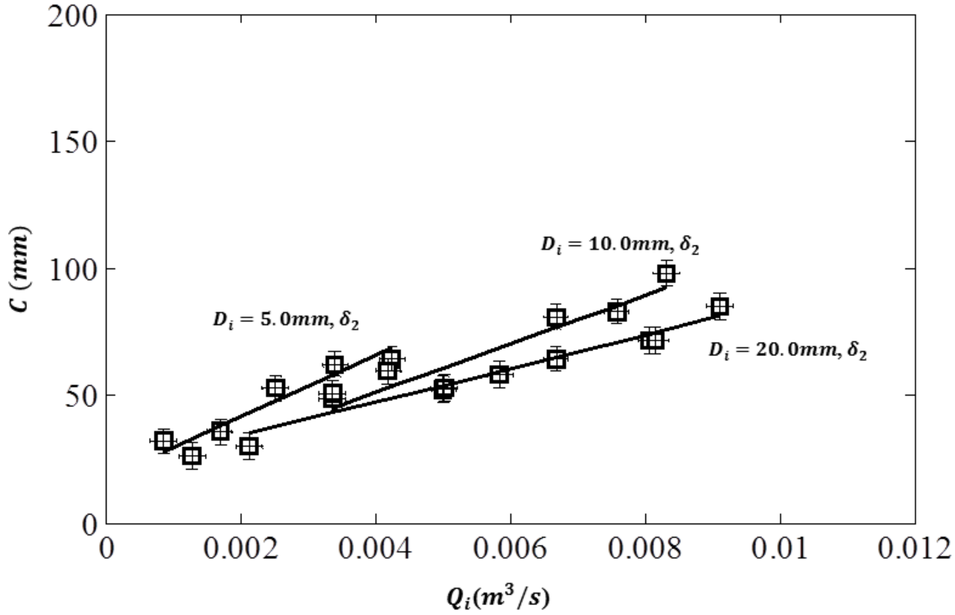

Figure 7.47 Chord length of the leg (C) with the jet volume flow rate (Q_i). Injection angle (β), cross-flow speed (U_∞), and boundary layer profile (δ) are fixed; β~90.0mm, U_∞=5.0m$/s$, $\delta = \delta_2$.

In summary, the cross-flow speed (U_∞), jet volume flow rate (Q_i), injection hole diameter (D_i), and boundary layer thickness (δ) are major parameters regarding the chord length (C). The role of the injection angle (β) is minor on chord length (C).

7.4 Equivalent diameter of deflected jet (D_E)

Size of the jet discharged from the injection hole is observed to be larger than size of the injection hole. The jet expands and forms ring shape flow consecutively. As presented in Figure 7.48, equivalent diameter (D_E) is the size of the gas semi-cylinder that forms after the injection hole. Uncertainty of the measurement occurs since sampling rate of the high speed cinematography is not small enough to capture the development of jet. In addition, focus issue occurs in case penetration depth of the jet is bigger than the depth of field. Considering both of the issue, uncertainty of the equivalent diameter (D_E) is $\pm 3\text{mm}$.

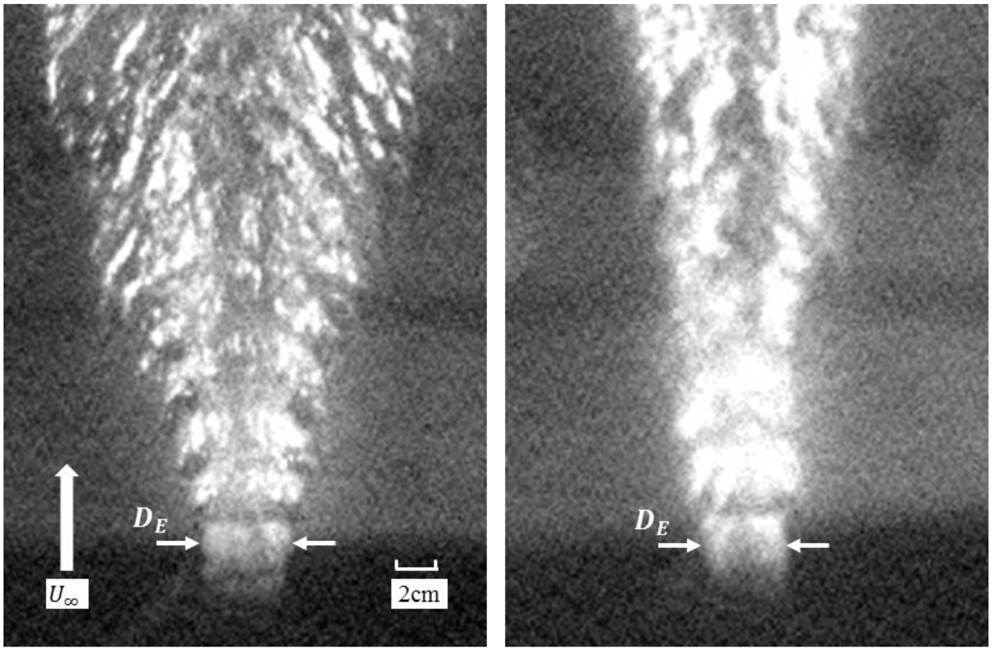

(a) **(b)**

Figure 7.48 Equivalent diameter of jet (D_E) is defined in the images of closer view on the jet in the vicinity of injection hole.. Conditions of each case are (a) D_i~10.0mm, β =90.0°, U_∞=2.5m$/s$, Q_i=6.7E-3m^3/s and (b) D_i ~10.0mm, β =90.0°, U_∞=4.0m$/s$, Q_i=6.7E-3m^3/s.

In Figure 7.49 through Figure 7.52, D_E is compared for different cross-flow speed (U_∞), jet volume flow rate (Q_i), injection angle (β), and injection hole diameter (D_i).

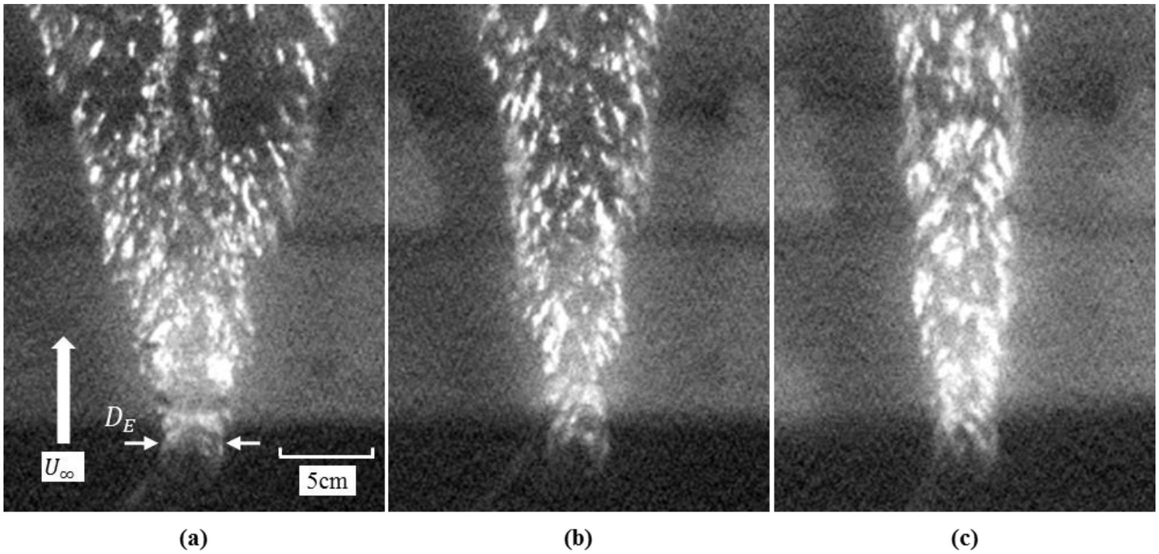

Figure 7.49 Comparison of Equivalent diameter (D_E) with changing U_∞; (a) U_∞=2.0m/s, (b) U_∞=3.0m/s, and (c) U_∞=4.0m/s. Other conditions are fixed; D_i~10.0mm, β =90.0°, and Q_i=3.4E-3m^3/s. Measured Chord lengths are (a) D_E =34.6mm, (b) D_E =30.6mm, and (c) D_E =27.9mm.

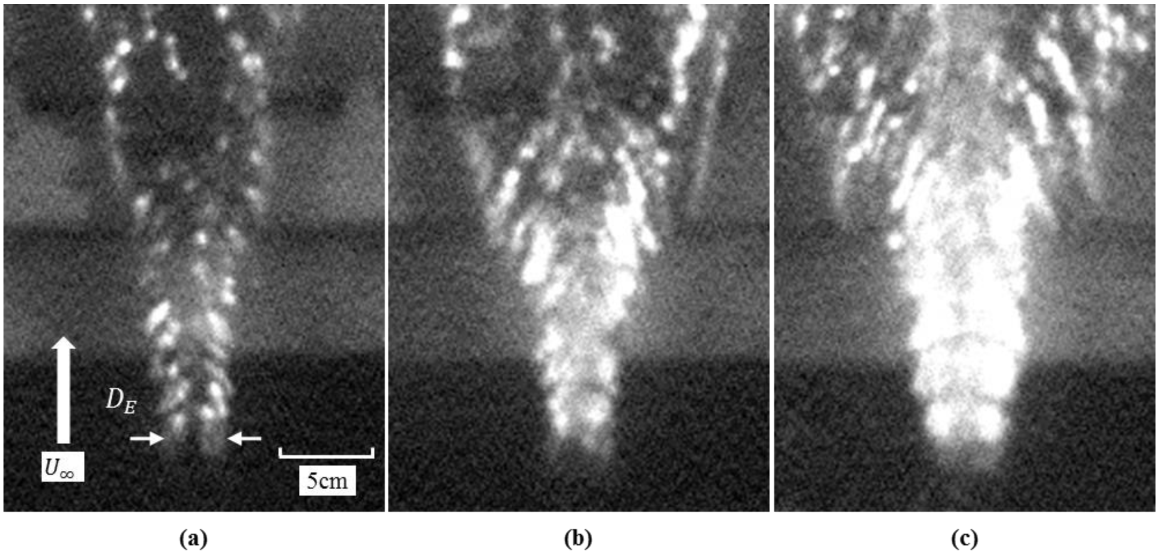

Figure 7.50 Comparison of Equivalent diameter (D_E) with changing Q_i; (a) Q_i=1.7E-3m^3/s, (b) Q_i=3.3E-3m^3/s, and (c) Q_i=6.5E-3m^3/s. Other conditions are fixed; D_i~10.0mm, β =90.0°, and U_∞=2.0m/s. Measured Chord lengths are (a) D_E =20.0mm, (b) D_E =33.3mm, and (c) D_E =40.0mm.

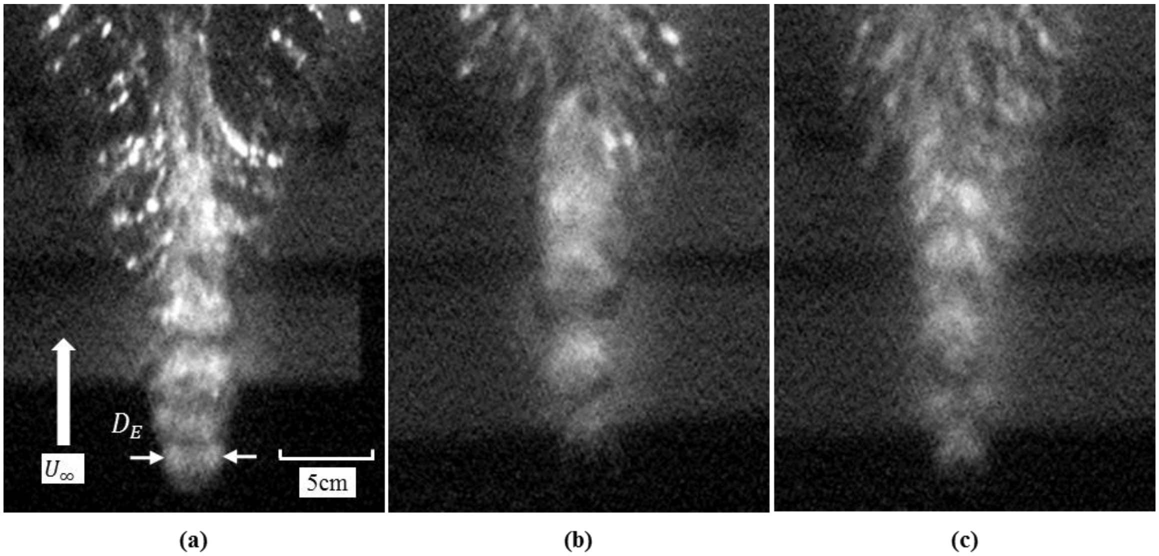

Figure 7.51 Comparison of Equivalent diameter (D_E) with changing β; (a) β =90.0°, (b) β =45.0°, and (c) β =22.5°. Other conditions are fixed; D_i~5.0mm, U_∞=2.0m/s, and Q_i=3.4E-3m^3/s. Measured Chord lengths are (a) D_E =32.0mm, (b) D_E =22.6mm, and (c) D_E =30.6mm.

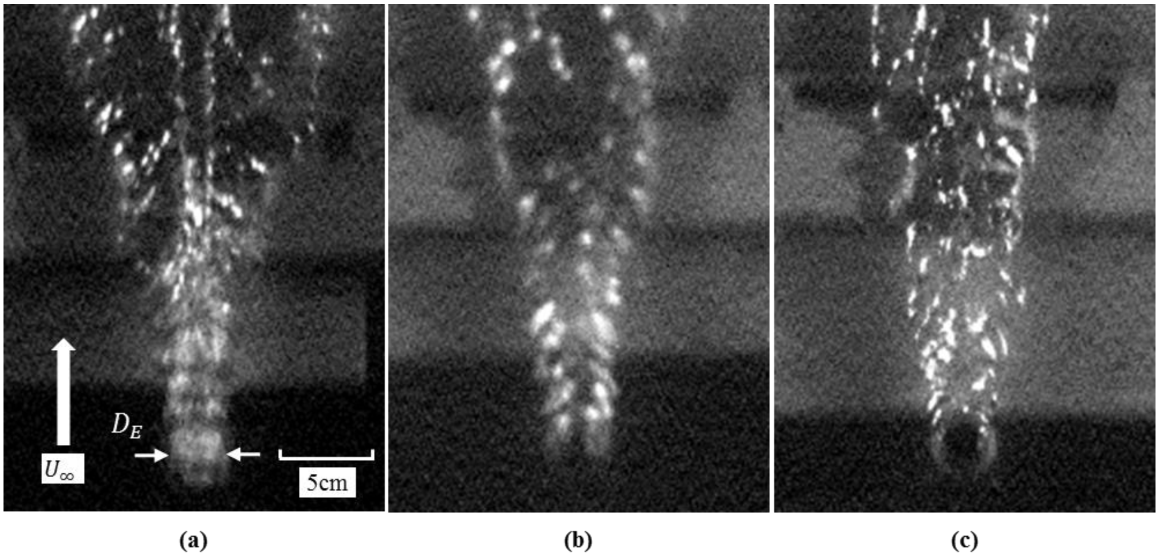

Figure 7.52 Comparison of Equivalent diameter (D_E) with changing D_i; (a) D_i~5.0mm, (b) D_i~10.0mm, and (c) D_i~20.0mm. Other conditions are fixed; β =90.0°, U_∞=2.0m/s, and Q_i=1.7E-3m^3/s. Measured Chord lengths are (a) D_E =19.1mm, (b) D_E =20.0mm, and (c) D_E =33.3mm.

Figure 7.53 through Figure 7.68 present plots of equivalent diameter (D_E) by varying cross-flow speed (U_∞), jet volume flow rate (Q_i), injection angle (β), and injection hole diameter (D_i). Throughout the plots, marker type represents cross-flow speed, ○U_∞=1.0m$/s$, ▷U_∞=2.0m$/s$, ◁U_∞=3.0m$/s$, ◇U_∞=4.0m$/s$, and □U_∞=5.0m$/s$. Solid markers (●)/dashed lines represent data from Barge model I, δ_1, and hollow markers (○)/solid lines represent data from Barge model II, δ_2.

Equivalent diameter of the jet (D_E) is plotted for different jet volume flow rates (Q_i) with varying cross-flow speed (U_∞) and boundary layer thickness (δ) are compared in Figure 7.53 through Figure 7.55. The magnitude of equivalent diameter (D_E) changes significantly by varying boundary layer thickness (δ). Unlike the sweep angle (φ) and chord length (C), the cross-flow speed (U_∞) does not take a significant role on the topology near-field, equivalent diameter (D_E).

The equivalent diameter (D_E) for different jet volume flow rate (Q_i) with varying injection angle (β) are compared in Figure 7.56 through Figure 7.63. Though the equivalent diameter (D_E) increases by increasing injection angle (β), its change is not significant. Figure 7.64 through Figure 7.68 presents comparison of the equivalent diameter (D_E) for different jet volume flow rates (Q_i) with varying injection hole diameter (D_i).

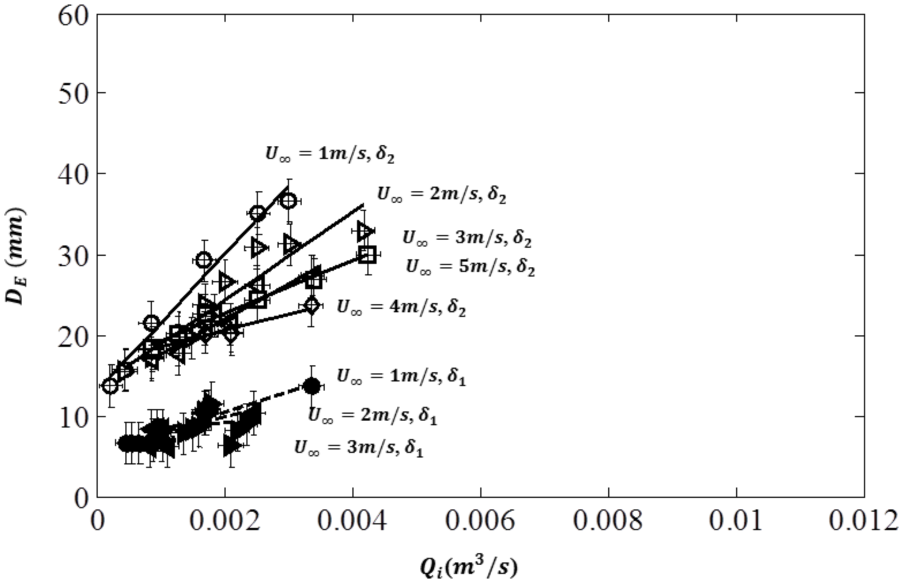

Figure 7.53 Equivalent diameter of jet (D_E) for different jet volume flow rate (Q_i) with varying cross-flow speed (U_∞) and boundary layer profile (δ) are compared. Diameter of injection hole (D_i) and injection angle (β) are fixed; D_i~5.0mm, β=90.0°.

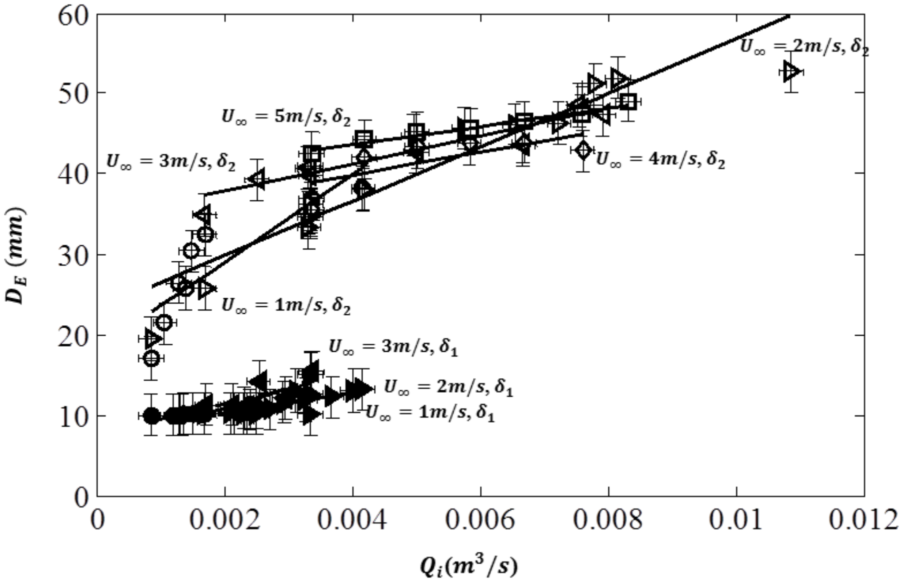

Figure 7.54 Equivalent diameter of jet (D_E) for different jet volume flow rate (Q_i) with varying cross-flow speed (U_∞) and boundary layer profile (δ) are compared. Diameter of injection hole (D_i) and injection angle (β) are fixed; D_i~10.0mm, β=90.0°.

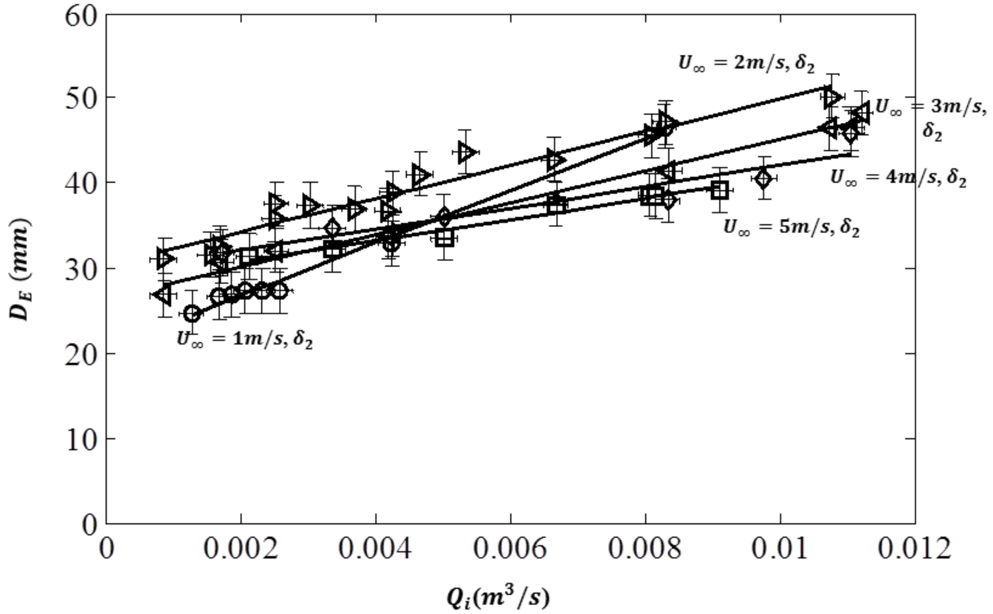

Figure 7.55 Equivalent diameter of jet (D_E) for different jet volume flow rate (Q_i) with varying cross-flow speed (U_∞) and boundary layer profile (δ) are compared. Diameter of injection hole (D_i) and injection angle (β) are fixed; D_i~20.0mm, β=90.0°.

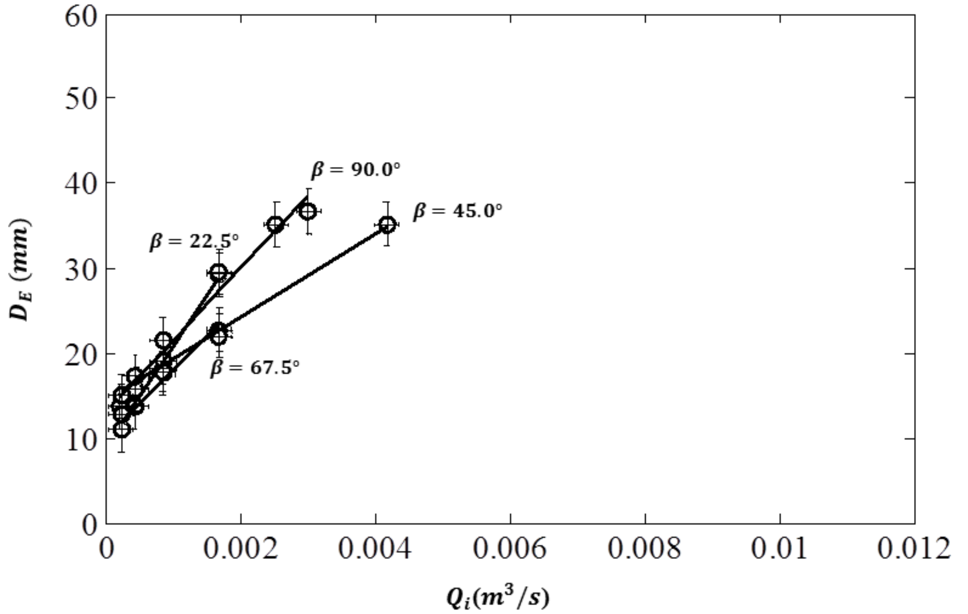

Figure 7.56 Equivalent diameter of jet (D_E) for different jet volume flow rate (Q_i) with varying injection angle (β) are compared. Diameter of injection hole (D_i) cross-flow speed (U_∞), and boundary layer profile (δ) are fixed; D_i~5.0mm, U_∞=1.0m/s, $\delta = \delta_2$

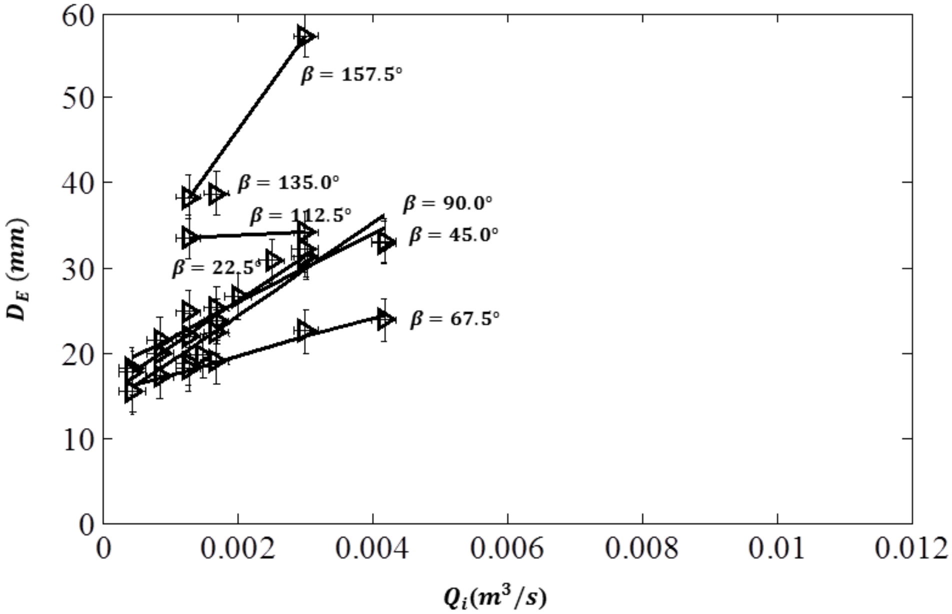

Figure 7.57 Equivalent diameter of jet (D_E) for different jet volume flow rate (Q_i) with varying injection angle (β) are compared. Diameter of injection hole (D_i) cross-flow speed (U_∞), and boundary layer profile (δ) are fixed; D_i~5.0mm, U_∞=2.0m/s, $\delta = \delta_2$

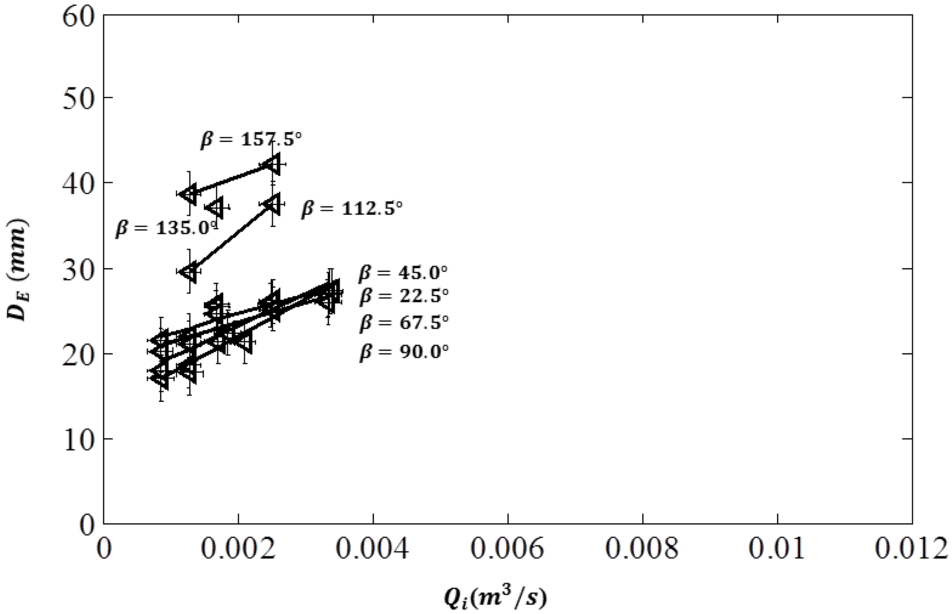

Figure 7.58 Equivalent diameter of jet (D_E) for different jet volume flow rate (Q_i) with varying injection angle (β) are compared. Diameter of injection hole (D_i) cross-flow speed (U_∞), and boundary layer profile (δ) are fixed; D_i~5.0mm, U_∞=3.0m/s, $\delta = \delta_2$

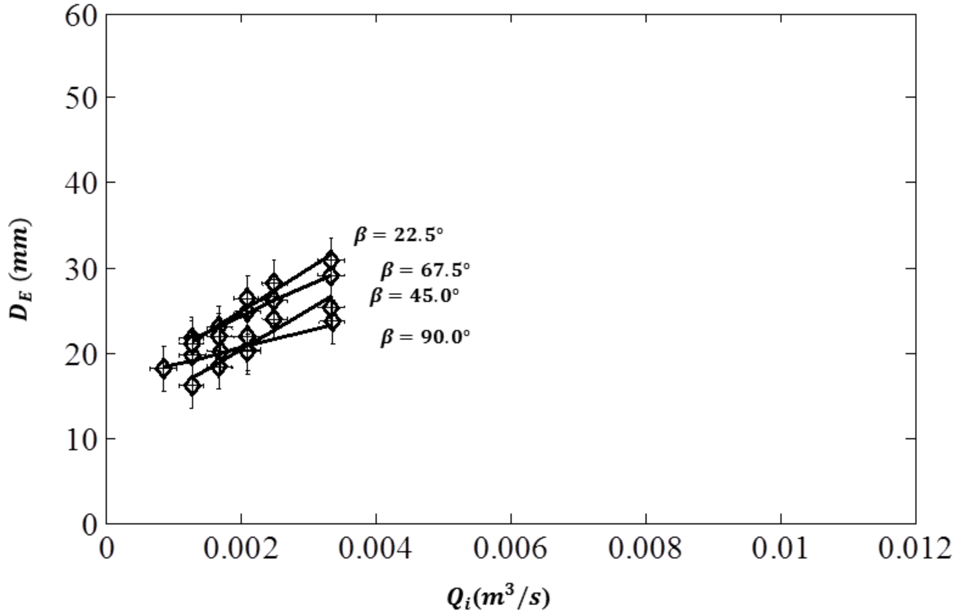

Figure 7.59 Equivalent diameter of jet (D_E) for different jet volume flow rate (Q_i) with varying injection angle (β) are compared. Diameter of injection hole (D_i) cross-flow speed (U_∞), and boundary layer profile (δ) are fixed; D_i~5.0mm, U_∞=4.0m/s, $\delta = \delta_2$

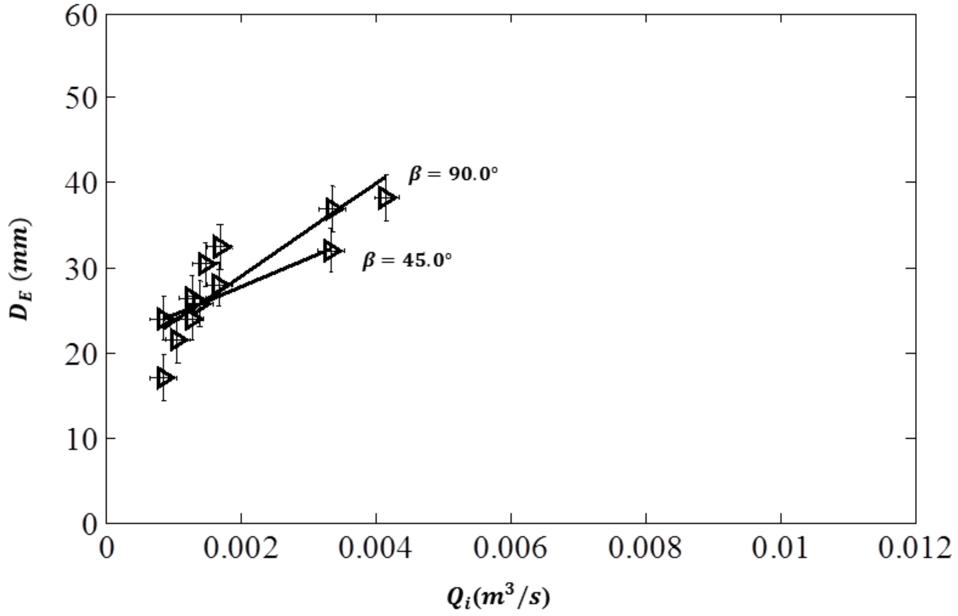

Figure 7.60 Equivalent diameter of jet (D_E) for different jet volume flow rate (Q_i) with varying injection angle (β) are compared. Diameter of injection hole (D_i) cross-flow speed (U_∞), and boundary layer profile (δ) are fixed; D_i~10.0mm, U_∞=1.0m/s, $\delta = \delta_2$

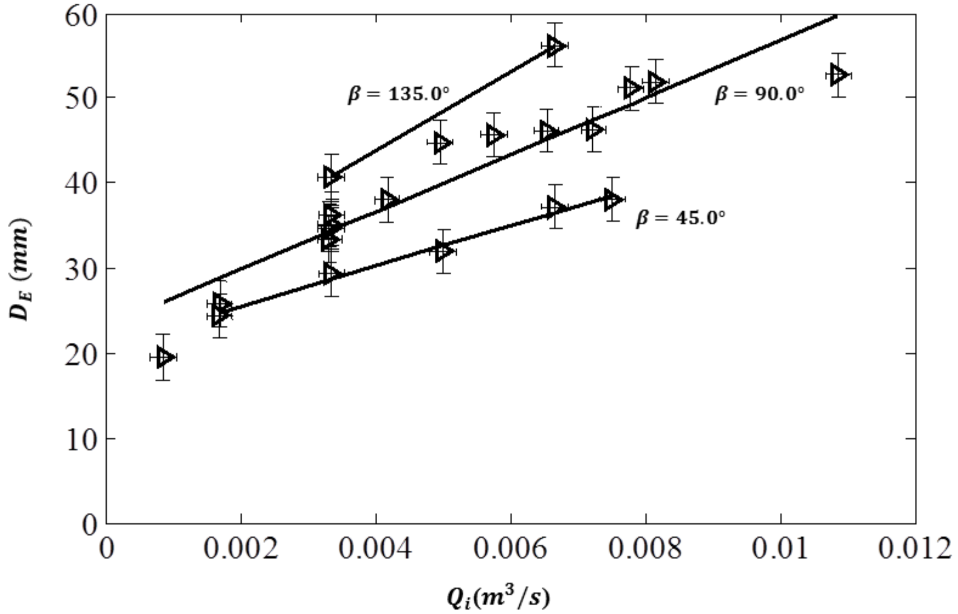

Figure 7.61 Equivalent diameter of jet (D_E) for different jet volume flow rate (Q_i) with varying injection angle (β) are compared. Diameter of injection hole (D_i) cross-flow speed (U_∞), and boundary layer profile (δ) are fixed; D_i~10.0mm, U_∞=2.0m$/s$, $\delta = \delta_2$

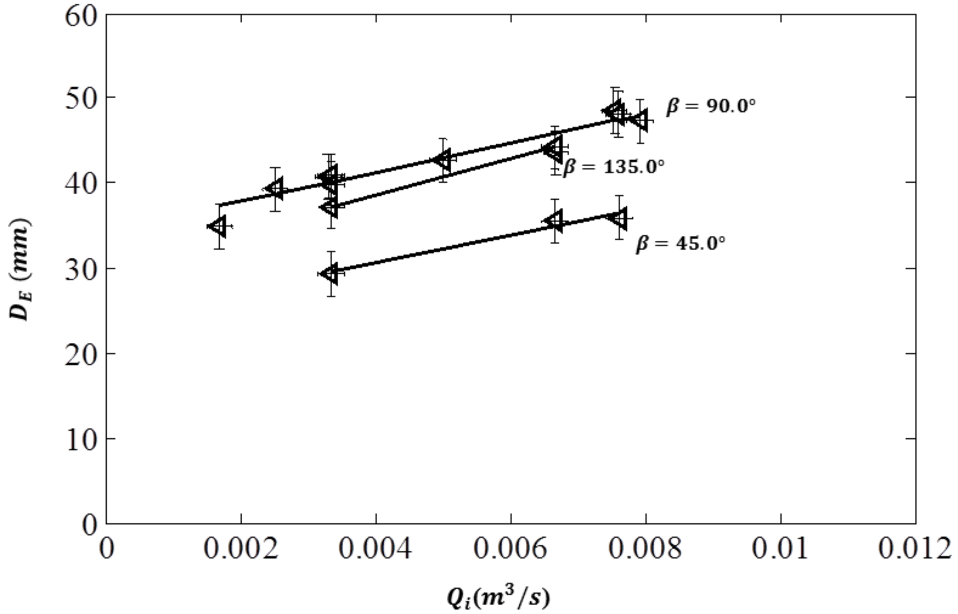

Figure 7.62 Equivalent diameter of jet (D_E) for different jet volume flow rate (Q_i) with varying injection angle (β) are compared. Diameter of injection hole (D_i) cross-flow speed (U_∞), and boundary layer profile (δ) are fixed; D_i~10.0mm, U_∞=3.0m$/s$, $\delta = \delta_2$

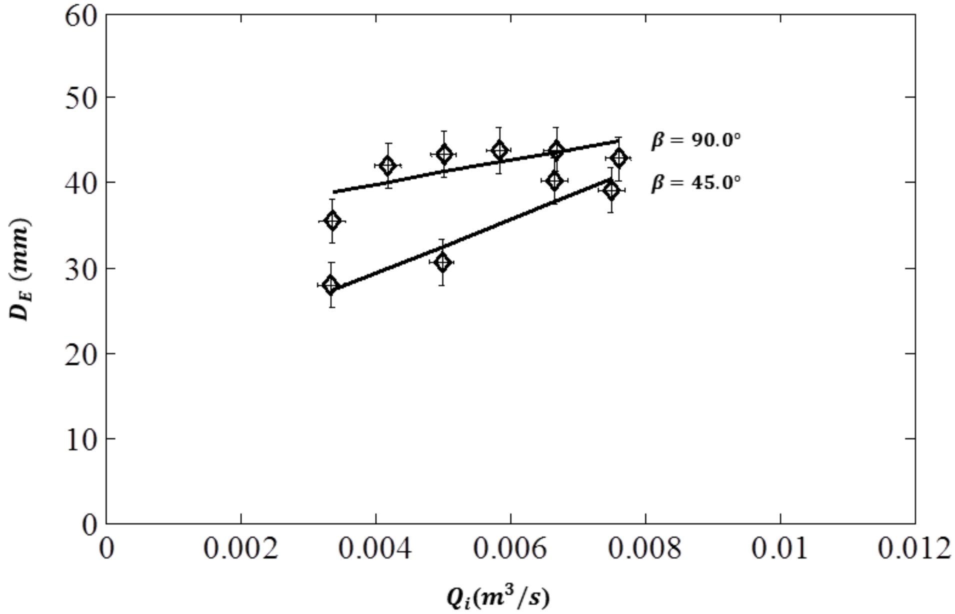

Figure 7.63 Equivalent diameter of jet (D_E) for different jet volume flow rate (Q_i) with varying injection angle (β) are compared. Diameter of injection hole (D_i) cross-flow speed (U_∞), and boundary layer profile (δ) are fixed; D_i~10.0mm, U_∞=4.0m/s, $\delta = \delta_2$

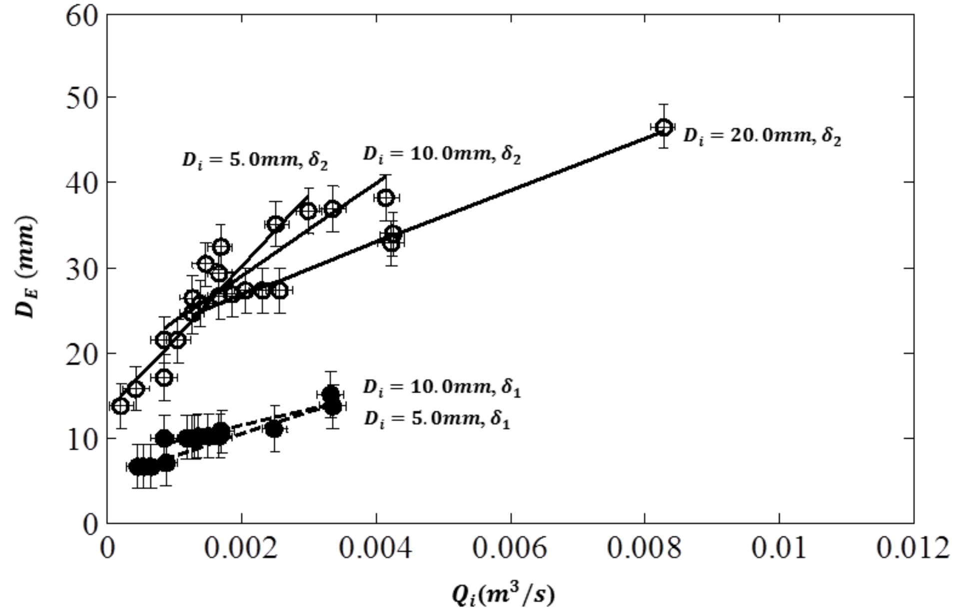

Figure 7.64 Equivalent diameter of jet (D_E) for different jet volume flow rate (Q_i) with varying injection hole diameter (D_i), and boundary layer profiles (δ) are compared. Injection angle (β) and cross-flow speed (U_∞) are fixed; β=90.0mm and U_∞=1.0m/s.

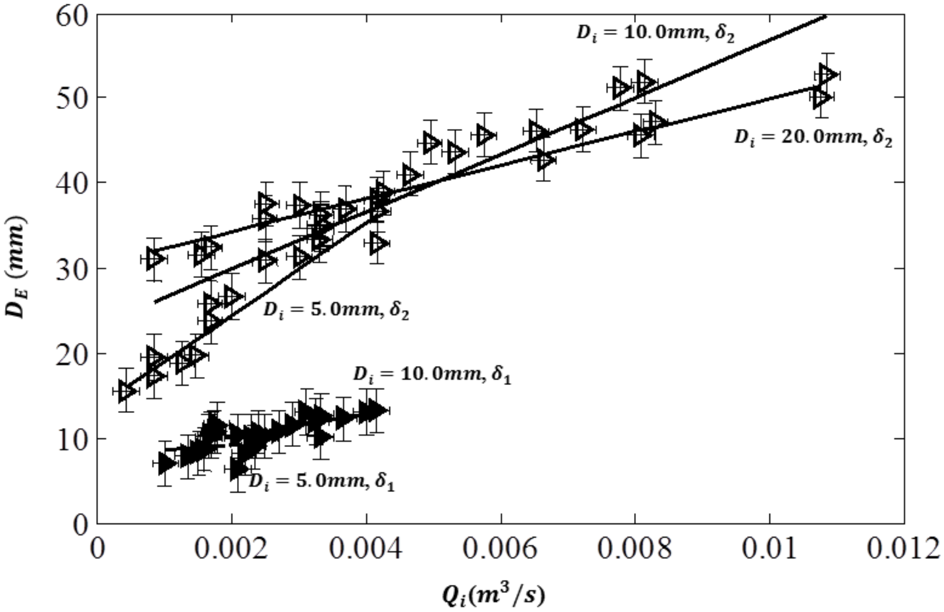

Figure 7.65 Equivalent diameter of jet (D_E) for different jet volume flow rate (Q_i) with varying injection hole diameter (D_i), and boundary layer profiles (δ) are compared. Injection angle (β) and cross-flow speed (U_∞) are fixed; β=90.0mm and U_∞=2.0m/s.

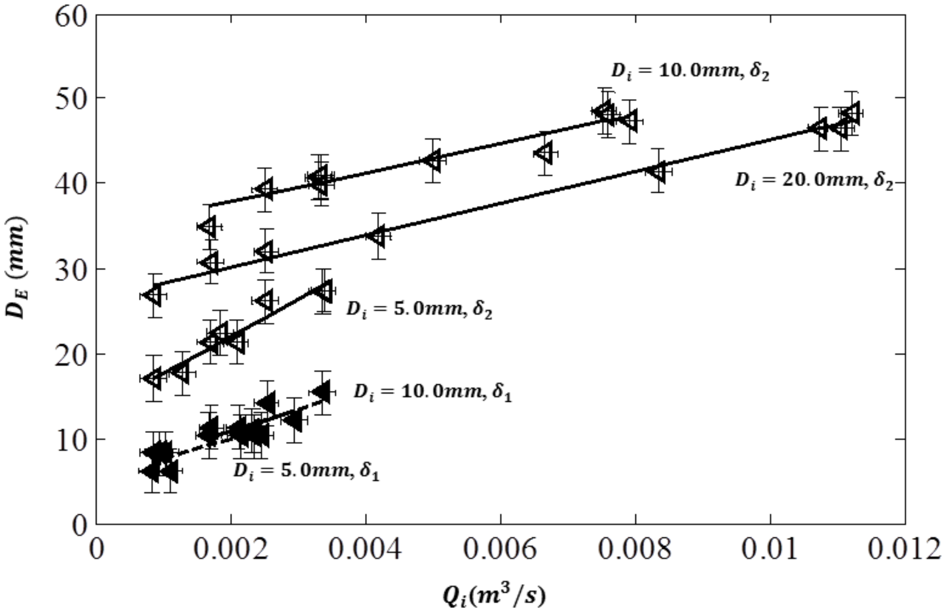

Figure 7.66 Equivalent diameter of jet (D_E) for different jet volume flow rate (Q_i) with varying injection hole diameter (D_i), and boundary layer profiles (δ) are compared. Injection angle (β) and cross-flow speed (U_∞) are fixed; β=90.0mm and U_∞=3.0m/s.

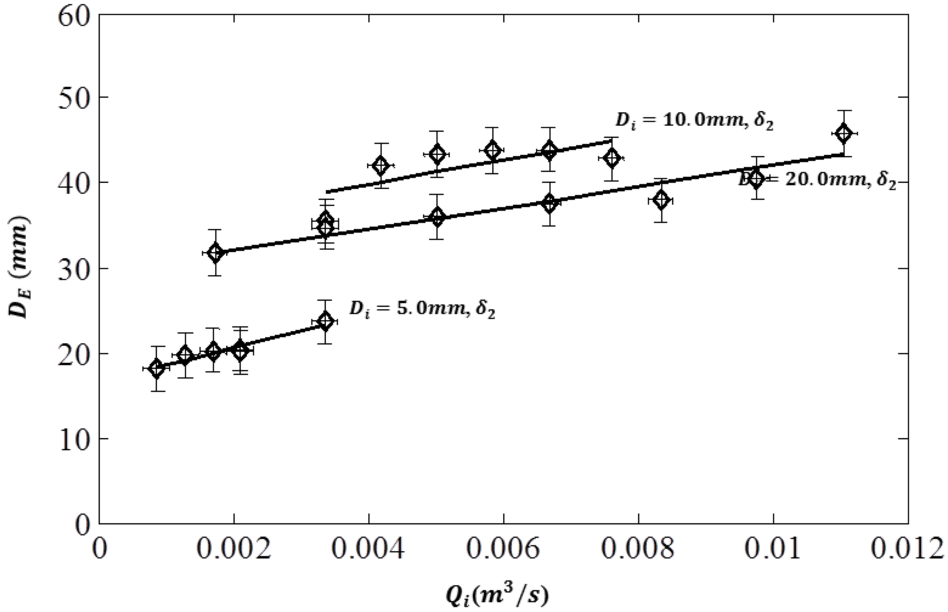

Figure 7.67 Equivalent diameter of jet (D_E) for different jet volume flow rate (Q_i) with varying injection hole diameter (D_i), and boundary layer profiles (δ) are compared. Injection angle (β) and cross-flow speed (U_∞) are fixed; β=90.0mm and U_∞=4.0m/s.

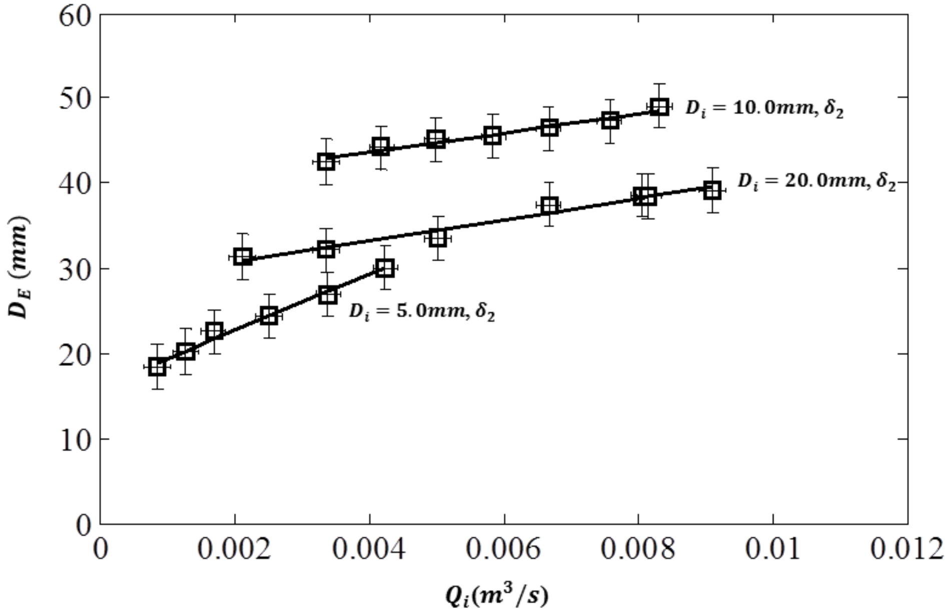

Figure 7.68 Equivalent diameter of jet (D_E) for different jet volume flow rate (Q_i) with varying injection hole diameter (D_i), and boundary layer profiles (δ) are compared. Injection angle (β) and cross-flow speed (U_∞) are fixed; β=90.0mm and U_∞=5.0m/s.

In summary, jet volume flow rate (Q_i), injection hole diameter (D_i), and boundary layer thickness (δ) are major parameters regarding the equivalent diameter (D_E). The role of the injection angle (β) is minor. Unlike far field properties, the cross-flow speed (U_∞) does not take a significant role on size of the jet in the near field of the injector.

7.5 Topology of the jet with low cross-flow speed

Observation of the jet topology show consistent trends except at the lowest cross flow speed examined. Figure 7.71 and Figure 7.72 compares the topologies by changing cross-flow speed (U_∞). Topologies of the resulting flow with higher cross-flow speeds ($U_\infty \geq 2\mathrm{m/s}$) have relatively straight legs, while those with lower speed ($U_\infty < 2\mathrm{m/s}$) have gas legs that are not straight and change in thickness along their length. A physical explanation will be discussed at chapter 9.

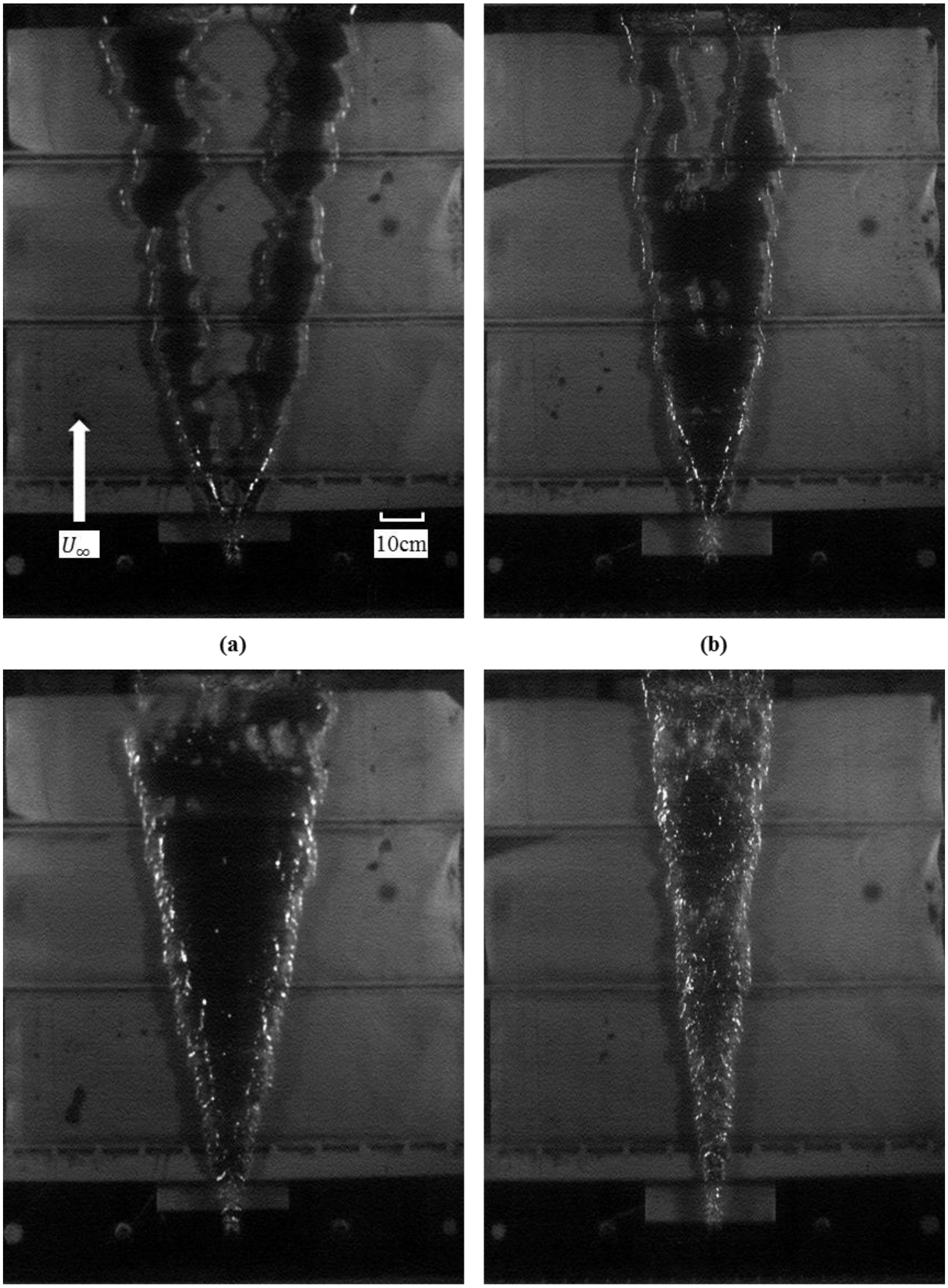

(a) **(b)**

(c) **(d)**

Figure 7.69 Images of different topologies of jet by changing cross-flow speed (U_∞). (a) U_∞=1.0m/s, (b) U_∞=1.5m/s, (c) U_∞=2.0m/s, and (d) U_∞=3.0m/s. Other conditions are fixed; D_i~10.0mm, β =90°, and Q_i =1.7E-3m^3/s.

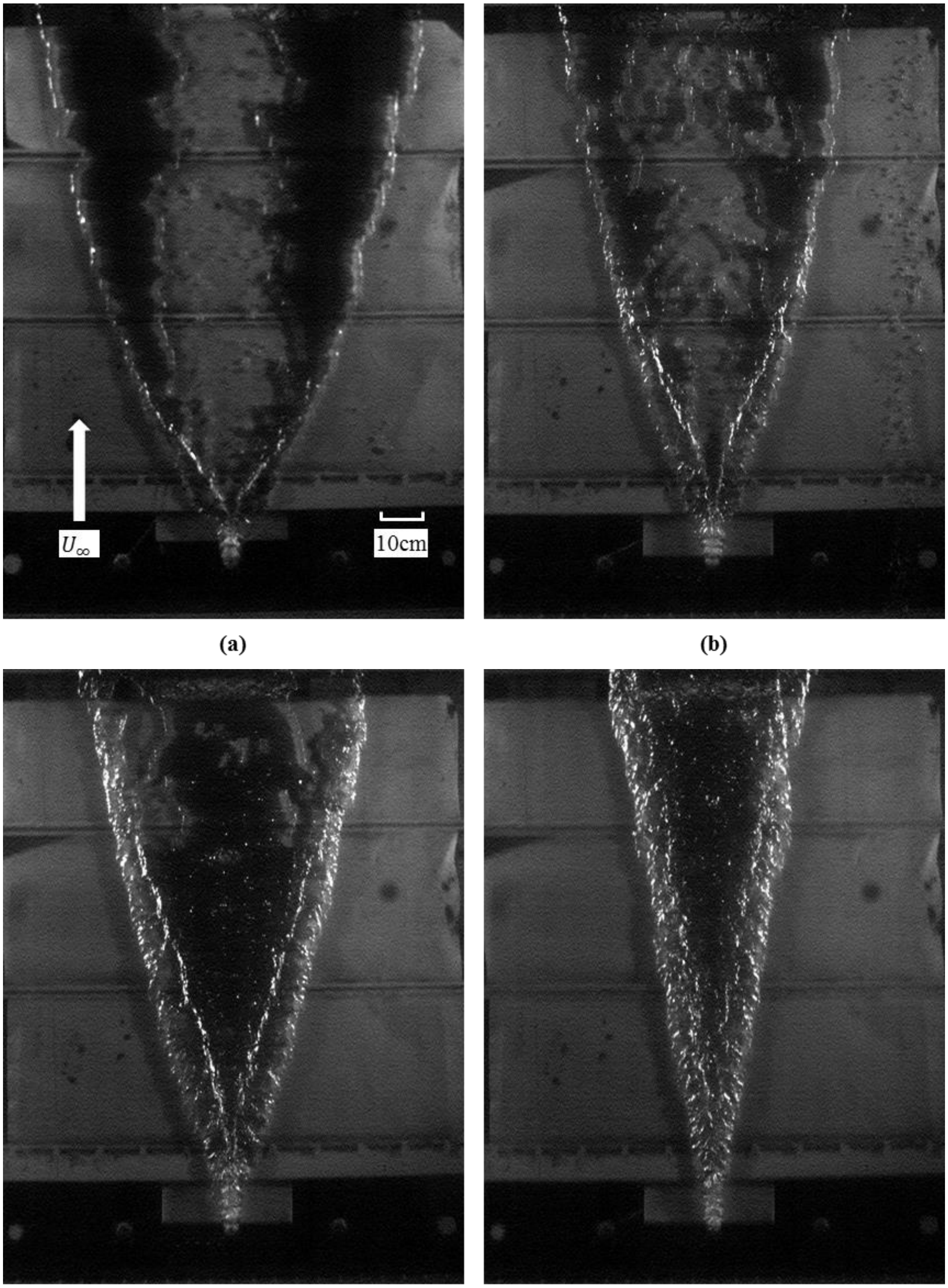

(a) (b)

(c) (d)

Figure 7.70 Images of different topologies of jet by changing cross-flow speed (U_∞). (a) U_∞=1.0m/s, (b) U_∞=1.5m/s, (c) U_∞=2.0m/s, and (d) U_∞=3.0m/s. Other conditions are fixed; D_i~10.0mm, β =90°, and Q_i =3.4E-3m^3/s.

7.6 Uncertainty and repeatability of measurements

Uncertainties of input variables, cross-flow speed (U_∞), jet volume flow rate (Q_i), boundary layer thickness (δ), and hydrostatic pressure (P_∞) are noted at Table 6.1. Uncertainties of measurement were noted in related sections in this chapter; sweep angle of the jet (φ) $\pm1.5°$, chord length of leg (C) ±5.0mm, and equivalent diameter of the jet (D_E) ±3.0mm.

For validating repeatability of the experiment, two cases were repeated six times. Table 7.2 presents the result of the repeated test. Deviations from the mean of each measurement are in the order of or less then uncertainties. Thus, data from the experiment in the setup are repeatable.

$D_i(mm)$	$\beta(°)$	$U_\infty(m/s)$	$Q_i(m^3/s)$	$\varphi(°)$	$\varphi - \varphi_{avg.}$	C(mm)	$C - C_{avg.}$	D_E(mm)	$D_E - D_{E,avg.}$
10	**90**	**2.0**	**3.3E-03**	**72.2**	**-0.3**	**86.1**	**-1.8**	**33.3**	**-0.2**
				72.5	**0.0**	**86.1**	**-1.8**	**34.6**	**1.1**
				72.9	**0.4**	**91.7**	**3.9**	**33.3**	**-0.2**
				72.5	**0.0**	**86.5**	**-1.4**	**33.3**	**-0.2**
				72.5	**0.0**	**90.8**	**2.9**	**33.3**	**-0.2**
				72.5	**0.0**	**86.2**	**-1.7**	**33.3**	**-0.2**
Average				$\varphi_{avg.}$=**72.5**		$C_{avg.}$=**87.9**		$D_{E,avg.}$=**33.5**	
10	**90**	**3.0**	**3.3E-03**	**80.0**	**0.3**	**71.6**	**-2.8**	**29.3**	**-0.2**
				79.4	**-0.3**	**75.4**	**1.0**	**26.6**	**-2.9**
				79.8	**0.1**	**71.6**	**-2.8**	**28.0**	**-1.6**
				79.6	**-0.1**	**69.7**	**-4.7**	**30.6**	**1.1**
				79.7	**-0.1**	**78.4**	**4.0**	**32.0**	**2.4**
				79.8	**0.1**	**79.8**	**5.4**	**30.6**	**1.1**
Average				$\varphi_{avg.}$=**79.7**		$C_{avg.}$=**74.4**		$D_{E,avg.}$=**29.5**	

Table 7.2 Summary of repeatability test

CHAPTER 8

Scaling of Interaction of Vertical Jet with Cross-flow beneath Horizontal Surface

Dimensional and non-dimensional analysis were performed on the characteristic dimensions of the gas pocket topology based on the results of the preceding chapter. Perpendicular component of sweep angle on the leg ($cos\varphi$), the ratio of the leg chord length and the boundary layer thickness (C/δ), and the ratio of the equivalent diameter of deflected jet to the diameter of injection hole (D_E/D_i) were analyzed. Figure 8.1 presents schematic drawing with analyzed parameters.

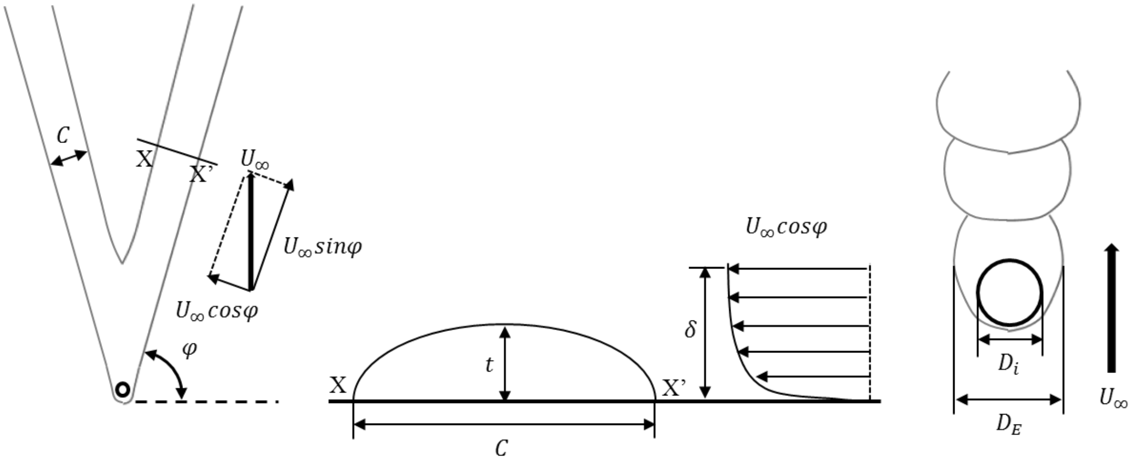

$\boldsymbol{cos\varphi}$ $\boldsymbol{C/\delta}$ $\boldsymbol{D_E/D_i}$

Figure 8.1 Schematic drawing describes parameters used on scaling. Left image is the bottom view of the resulting flow. Middle image is the cross section of the split leg(XX' plane on the left image). Right image is closer view around the injection hole.

Throughout this chapter, following markers are used to represent different flow conditions.

- Different symbols represent different types of the jet: △Delta type, ◇Transition type, ▽Lambda type
- Face color of the markers represents boundary layer profile(Barge model): ▲δ_1 (Barge model I) and △δ_2 (Barge model II)
- Size of the markers represent the diameter of the injection hole: △D_i=5.0mm, △D_i=10.0mm, and △D_i=20.0mm

Since behavior of resulting flow with $U_\infty = 1\mathrm{m/s}$ is differs significantly from those with a higher cross-flow speed, the dimensional and non-dimensional analysis were performed on data sets both with U_∞=1$\mathrm{m/s}$ and without U_∞=1$\mathrm{m/s}$ data.

8.1 Dimensional analysis

Dimensional analysis on perpendicular component of sweep angle ($cos\varphi$), the ratio of chord length of leg and boundary layer thickness (C/δ), and the ratio of equivalent diameter and injection hole diameter (D_E/D_i) were performed to gain better understanding on how these variables changes with respect to the independent flow parameters. The independent parameters considered were the jet speed at the exit of the injection hole (U_i), the cross-flow speed (U_∞), the vertical component of injection angle (sinβ), the diameter of the injection hole (D_i), and the boundary layer thickness (δ). Since the jet speed (U_i) is product of jet volume flow rate (Q_i) and injection hole diameter (D_i), $U_i = Q_i/\left(\frac{\pi}{4}{D_i}^2\right)$, one of either the jet speed (U_i) or jet volume flow rate (Q_i) can be used with injection hole diameter (D_i) but not all three together. In this dimensional analysis, the jet speed (U_i) is used instead of jet volume flow rate (Q_i) with injection hole diameter (D_i).

Dimensional analysis on the perpendicular component on the leg of sweep angle (cosφ) is presented in Figure 8.2, data with U_∞=1m/s, and Figure 8.3, data without U_∞=1m/s. The data set without U_∞=1m/s shows a better line fit, but the overall trend does not change much. Outliers on Figure 8.2 are cases with low cross-flow speed (U_∞=1m/s), small injection hole diameter (D_i=5mm), and a relatively high jet speed (U_i). As stated above, the influence of cross-flow speed (U_∞), jet speed (U_i), and injection hole diameter (D_i) is significant on sweep angle (φ). While the injection angle ($sin\beta$) and boundary layer thickness (δ) are not as significant. This suggests that the detailed flow around the jet injection location does not strongly influence the flow in the legs.

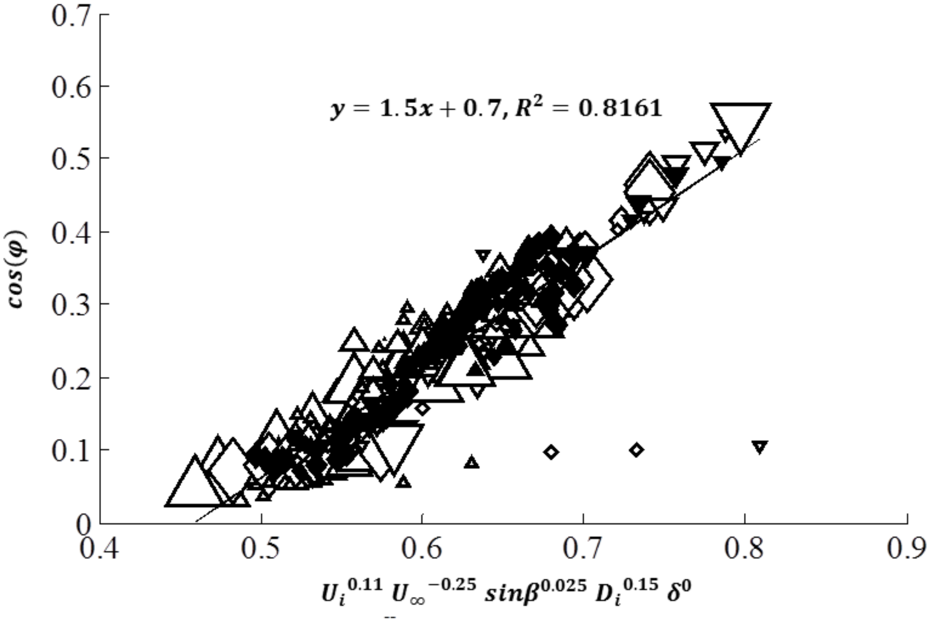

Figure 8.2 Dimensional analysis on perpendicular component of sweep angle ($cos\varphi$) with independent input variables, Jet speed (U_i), cross-flow speed (U_∞), vertical component of injection angle ($sin\beta$), injection hole diameter (D_i), boundary layer thickness (δ).

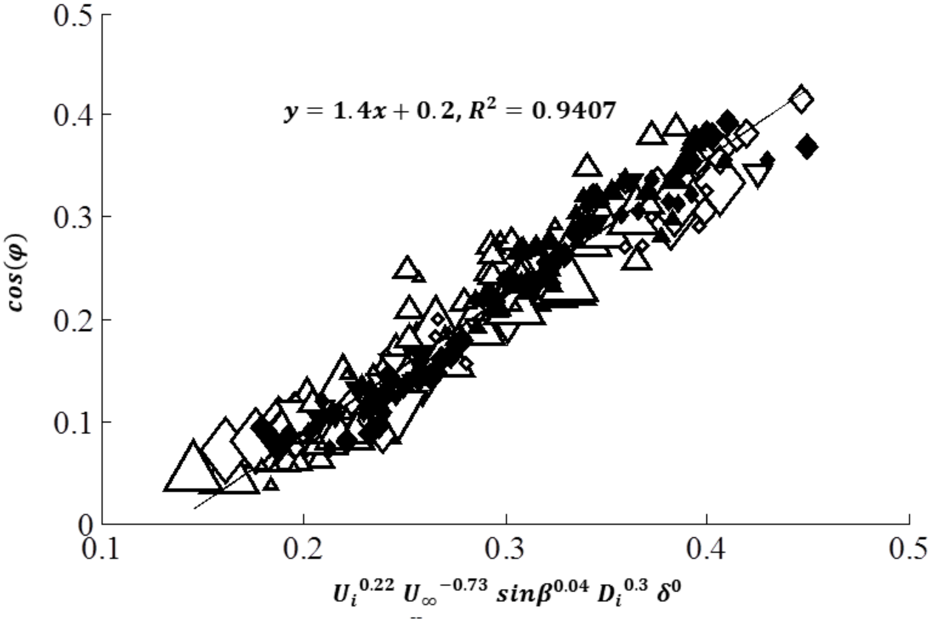

Figure 8.3 Dimensional analysis on perpendicular component of sweep angle ($cos\varphi$) with independent input variables, Jet speed (U_i), cross-flow speed (U_∞), vertical component of injection angle ($sin\beta$), injection hole diameter (D_i), boundary layer thickness (δ). Data with U_∞ =1m/s are excluded.

Dimensional analysis on ratio of chord length of leg and boundary layer thickness(C/δ) is presented in Figure 8.4, data with U_∞=1m/s, and Figure 8.5, data without U_∞=1m/s. The data set without U_∞=1m/s shows a better fit, but the overall trend does not change much. As it is observed earlier in chapter, influence of cross-flow speed (U_∞), jet speed (U_i), injection hole diameter (D_i), and boundary layer thickness (δ) is significant on chord length (C), while the injection angle ($sin\beta$) is not. Here again, the way how air is being injected does not appear take a significant role on formation of the gas legs.

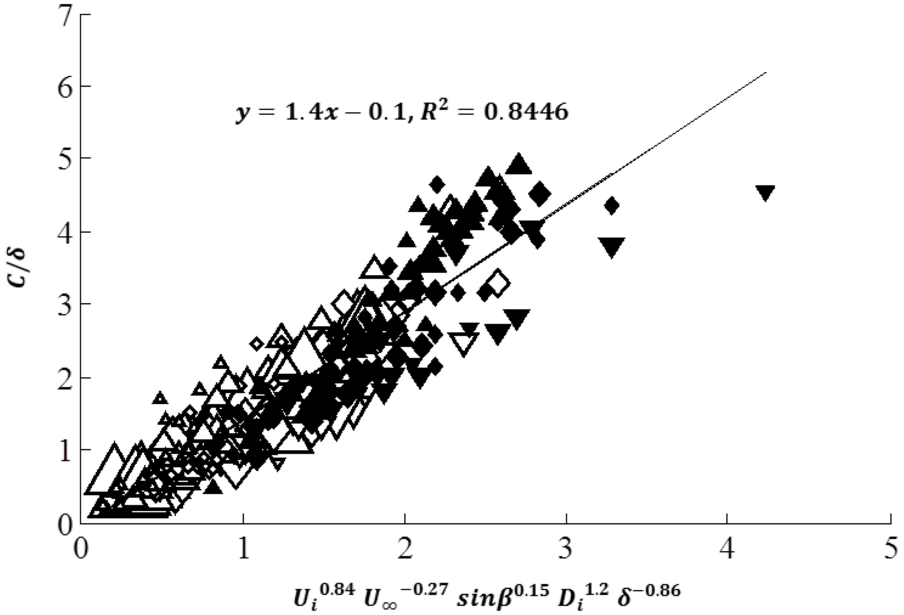

Figure 8.4 Dimensional analysis on ratio of chord length of the leg and boundary layer thickness (C/δ) with independent input variables, Jet speed (U_i), cross-flow speed (U_∞), vertical component of injection angle ($sin\beta$), injection hole diameter (D_i), boundary layer thickness (δ).

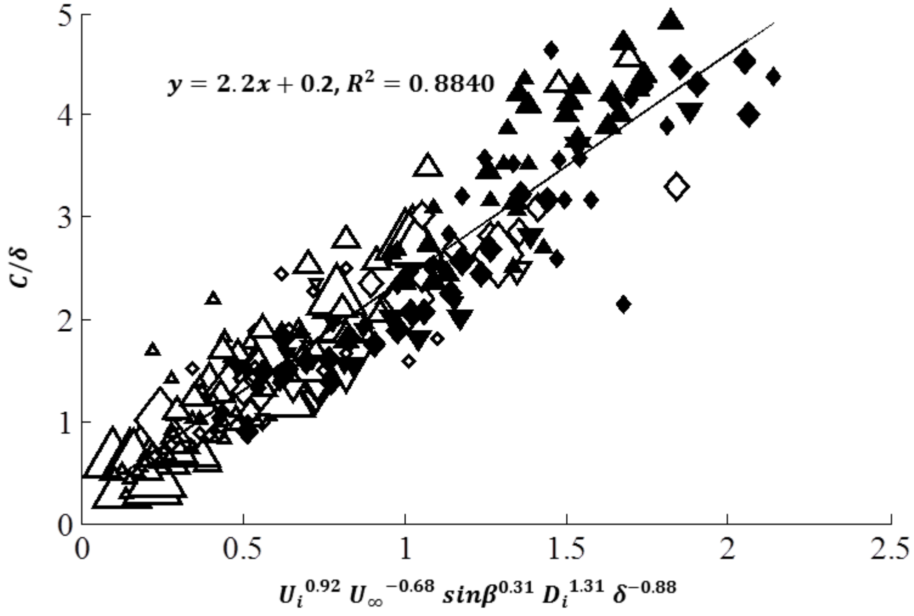

Figure 8.5 Dimensional analysis on ratio of chord length of the leg and boundary layer thickness (C/δ) with independent input variables, Jet speed (U_i), cross-flow speed (U_∞), vertical component of injection angle ($sin\beta$), injection hole diameter (D_i), boundary layer thickness (δ). Data with U_∞ =1m/s are excluded.

Dimensional analysis on ratio of equivalent diameter and injection hole diameter (D_E/D_i) is presented in Figure 8.6, data with U_∞=1m/s, and Figure 8.7, data without U_∞=1m/s. Outliers on top right are cases with small injection hole diameter (D_i=5mm) and relatively high injection angle ($\beta > 90$), injecting air toward the upstream flow. As it is observed earlier, the influence of jet speed (U_i), injection hole diameter (D_i), and boundary layer thickness (δ) is significant on the equivalent diameter (D_E). While the injection cross-flow speed (U_∞) and angle ($sin\beta$) are not as significant. Unlike the other two parameter, $cos\varphi$ and C/δ, the equivalent diameter (D_E) is not affected much by the cross-flow speed.

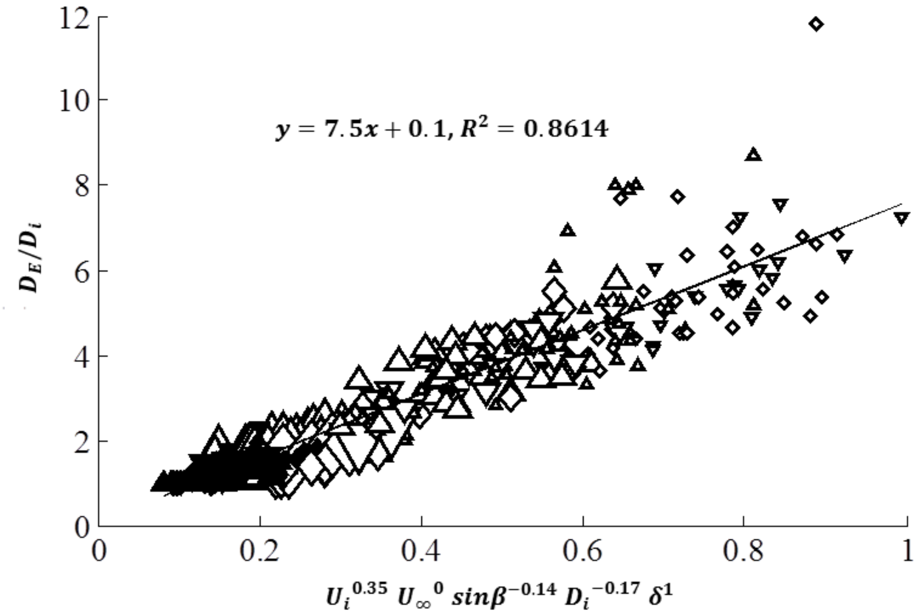

Figure 8.6 Dimensional analysis on ratio of equivalent diameter and injection hole diameter (D_E/D_i) with independent input variables, Jet speed (U_i), cross-flow speed (U_∞), vertical component of injection angle ($sin\beta$), injection hole diameter (D_i), boundary layer thickness (δ).

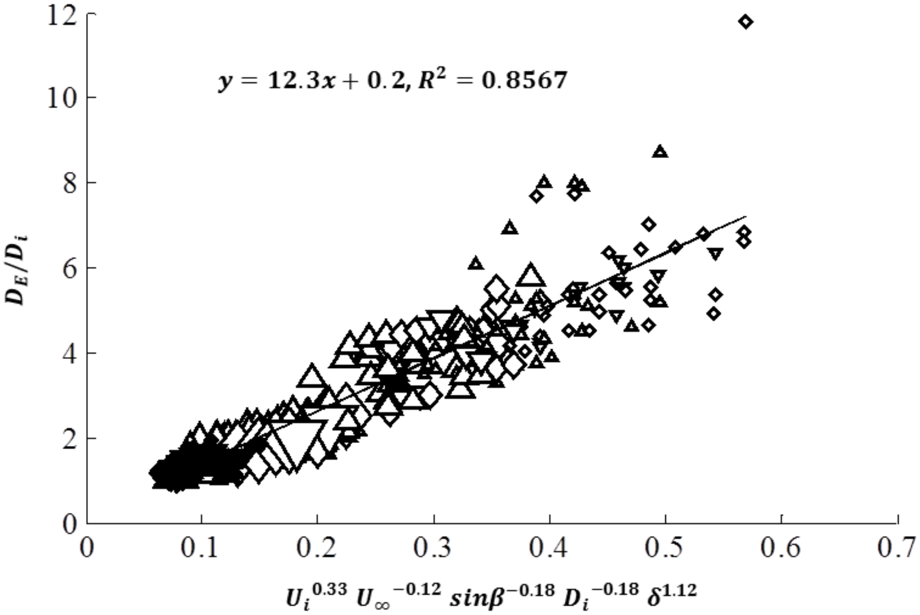

Figure 8.7 Dimensional analysis on ratio of equivalent diameter and injection hole diameter (D_E/D_i) with independent input variables, Jet speed (U_i), cross-flow speed (U_∞), vertical component of injection angle ($sin\beta$), injection hole diameter (D_i), boundary layer thickness (δ). Data with U_∞ =1m/s are excluded.

8.2 Non-dimensional analysis

According to π-theory, there should be four non-dimensional groups to scale the non-dimensional dependent variables, cosφ , C/δ , and D_E/D_i given all related independent parameters, U_∞, Q_i, D_i, β, δ, and g. These four non-dimensional groups were chosen to be $Q_i/U_\infty\delta^2$, $U_\infty/\sqrt{g\delta}$, $U_i sin\beta/U_\infty$, and $U_i cos\beta/U_\infty$. Last two parameters, $U_i sin\beta/U_\infty$ and $U_i cos\beta/U_\infty$. Note that

$$r = \frac{U_i}{U_\infty} = \sqrt{(\frac{U_i sin\beta}{U_\infty})^2 + (\frac{U_i cos\beta}{U_\infty})^2} \tag{8.1}$$

The volume flow rate ratio ($Q_i/U_\infty\delta^2$) represents the ratio of jet volume flow rate and cross-flow replacing volume flow rate in the boundary layer. The Froude number of cross-flow (Fr_δ=$U_\infty/\sqrt{g\delta}$) represents the inertia of the cross-flow and buoyancy across the boundary layer. Figure 8.8 presents the schematic drawing in the vicinity of injection hole from the side with parameter for non-dimensional analysis.

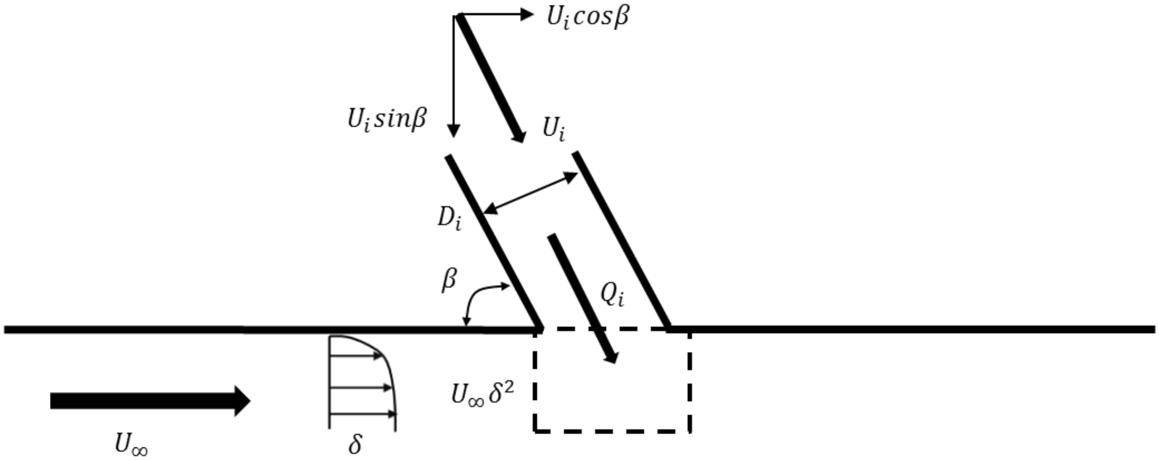

Figure 8.8 Side view in the vicinity of injection hole

The non-dimensional analysis on perpendicular component on the leg of sweep angle ($cos\varphi$) is presented in Figure 8.9, data with U_∞=1m/s, and Figure 8.10, data without U_∞=1m/s. Outliers on Figure 8.9 are cases with low cross-flow speed (U_∞=1m/s), small injection hole diameter (D_i=5mm), and relatively high jet speed (U_i). Both of the figures suggest that the Froude number is the most dominant parameter in this problem. The volume flowrate ratio, which indicates how much air is being injected, also contributes on formation of sweep angle. Speed ratios of the jet and cross-flow in both vertical and horizontal directions have relatively no contribution on the sweep angle. The sweep angle of the developed gas leg is dominated by the local Froude number and the inertia of the cross-flow.

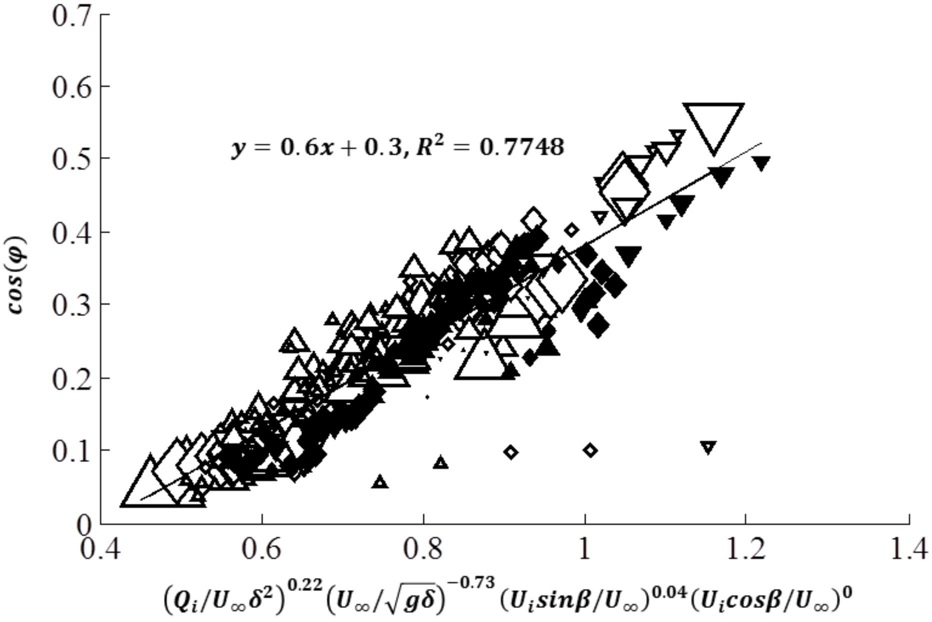

Figure 8.9 Scaling of perpendicular component of sweep angle ($cos\varphi$) with non-dimensional input variables, volume flow rate ratio ($Q_i/U_\infty\delta^2$), Froude number of cross-flow $\left(U_\infty/\sqrt{g\delta}\right)$, vertical component of speed ratio ($U_i sin\beta/U_\infty$), horizontal component of speed ratio ($U_i cos\beta/U_\infty$).

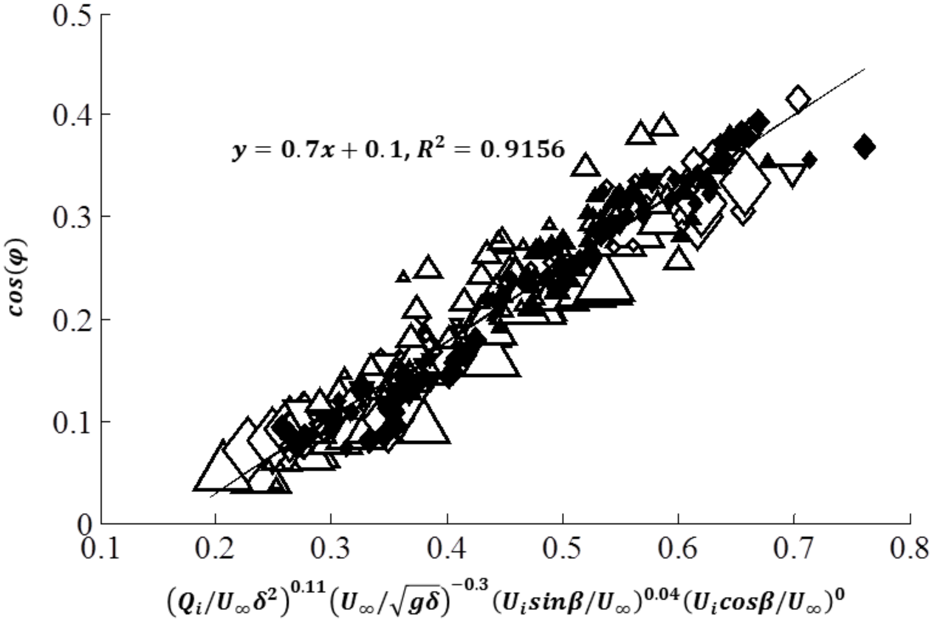

Figure 8.10 Scaling of perpendicular component of sweep angle ($cos\varphi$) with non-dimensional input variables, volume flow rate ratio ($Q_i/U_\infty\delta^2$), Froude number of cross-flow $\left(U_\infty/\sqrt{g\delta}\right)$, vertical component of speed ratio ($U_i sin\beta/U_\infty$), horizontal component of speed ratio ($U_i cos\beta/U_\infty$).Data with U_∞ =1m/s are excluded.

The non-dimensional analysis of chord length of leg to boundary layer thickness (C/δ) ratio is presented in Figure 8.11, data with U_∞=1m/s, and Figure 8.12, data without U_∞=1m/s. Again, the Froude number is the most dominant parameter in this analysis. Since the majority of the gas flux is presumed to occur in the two legs, the, volume rate ratio is also an important parameter. The speed ratios of jet and cross-flow in both vertical and horizontal directions have relatively no contribution on topology of the leg. As was also observed for the sweep angle, the topology of the leg (chord length) is far-field structure and in the region where the Froude number dominates.

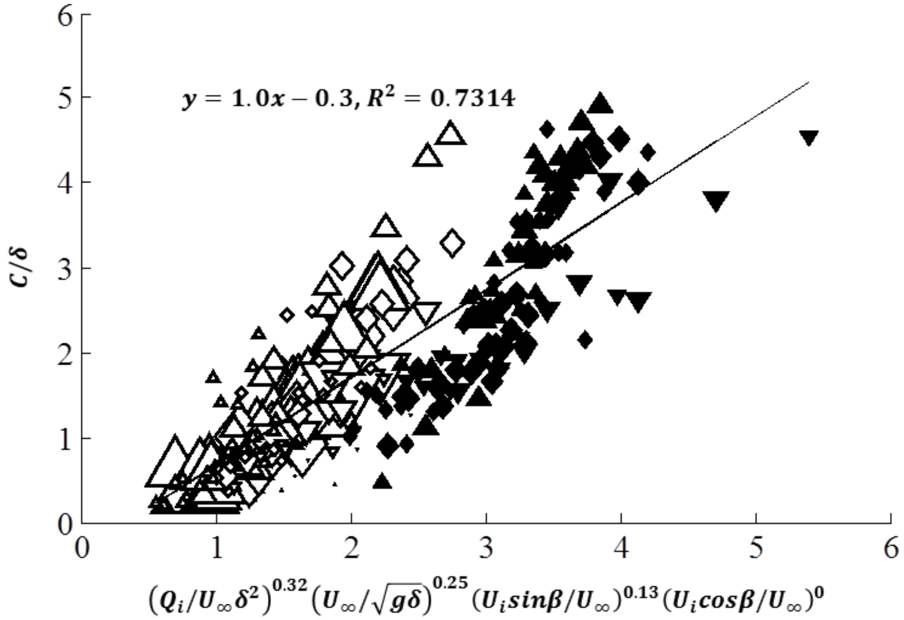

Figure 8.11 Scaling of ratio of chord length of the leg and boundary layer thickness (C/δ) with non-dimensional input variables, volume flow rate ratio $(Q_i/U_\infty\delta^2)$, Froude number of cross-flow $\left(U_\infty/\sqrt{g\delta}\right)$, vertical component of speed ratio $(U_i sin\beta/U_\infty)$, horizontal component of speed ratio $(U_i cos\beta/U_\infty)$.

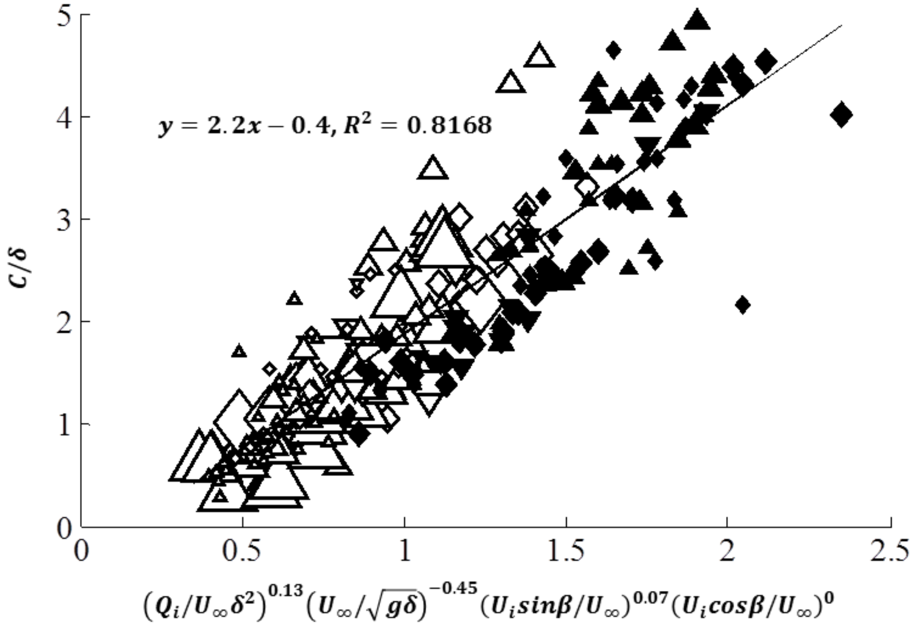

Figure 8.12 Scaling of ratio of chord length of the leg and boundary layer thickness (C/δ) with non-dimensional input variables, volume flow rate ratio ($Q_i/U_\infty\delta^2$), Froude number of cross-flow $\left(U_\infty/\sqrt{g\delta}\right)$, vertical component of speed ratio ($U_i sin\beta/U_\infty$), horizontal component of speed ratio ($U_i cos\beta/U_\infty$). Data with U_∞ =1m/s are excluded.

Non-dimensional analysis on ratio of equivalent diameter and injection hole diameter (D_E/D_i) is presented in Figure 8.13, data with U_∞=1m/s, and Figure 8.14, data without U_∞=1m/s. Outliers on top left are cases with small injection hole diameter (D_i=5mm) and relatively high injection angle ($\beta > 90$), injecting air toward upstream. Unlike previous two parameters, which represent far-field structure, the speed ratio of jet and cross-flow (especially the vertical velocity component), and the volume flowrate ratio are the dominant parameters. The area of the gas jet discharge occurs along a distance of 2δ to 3δ , which is in the near field of the gas jet. Here the Froude number relatively has a minimal contribution on the diameter ratio.

From the scaling, it is now clear that the resulting flow has two regions with different characters, near-field and far-field. The sweep angle ($cos\varphi$) and the topology of the leg (C/δ) are in far-field region, and the ratio of the equivalent diameter and injection hole diameter (D_E/D_i) is in near-field region, where the jet “puffing” occurs.

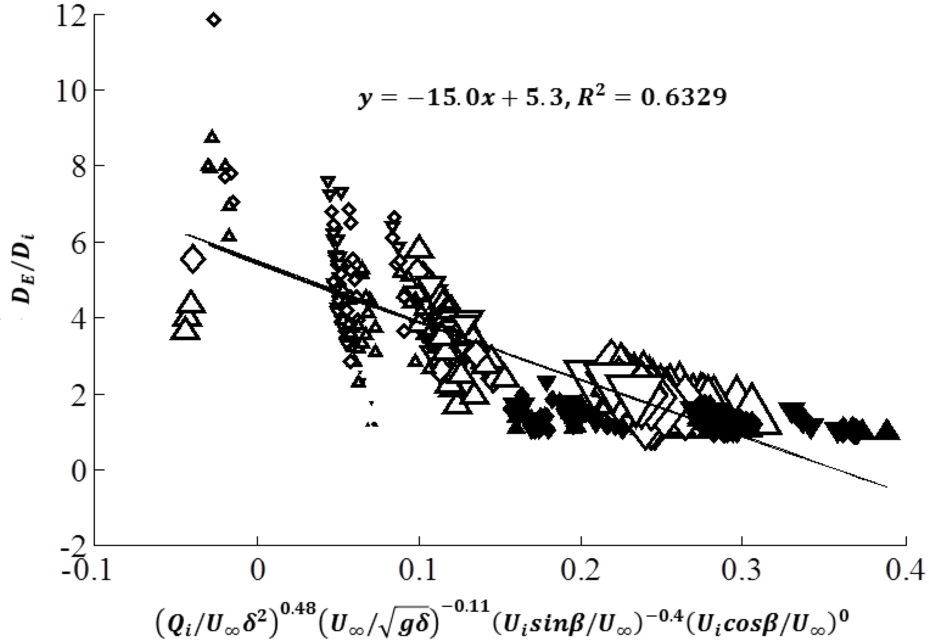

Figure 8.13 Scaling of ratio of equivalent diameter and injection hole diameter (D_E/D_i) with non-dimensional input variables, volume flow rate ratio ($Q_i/U_\infty\delta^2$), Froude number of cross-flow $\left(U_\infty/\sqrt{g\delta}\right)$, vertical component of speed ratio ($U_i sin\beta/U_\infty$), horizontal component of speed ratio ($U_i cos\beta/U_\infty$).

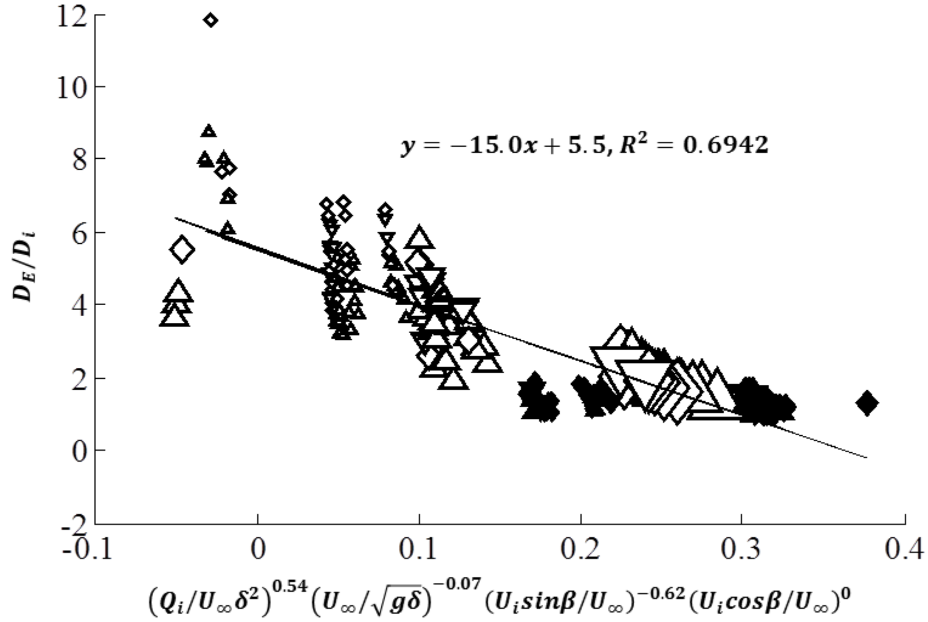

Figure 8.14 Scaling of ratio of equivalent diameter and injection hole diameter (D_E/D_i) with non-dimensional input variables, volume flow rate ratio ($Q_i/U_\infty\delta^2$), Froude number of cross-flow $\left(U_\infty/\sqrt{g\delta}\right)$, vertical component of speed ratio ($U_i sin\beta/U_\infty$), horizontal component of speed ratio ($U_i cos\beta/U_\infty$). Data with U_∞ =1m/s are excluded.

CHAPTER 9

Discussion on Interaction of Vertical jet with Cross-flow beneath Horizontal surface

General topology and measurements observed in interaction of vertical gas jet with liquid cross-flow beneath horizontal surface experiment and their scaling were presented in chapter 7 and chapter 8. This chapter will present physical explanation of the phenomenon. The questions that should be answered to explain the physics are listed below.

- Why does the flow in the present study different from the flow with horizontal jet into vertical cross-flow (Pignoux 1998)? Why does the flow split into two legs?
- What parameters decide the topology of the leg (sweep angle, chord length and thickness of the leg)?
- What is the physics of puffing at the injection hole (equivalent diameter)?
- Why does the flow with low cross-flow speed differ from higher cross-flow speed?

9.1 Effect of Gravity in the flow

In order to answer the first question, “Why does this flow different from the flow with horizontal jet into vertical cross-flow (Pignoux 1998)?” and “Why does the flow split into two leg?”, the conditions of each flow should be compared. The most remarkable difference between them is directions of the jet and cross-flow relative to the direction of gravity. Other parameters are in the similar range or at least of the same order. Table 10.1 compares the conditions on each flow.

	Pignoux 1998	**This study**
Jet direction	**Horizontal (perpendicular to gravity)**	**Vertical (along gravity)**
Cross-flow direction	**Vertical (along gravity)**	**Horizontal (perpendicular to gravity)**
Fr_{D_i} (=$\frac{U_\infty}{\sqrt{gD_i}}$)	**18.39 ~ 54.41**	**2.27 ~ 22.93**
Re_{D_i} (=$\frac{U_i D_i}{\nu_i}$)	**5.74E+3 ~ 2.06E+4**	**2.20E+2 ~ 1.76E+4**
Π (=$\frac{\rho_i {U_i}^2}{\rho_\infty {U_\infty}^2}$)	**4.39 ~ 52.27**	**1.07E-3 ~ 61.40**
r (=$\frac{U_i}{U_\infty}$)	**60.00 ~ 208.66**	**0.90 ~ 225.80**

Table 9.1 Comparison of two flows, Pignoux (1998) and the present study

In case of study of Pignoux (1998), due to momentum of the cross-flow(liquid), the gas jet deflects along the direction of the cross-flow, which is also the same direction of gravity. As the cross section of the jet expands in a form of gas pocket as the flow develops along the cross-flow, the jet breaks down to form a bubbly flow when the jet volume flow rate required to maintain the gas pocket of given cross-section becomes larger than the jet volume flow rate at the injector. Bubbles after the gas pocket experience vortical flow due to separation of the flow. When the bubbles inside the vortical flow break down to smaller size that has less effect of buoyancy, they evacuate the region and flow along the cross-flow. Figure 9.1 presents the image of the flow (Pignoux, 1998). It can be observed that the jet expands until the gas pocket breaks down into a bubbly flow.

In the present study, structure of the resulting flow is remarkably different. The discharged gas jet deflects along the direction of the cross-flow as it does in Pignoux's work. At the same time, the jet is forced to return toward the surface due to the presence of buoyancy. The jet tends to expand in the spanwise direction but not in vertical direction. Due to both momentum of cross-flow and gravity, the jet forms a hump after the injection area and then impinges back on to the flow surface. Then, the gas pocket splits into two legs. From Figure 9.2, it is observed that the flow splits into two legs around jet impingement. This suggests the jet impingement contributes to the splitting. At this point, however, we cannot conclude that the jet impingement directly splits the flow.

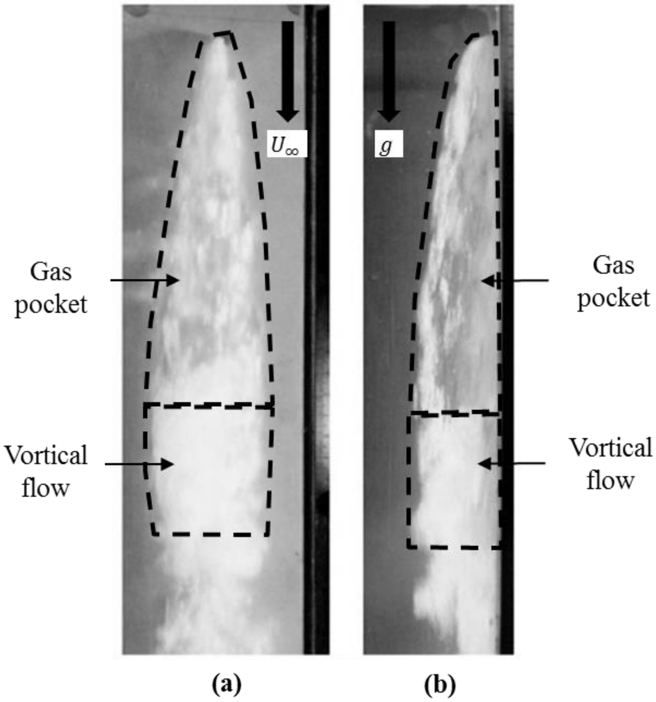

Figure 9.1 Image of a flow from Pignoux 1998. U_∞=3.0m/s, Q_i=2.67E-4m^3/s, D_i=1.0mm

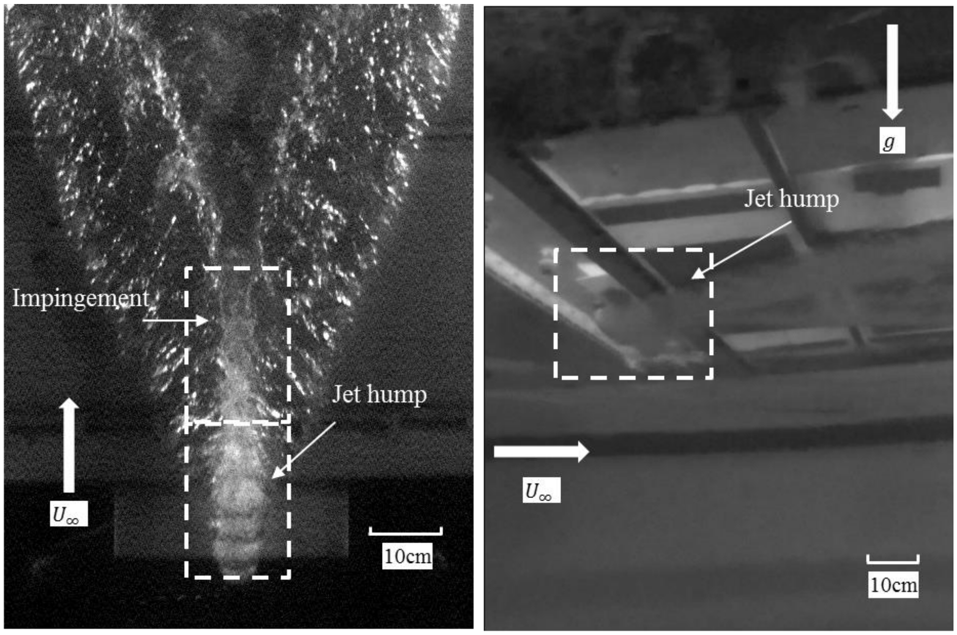

(a) **(b)**

Figure 9.2 Image of hump and impingement of the jet. U_∞=2.0m/s, Q_i=1.1E-2m^3/s, D_i~10.0mm

The influence of gravity on this flow has been investigated using a companion numerical simulation. The simulation was performed by Dr. Grzegorz Filip using OpenFoam, an open-source finite volume CFD toolbox. The solver interFoam is used together with the Volume of Fluid method for the interface treatment and the PISO algorithm for pressure-velocity coupling. The simulation was done by solving the single-fluid formulation of the multiple-phase governing equations: continuity and conservation of momentum equations, and advection equation for alpha, the phase-indicator. The equations are discretized on a computational grid with approximately 11 million cells. No explicit turbulence model is used and instead the truncation and discretization errors mimic the behavior of the subgrid-scale stresses in the adopted implicit large-eddy simulations approach. The upstream inlet boundary layer has a prescribed velocity profile based on the experimental measurements from the present study and the injector port has a fixed inlet velocity also based on the experimental values.

Figure 9.3 presents two cases from the simulation. Each case has the same flow conditions with the exception of the value of the gravity force. The results shown on the left is for a flow with gravity perpendicular to the flow (as in the experiment), and the image on the right is a simulation without gravity. Note that the flow without gravity does not lead to the cavity split, while the flow with gravity results in the formation of two legs. This result illustrates the importance of buoyancy in the problem, and is consistent with the observed importance of the Froude number in the previous scaling.

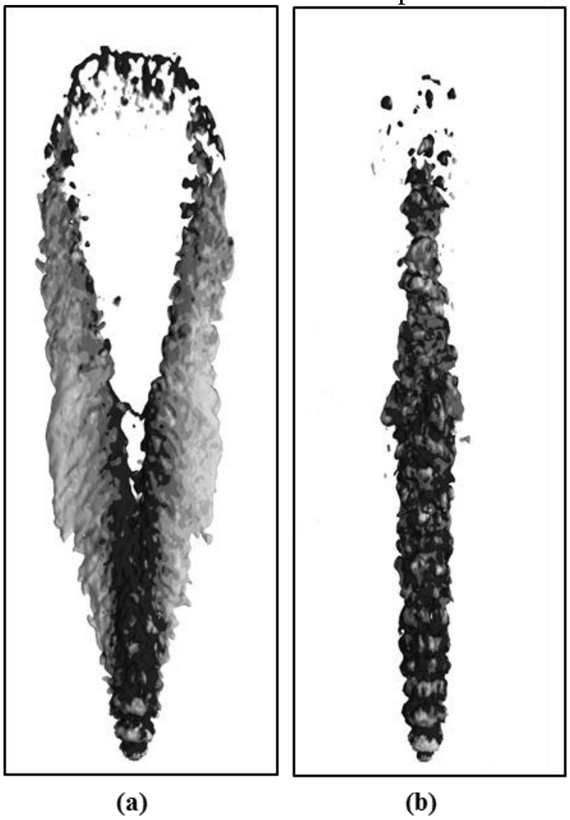

Figure 9.3 Numerical simulation of vertical jet injection into cross-flow beneath horizontal surface with U_∞=3.0m/s, Q_i=5.0E-3m^3/s, D_i~10.0mm. (a) with gravity and (b) without gravity. Figure by Dr. Grzegorz Filip

9.2 Force equilibrium at cross section of the leg

In order to better understand the flow around the gas leg away from the point of gas injection, a model of the leg has been constructed. The leg has been modeled as a two-dimensional flow with freestream speed $U_\infty cos\varphi$, the component of the flow perpendicular to the leg. Moreover, the gas pocket is modeled as the closed cavity forming behind an arbitrary cavitator, a fixed point of cavity detachment. Figure 9.4 presents the cavitator, the gas pocket which represents the cross-section of the leg, and a control volume defining the flow around the gas pocket. The liquid domain is closed by the cavitator and part of the cavity interface.

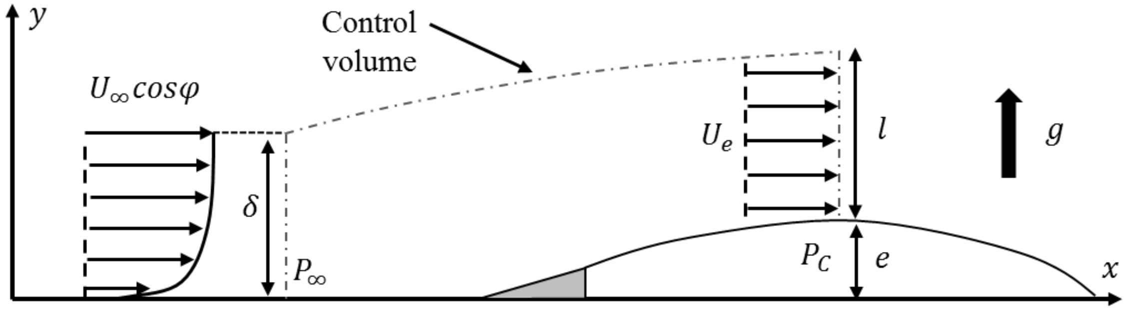

Figure 9.4 Schematic drawing of cross section of leg with control volume

The flow into the control volume has free stream speed, $U_\infty cos\varphi$ in the x direction, and a boundary layer thickness, δ. The pressure on the bottom surface is P_∞ and the pressure inside the cavity is P_C. The maximum thickness of the cavity is e and the length of the exit on the top of the cavity surface is l. The outlet speed of the liquid exiting the control volume is assumed to be uniform in the x direction with magnitude U_e. The shape of the control volume is set to have no cross-flow out of the top of the control volume. A relationship between δ and l can be derived using conservation of mass:

$$\int_0^\delta U_\infty cos\varphi \left(\frac{y}{\delta}\right)^{1/n} dy = U_e l \tag{9.1}$$

And by assuming $U_\infty cos\varphi \cong U_e$, equation 9.1 simplifies into:

$$\frac{n}{n+1}\delta \; = \; l \tag{9.2}$$

The *x*-momentum balance in this domain leads to the derivation of the drag force, D:

$$D =$$

$$\int_0^\delta (P_\infty + \rho_\infty gy)\,dy + \int_\delta^{e+l} (P_\infty + \rho_\infty gy)\,dy - \int_0^e P_C\,dy - \int_e^{e+l} \big(P_C + \rho_\infty g(y-e)\big)\,dy \tag{9.3}$$

$$+ \int_0^\delta \rho_\infty \left(U_\infty cos\varphi \left(\frac{y}{\delta}\right)^{1/n}\right)^2 dy - \int_e^{e+l} \rho_\infty {U_e}^2\,dy$$

Solving and dividing D by $\frac{1}{2}\rho(U_\infty cos\varphi)^2 e$, the drag coefficient, C_D, is obtained:

$$C_D = \frac{D}{\frac{1}{2}\rho_\infty (U_\infty cos\varphi)^2 e}$$

$$= \frac{(P_\infty - P_C)}{\frac{1}{2}\rho_\infty (U_\infty cos\varphi)^2}\left(1 + \frac{n}{n+1}\frac{\delta}{e}\right) + \frac{g\delta}{(U_\infty cos\varphi)^2}\left(\frac{e}{\delta} + \frac{2n}{n+1}\right) - \frac{2n}{(n+1)(n+2)}\frac{\delta}{e} \tag{9.4}$$

$$= \frac{\sigma}{cos^2\varphi}\left(1 + \frac{n}{n+1}\frac{\delta}{e}\right) + \frac{1}{cos^2\varphi}\frac{1}{{Fr_\delta}^2}\left(\frac{e}{\delta} + \frac{2n}{n+1}\right) - \frac{2n}{(n+1)(n+2)}\frac{\delta}{e}$$

where cavitation number, σ, and Froude number based on boundary layer thickness, Fr_δ is:

$$\sigma = \frac{(P_\infty - P_C)}{\frac{1}{2}\rho_\infty {U_\infty}^2} \tag{9.5}$$

$$Fr_\delta = \frac{U_\infty}{\sqrt{g\delta}} \tag{9.6}$$

To verify the derivation, replacing inlet velocity profile to uniform flow and removing gravity should be equivalent with classic solution of cavitator in free stream without gravity:

$$D \; = \; (P_\infty - P_C)e \tag{9.7}$$

The solution (equation 9.7) is from *Fundamental of Cavitation* (Franc, 2004).

$$(C_D)_{n\rightarrow\infty} = \frac{(P_\infty - P_C)}{\frac{1}{2}\rho_\infty (U_\infty cos\varphi)^2 e}\left(1+\frac{\delta}{e}\right) + \frac{g\delta}{{U_i}^2}\left(\frac{e}{\delta}+2\right) \tag{9.8}$$

$$(C_D)_{n\rightarrow\infty,\delta\rightarrow 0,g\rightarrow 0} = \frac{(P_\infty - P_C)}{\frac{1}{2}\rho_\infty (U_\infty cos\varphi)^2 e} \tag{9.9}$$

The classic solution (equation 9.7) and solution of the present study (equation 9.9) are equivalent.

Since there is no actual cavitator fixed on the surface in the present study, drag force, D, should be zero at the equilibrium state when the gas pocket is stationary in the lab frame. Then, equation 9.4 yields the force equilibrium condition:

$$0 = \frac{\sigma}{cos^2\varphi}\left(1+\frac{n}{n+1}\frac{\delta}{e}\right) + \frac{1}{cos^2\varphi}\frac{1}{{Fr_\delta}^2}\left(\frac{e}{\delta}+\frac{2n}{n+1}\right) - \frac{2n}{(n+1)(n+2)}\frac{\delta}{e} \tag{9.10}$$

From equation 9.3, force equilibrium can be achieved by varying the cavitation number (σ), the sweep angle (φ), and the cavity thickness (e) for given ρ, δ, U_∞, P_∞, Q_i, and g. If cavitation number (σ) and cavity thickness (e), then sweep angle (φ) also should be constant to maintain force equilibrium state on the leg. This is consistent with the observation the leading edge of the gas leg forms a straight line.

Assuming that the injected air only moves through legs (*i.e.* a pure lambda configuration) and flows with the average speed of liquid moving parallel to the leg, we can estimate the area of the leg cross section. Then, assuming that the cross section is semi-ellipse, chord length and thickness of the leg can be calculated:

$$Q_i = \frac{\pi C\hat{e}}{2}U_\infty sin\varphi \tag{9.11}$$

where $\hat{e}$ is calculated thickness and $U_i sin\varphi$ is fluid speed along the leg.

Figure 9.5 presents ratio of calculated leg thickness and boundary layer thickness ($\hat{e}/\delta$) with varying ${Fr_\delta}^*$ and σ^*, with the redefined Froude and cavitation numbers now scaling the velocity with $cos\varphi$. Varying cavitation numbers are plotted as solid lines.

The 1/7th law for boundary layer profile is applied. Again, different symbols represent different types of the jet: △Delta type, ◇Transition type, ▽Lambda type. The face color of the markers represents boundary layer profile(Barge model): ▲δ_1 (Barge model I) and △δ_2 (Barge model II). The size of the markers represents the diameter of the injection hole: △D_i=5.0mm, △D_i=10.0mm, and △D_i=20.0mm. Most of the data suggests that the cavitation numbers are negative, which means that the pressure in the leg (P_C) is larger than pressure on the surface of the flow boundary (P_∞), which is in fact the lowest pressure in the freestream flow. The pressure difference ($\mathrm{P}_\infty - \mathrm{P}_C$) is about 0~0.9kPa considering most of the data points lie -5< σ^* <0. And 0.9kPa is a very small value compared to P_∞, 102.7kPa.

Definition of ${Fr_\delta}^*$ and σ^* are:

$$\sigma^* = \frac{(P_\infty - P_C)}{\frac{1}{2}\rho_\infty (U_\infty cos\varphi)^2} \tag{9.12}$$

$${Fr_\delta}^* = \frac{U_\infty cos\varphi}{\sqrt{g\delta}} \tag{9.13}$$

Force equilibrium equation using ${Fr_\delta}^*$ and σ^* is:

$$0 = \sigma^* \left(1 + \frac{n}{n+1}\frac{\delta}{e}\right) + \frac{1}{({Fr_\delta}^*)^2}\left(\frac{e}{\delta} + \frac{2n}{n+1}\right) - \frac{2n}{(n+1)(n+2)}\frac{\delta}{e} \tag{9.14}$$

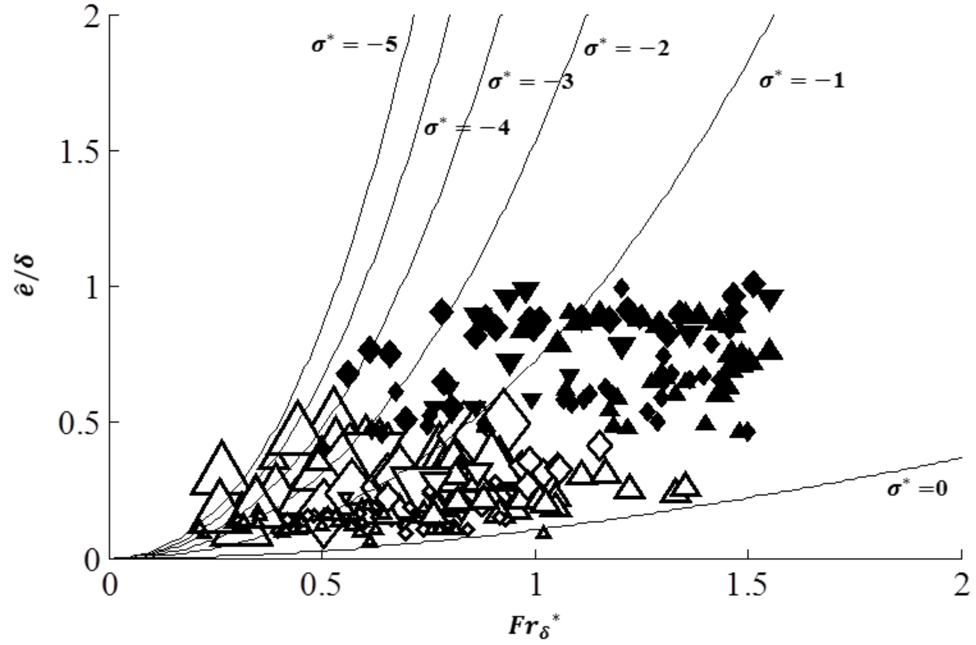

Figure 9.5 Ratio of calculated leg thickness and boundary layer thickness ($\hat{e}/\delta$) with varying Froude number ($Fr_\delta{}^*$) is presented. Different cavitation numbers (σ^*) based on force equilibrium equation (9.14) are plotted in solid lines. Data with U_∞ =1m/s are excluded.

For better understanding, modified cavitation number ($\hat{\sigma}^*$) that has positive value with data points is introduced. The reference pressure for modified cavitation number ($\hat{\sigma}^*$) is pressure at boundary layer thickness upstream of the injection location ($P_\infty + \rho g \delta$) instead of pressure on the bottom surface alone (P_∞). The modified cavitation number ($\hat{\sigma}$) is defined as:

$$\hat{\sigma}^* = \frac{(P_\infty + \rho g \delta - P_C)}{\frac{1}{2}\rho_\infty (U_\infty cos\varphi)^2} = \sigma^* + \frac{2}{(Fr_\delta{}^*)^2} \tag{9.15}$$

Force equilibrium equation with modified cavitation number ($\hat{\sigma}^*$) becomes:

$$0 = \hat{\sigma}^* \left(1 + \frac{n}{n+1}\frac{\delta}{e}\right) + \frac{1}{(Fr_\delta{}^*)^2}\left(\frac{e}{\delta} - \frac{2n}{n+1}\frac{\delta}{e} - \frac{2}{n+1}\right) - \frac{2n}{(n+1)(n+2)}\frac{\delta}{e} \tag{9.16}$$

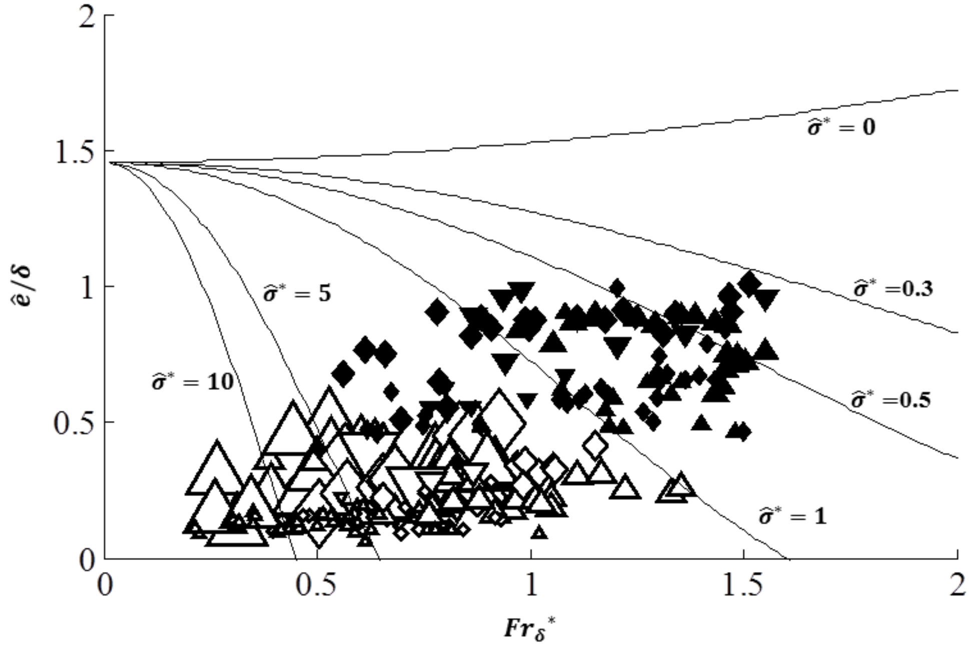

Figure 9.6 Ratio of calculated leg thickness and boundary layer thickness ($\hat{e}/\delta$) with varying Froude number (${Fr_\delta}^*$) is presented. Different modified cavitation numbers ($\hat{\sigma}^*$) based on force equilibrium equation (9.16) are plotted in solid lines. Data with U_∞ =1m/s are excluded.

Figure 9.6 presents $\hat{e}/\delta$ with varying Fr_δ and varying $\hat{\sigma}^*$. The 1/7th law for boundary layer profile is applied. All of the data points are in modified cavitation number positive region, which suggests that the pressure inside the leg (cavity) is slightly lower than pressure of surrounding fluid. Then the balance of inertia and pressure forces at the cavity interface will cause the cavity to curve towards the surface once the maximum cavity thickness is achieved, and this results in the closure of the leg, as illustrated by Franc (2004). This would therefore explain why the flow splits into two legs, as the equilibrium pressure in the gas pocket would lead to local cavity closure for each leg. Again, the range of pressure difference ($P_\infty + \rho g \delta - P_C$) is 0.1~1.8kPa considering most of the data points lie $0.3< \hat{\sigma}^* <10$, which is very small comparing to P_∞, 102.7kPa.

By assuming Pressure in the leg (P_C) is in the same order with hydrostatic pressure at thickness of leg: $P_C = P_\infty + \varepsilon \rho g e$ (0< ε <1), force equilibrium equation can be expressed only with ${Fr_\delta}^*$ and e/δ:

$$0 = \frac{1-2\varepsilon}{({Fr_\delta}^*)^2}\left(\frac{e}{\delta}\right)^2 + \frac{2n(1-\varepsilon)}{(n+1)(1-2\varepsilon)}\frac{1}{({Fr_\delta}^*)^2}\left(\frac{e}{\delta}\right) - \frac{2n}{(n+1)(n+2)} \tag{9.17}$$

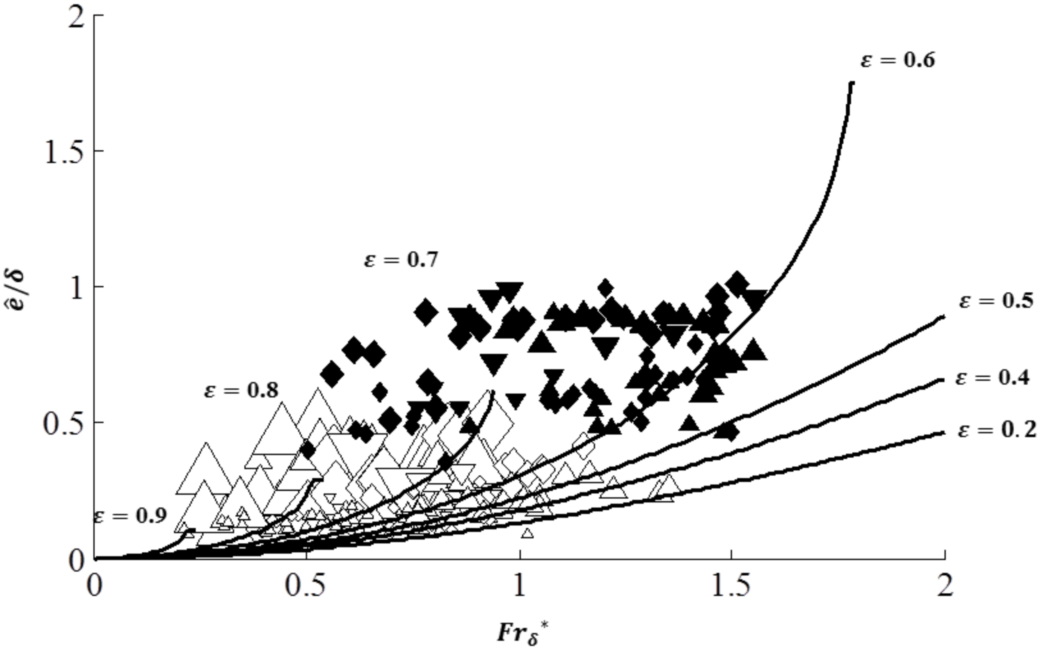

Figure 9.7 Ratio of leg thickness and boundary layer thickness (e/δ) is plotted as a function of Froude number (${Fr_\delta}^*$) with known P_C comparing with data points with calculated leg thickness ($\hat{e}$). Data with U_∞ =1m/s are excluded.

The solution of e/δ when $0 \leq \varepsilon < 1$:

$$\frac{e}{\delta} = \frac{(\varepsilon-1)}{(n+1)(1-2\varepsilon)} \pm \frac{1}{2}\sqrt{\left(\frac{n(1-\varepsilon)}{(n+1)(1-2\varepsilon)}\right)^2 + \frac{8n}{(n+1)(n+2)}\frac{({Fr_\delta}^*)^2}{1-2\varepsilon}} \tag{9.18}$$

The solution of e/δ when $\varepsilon = 1/2$:

$$\frac{e}{\delta} = \frac{({Fr_\delta}^*)^2}{(n+2)(1-\varepsilon)} \tag{9.19}$$

Figure 9.7 presents e/δ plotted as a function of Froude number ($Fr_{\delta}{}^{*}$) for a given P_C. Comparing with data points with calculated leg thickness ($\hat{e}$). Part of data points lie between $\varepsilon = 0.2$ and $\varepsilon = 0.9$.

9.3 Relationship for the cavity pressure (P_C) to find $cos\hat{\varphi}$ and C/δ

In order to determine the relationship between the observed variables, a relationship is needed between the cavity pressure and the independent variables. The pressure inside the gas leg (cavity), P_C, is related to the volume rate of the injected air and the rate of gas entrainment at the local cavity closure and the terminus of the leg at the farthest downstream extent of the gas pocket. Without additional direct measurements of the pocket pressure, a relationship between the flow rate and gas pressure must be assumed. Here, it will assumed that the following relationship described the cavity pressure

$$P_C = P_\infty \left(1 + a\left(\frac{Q_i}{U_\infty \delta^2}\right)^b\right) = P_\infty\left(1 + aQ^{*b}\right) \tag{9.20}$$

where Q^* is volume ratio of the jet and cross-flow, and a and b are constants yet to be determined.

Using equation 9.20 and assumption $P_C = P_\infty + \varepsilon\rho g e$ (0< ε <1), e can now be expressed in terms of Q^*, a, b, and ε.

$$\check{e} = aQ^{*b}\,\frac{P_\infty}{\rho g \varepsilon} \tag{9.21}$$

where $\check{e}$ is calculated thickness of the leg using Q^*. From equation 9.20 and 9.21, force equilibrium equation, now, become;

$$cos\hat{\varphi} = \tag{9.22}$$

$$\sqrt{(n+2)(1-\varepsilon)\frac{1}{{Fr_\delta}^2}aQ^{*b}\frac{P_\infty}{\rho g\delta\varepsilon}+\frac{(n+1)(n+2)}{2n}(1-2\varepsilon)\frac{1}{{Fr_\delta}^2}\left(aQ^{*b}\frac{P_\infty}{\rho g\delta\varepsilon}\right)^2}$$

where $\hat{\varphi}$ is calculated sweep angle. With equation 9.22, the sweep angle is not a function of only the independent variables and the three unknown constants, ε, a, and b.

Figure 9.8 compares calculated sweep angle ($cos\hat{\varphi}$) and the measured sweep angle ($cos\varphi$) with varying Froude number ($Fr_\delta = U_\infty/\sqrt{g\delta}$). Marker × represents $cos\hat{\varphi}$ and marker △/◇/▽ represent Delta type, Transition type, and Lambda type of $cos\varphi$. Regression was used to fit the best values of ε, a, and b. The values are $a = 1.8\text{E} - 4$, $b = 0.2$, and $\varepsilon = 0.4$. Calculated and measured data show good agreement. Moreover, the power exponents of Fr_δ and Q^* in terms of $cos\hat{\varphi}$ are about -1 and 0.2, which are close to exponents of -0.73 and 0.22 derived from the $cos\varphi$ scaling results shown in Figure 8.10

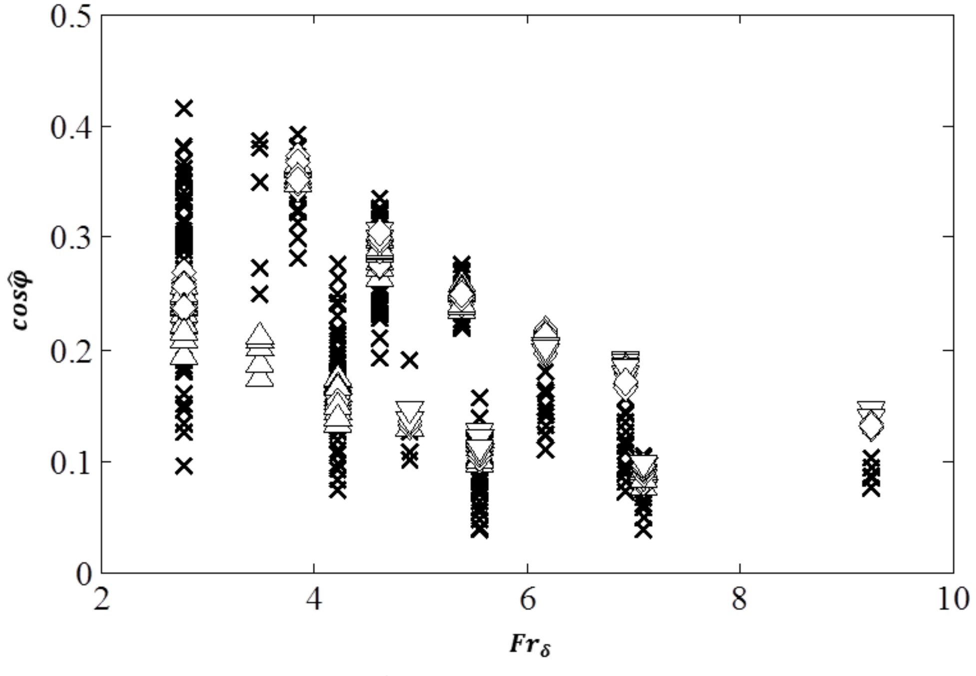

Figure 9.8 Calculated sweep angle ($\cos\hat{\varphi}$) and measured sweep angle ($\cos\varphi$) are plotted as a function of Froude number (Fr_δ). Data with U_∞ =1m/s are excluded.

The chord length of the gas leg (C) can also be calculated using the assumption on air volume flow rate (Q_i) the thickness of the leg (e), and an assumed cross section as was done to determine $\hat{e}$ using equation 9.11. This equation will be modified with the constant γ and combined with equation 9.21 to compute the chord length

$$\hat{C} = \gamma \frac{2Q_i}{\pi \check{e} U_\infty sin\varphi} = \gamma Q^{*(1-b)} \frac{2\delta^2 \rho g \varepsilon}{a\pi P_\infty sin\varphi} \tag{9.23}$$

where $\hat{C}$ is calculated chord length. And γ is constant coefficient which can correct the product of the combination of air flow rate(Q_i), air flow speed ($U_\infty sin\varphi$), and area of the leg cross section ($\frac{\pi}{2}Ce$). In effect, the coefficient could correct for air leakage, variation in the sectional area of the leg from an elliptic shape, and/or variation in the average air flow speed in the leg.

Figure 9.9 compares calculated chord length ($\hat{C}$) and measured chord length (C) with varying Q^* ($= Q_i/U_\infty\delta^2$) after regression was used to determine γ assming the previously determined values for ε, a, and b . Marker × represents $\hat{C}$ and marker △/◇/▽ represent Delta type, Transition type, and Lambda type of C. Each coefficient has values, $a = 1.8\mathrm{E}-4$, $b = 0.2$, $\varepsilon = 0.4$, and $\gamma = 0.3$. A value of $\gamma = 0.3$ was determined to produce the best data fit. Hence, the cross-section of the leg was assumed to be semi-ellipse but may be a shape with somewhat smaller cross sectional area. And/or, the air flow speed in the leg is assumed to be equivalent to the component of the freestream speed parallel to the leg, but actual average gas speed in the leg may be slower than that. Finally, this calculation does not take into account air leakage from the leg that makes a Delta or Transition type topologies. This too would lead to a value of $\gamma < 1$. Hence, all three considerations would suggest that γ to be smaller than 1. The calculated data show good agreement with measured data using the four coefficients from the regression.

$\hat{C}$ can also be expressed with Fr_δ and Q^*;

$$\hat{C} = \gamma Q^{*(1-b)} \frac{1}{{Fr_\delta}^2} \frac{2\rho\varepsilon\delta U_\infty}{\mathrm{a}\pi P_\infty sin\varphi} \tag{9.24}$$

In equation 9.24, the power of Fr_δ and Q^* in $\hat{C}$ are -2 and 0.8. Comparing these values with power from $\hat{C}$ scaling, -0.45 and 0.13, shown in Figure 8.12. Here, the ratio of the exponents are similar (~3), but they differ by a factor of ~4.

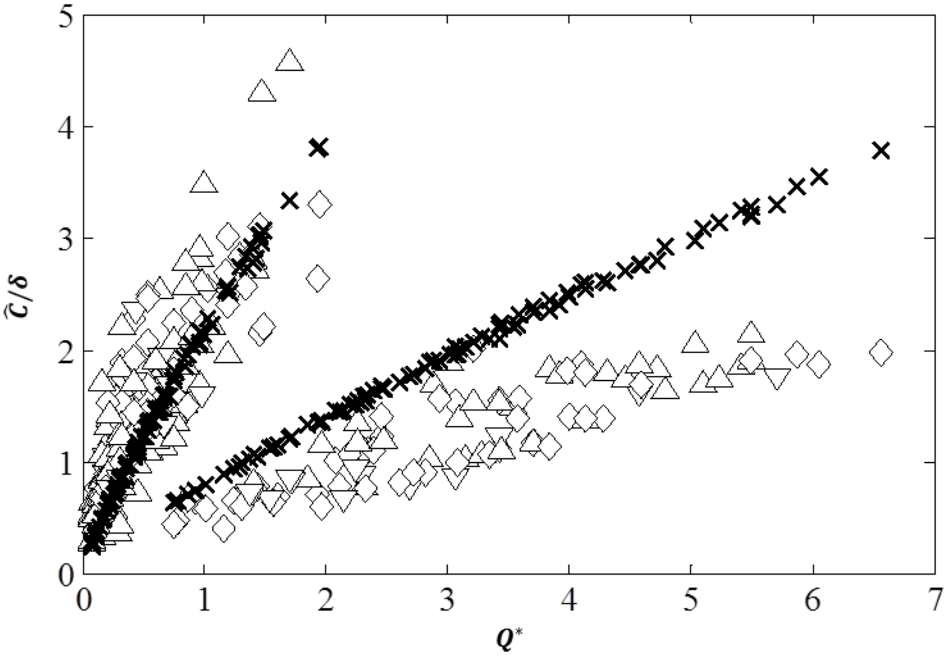

Figure 9.9 Calculated chord length ($\hat{C}$) and measured chord length (C) are plotted as a function of Q^*. Data with U_∞ =1m/s are excluded.

9.4 Stability of the leg

With the previous relationships, the stability of the gas leg can now be analyzed. Figure 9.10 presents the direction of drag force (D) and sweep angle (φ). In order to have stable system, there should be a restoring force back to the equilibrium sweep angle if the leg undergoes a perturbation in sweep angle.

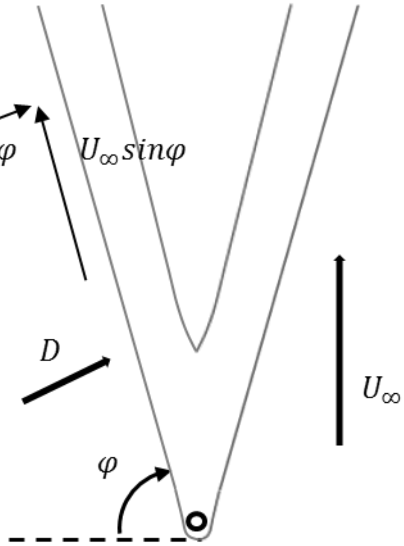

Figure 9.10 Schematic drawing of the legs with direction mark of drag force (D) and sweep angle (φ)

Therefore, the sign of derivative of D with φ around the point of equilibrium will indicate if the legs are in a stable position. To determine this derivative, the following assumptions are used.

- Pressure in the leg(P_C) is equivalent to hydrostatic pressure at depth in the order of thickness of leg: $P_C = P_\infty + \varepsilon\rho g e$, ($\varepsilon$=0.4)
- Pressure in the leg(P_C) is also related to volume ratio of jet and cross-flow(Q^*): $P_C = P_\infty\left(1 + aQ^{*b}\right)$, ($a$=1.8E-4 and b=0.2)

The drag on the leg can be written as,

$$D = \frac{n}{n+1}(1-\varepsilon)\rho g\delta\left(aQ^{*b}\frac{P_\infty}{\rho g\varepsilon}\right) + \left(\frac{1}{2}-\varepsilon\right)\rho g\left(aQ^{*b}\frac{P_\infty}{\rho g\varepsilon}\right)^2 - \frac{n}{(n+1)(n+2)}\rho {U_\infty}^2\delta cos^2\varphi \tag{9.25}$$

and the derivative of D with φ around the point of force equilibrium is

$$\left(\frac{\partial D}{\partial\varphi}\right)_{D=0} = -\frac{2n}{(n+1)(n+2)}\rho {U_\infty}^2\delta\, cos\varphi\, sin\varphi \tag{9.26}$$

In the present study, range of φ is from 0 to 90 degree. In this range of φ, the sign of the derivative of D with φ around the point of force equilibrium is always negative. When the sign is negative, a restoring force exists. In other words, when there is a positive perturbation on the sweep angle at force equilibrium state, a net negative drag force occurs, and this results in the leg returning to its equilibrium position. Similarly, if the sweep angle is reduced, the drag increases, the leg is pushed back.

9.5 Surface tension on the leg

Previous subsections showed that the resulting flow is dominated by inertia and buoyancy. However, cases with lower cross-flow speed, $U_\infty = 1$m/s, are different. Another parameter should be considered to understand its topology. Here, the surface tension is introduced in this subsection to explain cases with lower cross-flow speed.

Considering dynamic pressure and pressure due to surface tension at cross section of the leg are in unity:

$$\frac{1}{2}\rho_\infty\left(U_\infty cos\varphi\left(\frac{e}{\delta}\right)^{1/n}\right)^2 \sim \frac{S}{C} \tag{9.27}$$

where S is surface tension of water-air(S=0.072N/m) and radius of the cross section is assumed to be C. Modifying this equation to get Weber number:

$$\frac{S}{\rho_\infty {U_\infty}^2 C} \sim \frac{1}{2}cos^2\varphi\left(\frac{e}{\delta}\right)^{2/n} \tag{9.28}$$

By using average values from measurements for each parameter, $\left(\frac{e}{\delta}\right)_{avg.}$=0.8 and $(\cos\varphi)_{avg.}$=0.8, and assuming n=7 from 1/7th law, the Weber number is close to unity is about 0.02. Actual range of Weber number in the present study is 5.7E-5~0.005. By dividing this original range by 0.02, Weber number range in unity of two pressures can be calculated: 0.3E-2~0.2. Surface tension will dominate the flow only with very low speeds on the order of 0.1m/s or lower. In the present study, contribution of surface tension on the flow is very small overall. However, surface tension will more contribute on the flow relatively when cross-flow speed, U_∞, is on the order of 1 m/s.

9.6 Conclusions

We have shown that the structure of a gas jet penetrating beneath a horizontal surface results in a bifurcated gas pocket, and this is dissimilar from the pocket formed when the gas in injected perpendicular to the action of gravity. In the near field of the gas injector, buoyancy is not very important. But, not far from the injector, the action of buoyancy is the return the gas pocket closer to the surface, and, when it impinges, the gas legs are often formed. These gas pockets are stable and extend far downstream until gas entrainment causes them to collapse.

Previously proposed scalings for traditional jets are not necessarily appropriate for the flow. Instead, scaling suggests that the Froude number based on the boundary layer thickness is the primary parameter for scaling the flow in the two gas legs, followed by the gas volume injection rate. Traditional jet scaling may be more appropriate near the injection location where buoyancy has yet to affect the flow. A simplified analytical model was successfully developed to understand the formation and stability of the gas legs.

The study here was conducted for flows at moderate Froude numbers, where buoyancy both leads to the formation of the gas legs and dominates the flow around them. With increasing flow speed, we would expect that the flows would begin to resemble those reported by Pignoux (1998), where the influence of gravity was secondary. Further study would be needed to bridge these two regimes in Froude number.

Finally, an ongoing companion numerical study will be used to further the basic understanding of these flows as well as validate and refine the simpler analytical models and scaling presented here. And, further work will be conducted on the interaction of multiple injection sites.

REFERENCES

1. Andreopoulos, J. and Rodi, W., “Experimental investigation of jets in a crossflow”, *Journal of Fluid Mechanics*, Vol. 138, pp. 93-127, 1984.
2. Broadwell, J. E. and Breidenthal, R. E., “Structure and mixing of transverse jet incompressible flow”, *Journal of Fluid Mechanics*, Vol. 148, pp. 405-412, 1984.
3. Billet, M. L., and Weir, D. S., “The Effect of Gas Diffusion on the Flow Coefficient for a Ventilated Cavity”, *ASME Journal of Fluids Engineering*, Vol. 97, pp. 501-506, 1975.
4. Brennen, C. E., "The Dynamic Balance of Dissolved Air and Heat in Natural Cavity Flow”, *Journal of Fluid Mechanics*, Vol., 37, pp. 115-127, 1969.
5. Carreau, J. L., Roger, F., Loukarfi, L., Gbahoue, L., and Hobbes, Ph., “Penetration of a horizontal gas jet submerged in a liquid”, *21eme Congres De L’Iecec.*, 1986.
6. Ceccio, S. L., “Friction Drag Reduction of External Flows with Bubble and Gas Injection”, *The Annual Review of Fluid Mechanics*, Vol.42, pp.183-203, 2010.
7. Chassing, P., George, J., Claria, A., and Sananes, F., “Physical characteristics of subsonic jets in a cross-stream”, *Journal of Fluid Mechanics*, Vol. 62, part 1, pp. 41-64, 1974.
8. Cheslak, F. R., Nicholls, J. A., and Sichel, M., “Cavities formed on liquid surfaces by impinging gaseous jets”, *Journal of Fluid Mechanics*, Vol. 36, Part 1, pp. 55-63, 1969.

9. Chua, L. P. and Antonia, R. A., “Spatial organization of large structures in the near-field of a circular jet”, *Fluid Dynamics Research*, Vol. 9, pp. 59-71., 1992.
10. Coelho, S. L. V. and Hunt, J. C. R., “The dynamics of the near field of strong jets in crossflow”, *Journal of Fluid Mechanics*, Vol. 200, pp. 95-120, 1989.
11. Cohen, J. and Wygnanski, I. “The evolution of instabilities in the axisymmetric jet. Part 1. The linear growth of disturbances near the nozzle”, *Journal of Fluid Mechanics*, Vol. 176, pp. 191-219, 1987.
12. Cohen, J. and Wygnanski, I. “The evolution of instabilities in the axisymmetric jet. Part 2. The flow resulting from the interaction between two waves”, *Journal of Fluid Mechanics*, Vol. 176, pp. 221-235, 1987.
13. Coutier-Delgosha, O., Stutz, B., Vabre, A., and Legoupil, S., “Analysis of Cavitating Flow Structure By Experimental and Numerical Investigations”, *Journal of Fluid Mechanics*, Vol. 578, pp. 171-222, 2007.
14. Epstein, P. S. and Plesset, M. S., “On the Stability of Gas Bubbles in Liquid-Gas Solutions*”, Journal of Chemical Physics*, Vol. 18, pp. 1505-1508, 1950.
15. Franc, J-P, and Michel, J-M., “Fundamentals of Cavitation”, *Kluwer Academic Publishers*, 2004.
16. Fearn, R. and Weston, R. P., “Vorticity Associated with a Jet in a Cross Flow”, *AIAA Journal*, Vol. 12, No. 12, pp. 1666-1671, 1974
17. Freymuth, P., “On transition in a separated laminar boundary layer”, *Journal of Fluid Mechanics*, Vol. 25, part 4, pp. 683-704, 1966.
18. Fric, T. F. and Roshko, A., “Vortical structure in the wake of a transverse jet”, *Journal of Fluid Mechanics*, Vol. 279, pp. 1-47, 1994.
19. Gadd, G. E. and Grant, S., “Some Experiments on Cavities Behind Disks”, *Journal of Fluid Mechanics*, Vol. 23, No. 4, pp. 645-656, 1965.

20. Gutmark, E. and Ho C-M., “Preferred modes and the spreading rates of jets”, American Institute of Physics, Vol. 26, pp. 2932-2938., 1983.
21. Hasselbrink, E. F. and Mungal, M. G., “Transverse jets and jet flames. Part 1. Scaling laws for strong transverse jets”, *Journal of Fluid Mechanics,* Vol. 443, pp. 1-25, 2001.
22. Hasselbrink, E. F. and Mungal, M. G., “Transverse jets and jet flames. Part 2. Velocity and OH field imaging”, Hasselbrink, E. F. and Mungal, M. G., “Transverse jets and jet flames. Part 1. Scaling laws for strong transverse jets”, *Journal of Fluid Mechanics*, Vol. 443, pp. 1-25, 2001.
23. Insel, M, Gokcay, S., and Helvacioglu, I. H., “Flow Analysis of an Air Injection Through Discrete Air Lubrication”, *International Conference on Ship Drag Reduction*, paper No. 13, 2010.
24. Kamotani, Y. and Greber, I., “Experiments on a Turbulent Jet in a Cross Flow”, *AIAA Journal*, Vol. 10, No. 11, pp. 1425-1429, 1972
25. Karimipanah, T., “Turbulent jets in confined spaces- Application in mixing ventilation Experimental and Numerical Studies”, *PhD thesis, Royal Institute of Technology*, 1996.
26. Kavsaoglu, M. S. and Schetz, J. A., “Effects of Swirl and High Turbulence on a Jet in a Crossflow”, *Journal of Aircraft*, Vol. 26, No. 6, pp. 539-546, 1989
27. Keffer, J. F. and Baines, W. D., “The round turbulent jet in a cross-wind”, *Journal of Fluid Mechanics*, Vol. 15, part 4, pp. 481-496, 1963.
28. Kelso, R. M., Lim, T. T., and Perry, A. E., “An experimental study of round jets in cross-flow”, *Journal of Fluid Mechanics*, Vol. 306, pp. 111-144, 1996.
29. Kerney, P. J., Faeth, G. M., and Olson, D. R., “Penetration Characteristics of a Submerged Steam Jet”, *AIChE Journal*, Vol. 18, No. 3, pp. 548-553, 1972.

30. Krothapalli, A., Lourenco, L., and Buchlin, J. M., “Separated Flow Upstream of a Jet in a Crossflow”, *AAIA Journal*, Vol. 28, No. 3, pp. 414-420, 1990.
31. Laberteaux, K. R. and Ceccio, S. L., “Partial cavity flows. Part 1. Cavities forming on Models Without Spanwise Variation”, *Journal of Fluid Mechanics*, Vol. 431, pp. 1-41, 2001.
32. Long, M. B. and Chu, B. T., “Mixing Mechanism and Structure of an Axisymmetric Turbulent Mixing Layer”, *AIAA Journal*, Vol. 19, No. 9, pp. 1158-1163, 1981.
33. Maeda, M., Yamaguchi, H., and Kato, H., “Laser Holography Measurement of Bubble Population in Cavitation Cloud on a Foil Section”, *Proceedings of the A.S.M.E. Cavitation '91 Symposium*, Vol. 116, pp. 67-75, 1991.
34. Mahesh, K., “The Interaction of Jets with Crossflow”, *Annual Review of Fluid Mechanics*, Vol. 45, pp. 379-407, 2013.
35. Mäkiharju, S.A., Chang, N., Gabillet, C., Paik, B.-G., Perlin, M. and Ceccio, S.L., “Time Resolved Two Dimensional X-Ray Densitometry of a Two Phase Flow Downstream of a Ventilated Cavity.” *Experiments in Fluids*, v. 54, n. 7, 2013.
36. Morton, B. R. and Ibbetson, A., “Jets Deflected in a Crossflow”, *Experimental Thermal and Fluid Science*, Vol. 12, pp. 112-133, 1996.
37. Newman, J. N., “Marine Hydrodynamics”, *The MIT press*, 1977.
38. Parkin, B. W., and Kermeen, R. W., “The Roles of Convective Air Diffusion and Liquid Tensile Stresses During Cavitation Inception”, *Proceedings I.A.H.R. Symposium on Cavitation and Hydraulic Machinery, Sendai, Japan*, pp. 21-24, 1963.
39. Parkin, B. W. and Ravindra, K., “Convective Gas Diffusion in Steady Cavity Flows”, *ASME Journal of Fluid Engineering*, Vol. 113, pp. 285-289, 1991.

40. Pignoux, S., “Structure interne d'un jet de gaz injecté perpendiculairement à une couche limite turbulente verticale d'eau”, PhD thesis, Univrtsity of Poitiers, France, 1998.
41. Sabersky, R. H., Acosta, A. J., Hauptmann, E. G., and Gates, E. M., “Fluid Flow”, *Prentice Hall International, Inc*, 1999.
42. Savory, E., Toy, N., and Ahmed, S., “Experimental study of a plume in a crossflow”, *Journal of Wind Engineering and Industrial Aerodynamics*, Vol. 60, pp. 195-209, 1996.
43. Stutz, B., and Legoupil, S., “X-ray measurements within unsteady cavitation”, *Experiments in Fluids*, Vol. 35, pp. 130-138, 2003.
44. Sucec, J. and Bowley, W. W., “Prediction of the Trajectory of a Turbulent Jet Injected Into a Crossflowing Stream”, *ASME Journal of Fluids Engineering*, pp. 667-672, 1967.
45. Sykes, R. I., Lewellen, W. S., and Parker, S. F., “On the vorticity dynamics of a turbulent jet in a crossflow”, *Journal of Fluid Mechanics*, Vol. 168, pp. 393-413, 1986.
46. Thwaites, B., “Incompressible aerodynamics”, *Dover Publications, Inc*., 1960.
47. Vigneau, O., Pignoux, S., Carreau, J. L., and Roger, F., “Influence of the wall boundary layer thickness on a gas jet injected into a liquid crossflow”, *Experiments in Fluids*, Vol. 30, pp. 458-466, 2001.
48. Yu, P. W., and Ceccio, S. L., “Diffusion Induced Bubble Populations Downstream of a Partial Cavity”, *Journal of Fluids Engineering*, Vol. 119, No. 4, pp. 782-787, 1997.
49. Yu, X., Wang, Y., Huang, C., Wei, Y., Fang, X., Di, T., and Wu, X., “Experiment and simulation on air layer drag reduction of high-speed

underwater axisymmetric projectile”, *European Journal of Mechanics B/Fluids*, Vol. 52, pp. 45-54, 2015.

50. Yuan, L. L. and Street, R. L., “Trajectory and entrainment of a round jet in crossflow”, Physics of Fluids, Vol. 10, No. 9, pp. 2323-2335, 1998.